DIAMOND HETEROEPITAXIAL LATERAL OVERGROWTH

By

Yung-Hsiu Tang

A DISSERTATION

Submitted to
Michigan State University
in partial fulfillment of the requirements
for the degree of

Physics-Doctor of Philosophy

2015

ABSTRACT

DIAMOND HETEROEPITAXIAL LATERAL OVERGROWTH

By

Yung-Hsiu Tang

This dissertation describes improvements in the growth of single crystal diamond by microwave plasma-assisted chemical vapor deposition (CVD). Heteroepitaxial (001) diamond was grown on 1 cm² a-plane sapphire substrates using an epitaxial (001) Ir thin-film as a buffer layer. Low-energy ion bombardment of the Ir layer, a process known as bias-enhanced nucleation, is a key step in achieving a high density of diamond nuclei. Bias conditions were optimized to form uniformly-high nucleation densities across the substrates, which led to well-coalesced diamond thin films after short growth times.

Epitaxial lateral overgrowth (ELO) was used as a means of decreasing diamond internal stress by impeding the propagation of threading dislocations into the growing material. Its use in diamond growth requires adaptation to the aggressive chemical and thermal environment of the hydrogen plasma in a CVD reactor. Three ELO variants were developed. The most successful utilized a gold (Au) mask prepared by vacuum evaporation onto the surface of a thin heteroepitaxial diamond layer. The Au mask pattern, a series of parallel stripes on the micrometer scale, was produced by standard lift-off photolithography. When diamond overgrows the mask, dislocations are largely confined to the substrate. Differing degrees of confinement were studied by varying the stripe geometry and orientation. Significant improvement in diamond quality was found in the overgrown regions, as evidenced by reduction of the Raman scattering linewidth. The Au layer was found to remain intact during diamond overgrowth and

did not chemically bond with the diamond surface. Besides impeding the propagation of threading dislocations, it was discovered that the thermally-induced stress in the CVD diamond was significantly reduced as a result of the ductile Au layer. Cracking and delamination of the diamond from the substrate was mostly eliminated. When diamond was grown to thicknesses above 0.1 mm it was found that crystallographic perfection continuously improved, leading to a diamond surface nearly free of stress.

Copyright by YUNG-HSIU TANG 2015 For my dear mom

ACKNOWLEDGMENTS

During the past five years, I immersed myself in the lab and tried to figure out the clues from the results. Most of time, I was completely in the dark and missed the puzzles. My advisor, Dr. Golding, was always there with me to look for the clues and put the puzzles together. In the beginning of the research, I often felt anxious and discouraged from uncontrolled experiments. My advisor told me that doing real research is living with high uncertainty. It takes more than anyone can imagine to accomplish this goal. Then, I started to learn how to adjust myself to mold into this lifestyle. I gratefully appreciate his guidance. He always encourages me and is always there with suggestions. Without his support, in every respect, in the first place, I would not be able to finish this degree. His patience and enthusiasm for scientific research will always be my model in the future.

I also greatly thank Dr. Baokang Bi, not only for his technical support in the KMF facilities, but also for valuable ideas for experimental designs. He always patiently answers my questions of any kind. The encouragement from Dr. Bi and Dr. Reza Loloee strongly motivated me to focus on the project. Thanks my committee members: Dr. Chih-Wei Lai, Dr. Carlo Piermarocchi, Dr. Megan Donahue, and Dr. Wade Fisher for their encouragement and suggestions.

The experiments would not be improved without help from the machining experts: Thomas Palazzolo, James Muns and Thomas Hudson from the Physics machine shop and Scott Bankroff from the Chemistry glassblowing facility. I always submitted complicated and difficult works. I really appreciate that they always finished the jobs on time with perfect parts. Finally, I would like to thank my dear mother who always supports my decisions, so I can endeavor to

accomplish the PhD degree. My husband, Tung-Wu, always accompanies me, sharing my happiness and tears in every moment.

I also thank the DOE for support of this research under grant DE-FG52-08NA28767.

TABLE OF CONTENTS

LIST OF TABLESxi			
LIST	LIST OF FIGURESxii		
1.	Chapter 1 Introduction	1	
2.	Chapter 2 Diamond: structure and physical properties	4	
2.1	Diamond crystal structure		
2.2	Electronic properties	5	
2.3	Optical properties	8	
2.4	The synthesis of diamond	10	
2.5	Diamond types: Impurities	11	
3.	Chapter 3 Characterization methods	12	
3.1	Scanning electron microscopy	12	
3.2	Atomic force microscopy	14	
3.3	X-ray diffraction (XRD)	16	
3	Rocking curve	18	
3.4	Raman spectroscopy	19	
3	Theory of Raman scattering	19	
	3.4.1.1 Polarized Raman spectroscopy		
	3.4.1.2 Stress measurements by polarized Raman spectroscopy	23	
3	Micro-Raman spectral method	27	
	3.4.2.1 Spectrum analysis		
	3.4.2.2 Spatial Raman scanning	29	
4	Chapter 4 Plasma-assisted heteroepitaxial growth	30	
4.1	Properties of plasma	30	
	1.1.1 Glow discharge		
4.2	DC magnetron sputtering	32	
۷	Configurations of AJA sputtering system		
	4.2.1.1 Oxidation issue in AJA		
4.3	Chemical vapor deposition (CVD)	35	
4	Configurations of the CVD reactor		
	4.3.1.1 Energy source of CVD reactor		
	4.3.1.2 Gas handling of CVD reactor		
	4.3.1.3 Biasing set up and circuit		
	4.3.1.4 Computer controlling/monitoring system		
	4.3.1.5 Substrate loading in CVD reactor		
۷	Configurations of AsTex reactor		
	4.3.2.1 Energy source of AsTex reactor		
	4.3.2.2 Gas handling of AsTex reactor		
	4.3.2.3 Temperature measurement	43	

	4.3.2.4	Substrate loading in AsTex reactor	43
	4.3.3	Diamond CVD methods	
	4.3.3.1	Effects of growth parameters	47
	4.3.3.2	Growth anisotropy: the α parameter	49
5	Chapt	er 5 Diamond nucleation and heteroepitaxy	51
		ucleation	
	5.2 C ₁	rystal growth modes	53
	5.3 He	eteroepitaxial diamond growth	54
	5.3.1	Epitaxy	54
	5.3.2	Definition of diamond heteroepitaxy	
	5.3.3	Substrate criteria for diamond heteroepitaxy	56
	5.3.3.1	Heteroepitaxial diamond growth on bulk substrates	59
	5.3.3.2	Heteroepitaxial diamond growth on Ir	
	5.4 Er	nhancement of diamond nucleation	
	5.4.1	Bias enhanced nucleation (BEN)	62
	5.4.1.1	Proposed mechanism of BEN	62
	5.4.1.2	Bias and plasma chemistry	
	5.4.1.3	Bias enhanced nucleation on iridium	
6.	Chapt	er 6 Epitaxial lateral overgrowth (ELO)	79
		islocations	
		LO method	
	6.3 Ty	ypes of ELO on GaN	
	6.3.1	Facet-initiated ELO (FIELO)	
	6.3.2	Different masking materials	
	6.3.3	PENDEO epitaxy	
	6.3.4	Air-bridged ELO	
	6.3.5	Cantilever epitaxy	
	6.3.6	Direct lateral epitaxy	
	6.4 Ty	ypes of ELO on diamond	89
7.		er 7 Epitaxial Ir growth on a-plane sapphire	
		-plane sapphire (a-ALO)	
	7.1.1	Epitaxial relation between Ir and a-ALO	
		sputtering procedure	
	7.2.1	Sapphire preparation	
	7.2.2	Sample mounting and loading	
	7.2.3	Ir DC sputtering	
	7.2.3.1	Bias cleaning on a-ALO	
	7.2.3.2	Ir DC sputtering rate	
		esults for Ir (001) epilayers	
	7.3.1	Ir x-ray diffraction (XRD)	
	7.3.2	Ir surface topography on a-ALO	
	7.4 Ir-	-ALO wafer processing	109

8.	Chapter 8 Heteroepitaxial growth of diamond	111
8.1	Fixtures for biasing	
8.2	Procedure for diamond growth	112
8.3	Result of BEN on Ir	115
8.4	Heteroepitaxial CVD diamond thin film growth	116
8.5	Procedure of thick diamond growth in AsTex	120
8.6	Heteroepitaxial CVD diamond thick film growth	120
9.	Chapter 9 Diamond heteroepitaxial lateral overgrowth	126
9.1	Au-masked Diamond ELO	126
9.1	\mathcal{S}	
9.1	.2 Diamond regrowth	131
9	P.1.2.1 Early stage of coalescence	133
9	9.1.2.2 Intermediate thickness diamond films	138
9	P.1.2.3 Thick diamond growth	
9.2	PENDEO for Diamond ELO	144
9.2	.1 Substrate preparation	145
9.2	5 T	
9.2	.3 Regrowth of protected diamond stripes	150
9.3	Diamond ELO with SiO ₂ mask	152
9.3	T T	
9.3	.2 BEN on patterned SiO ₂ /Ir (001)/a-ALO substrates	154
10.	Chapter 10 Conclusions and outlook	158
APPEN	DIX	162
RIRI 16	ACR A PHV	167

LIST OF TABLES

Table 2.1 Bandgaps, E _g , of some common semiconductors.	. 6
Table 2.2 Diamond types according to impurities and corresponding concentrations. ²⁸	11
Table 3.1 Raman selection rules for backscattering from a (001) surface, with $x' [110]$, $y' [-110]$, and $z' [001]$.	25
Table 3.2 Raman selection rules for backscattering from a (110) surface, with $x' [110]$, $y' [-110]$, and $z' [001]$.	26
Table 5.1 Thermal expansion coefficients of some substrates used in diamond heteroepitaxy (at 300 K).	t 58
Table 5.2 Comparison of growth conditions for samples shown in Figure 5.16.	78
Table 5.3 Bias conditions for groups studying diamond heteroepitaxy on Ir.	78
Table 7.1 Typical steps for Ir sputtering. The pressure is set at 30 mTorr in the first step to ignit the RF plasma prior to substrate cleaning.	
Table 8.1 Detailed conditions for CVD diamond thin film growth, with temperature measured of the Mo cap by a single-color pyrometer.	
Table 8.2 Standard bias conditions	15
Table 8.3 Detailed growth parameters of thick heteroepitaxial diamond. Row lists the corresponding growth conditions. Multiple growth steps were used for samples A and B. The listed temperature is the reading from a single color pyrometer focused on diamond top surface	
Table 9.1 Growth conditions of ELO diamond with different initial thicknesses. Growth with tweeters is indicated by x/y	
Table 9.2 Conditions of diamond plasma etch in pure H ₂ .	47
Table 9.3 Regrowth conditions of sample 13-3 after H ₂ plasma etch	50
Table A.1 Temperature dependent thermal expansion coefficients of diamond and sapphire. 173	64
	0 1

LIST OF FIGURES

Figure 2.1 Diamond crystal structure which belongs to the space group $Fd\overline{3}m$. ¹⁴ The red balls represent the basis from $(0,0,0)$ to $(\frac{1}{4},\frac{1}{4},\frac{1}{4})$ and the blue balls are the neighboring carbon atoms connected by the nearest neighbor bonds, the orange sticks.	ļ
Figure 2.2 Diamond electronic band structure calculated by linearized augmented plane wave method (LAPW) 15 , where the conduction band minimum occurs at 0.73 $\overrightarrow{\textbf{\textit{TX}}}$, and the valence band maximum is at the center of the Brillouin zone. Therefore, the diamond bandgap is indirect and 5.5 eV.	
Figure 2.3 Brillouin zone of diamond. 15)
Figure 2.4 Schematic diagram of energy levels in materials with (a) positive electron affinity, such as silicon and (b) negative electron affinity, such as diamond. E_C is the energy minimum of the conduction band, E_V is the energy maximum of the valence band, E_F is the Fermi energy, and E_{Vac} represents the vacuum level.	
Figure 2.5 Transmission spectrum of diamond. 19)
Figure 2.6 Raman-active vibrational mode of diamond. The arrows represent the relative displacement of a near-zero wavevector optical mode. ¹⁹)
Figure 2.7 Pressure-temperature diagram of carbon. ²⁷)
Figure 3.1 Schematic of a scanning electron microscope (SEM). ²⁹)
Figure 3.2 Interaction between primary beam and sample, where the range R depends on the primary beam energy and the specimen. ²⁹	j
Figure 3.3 Schematic of Digital Instruments DI 3100 AFM in tapping mode. ³¹	,
Figure 3.4 Schematic of XRD geometry)
Figure 3.5 Illustration of Bragg condition. The solid circles represent a 2-D projection of the ordered atoms with lattice spacing d . Solid arrows are the incident and scattered x-ray beams with diffraction angle θ respect to the lattice plane. The path difference between ray (1) and (2) is $2dsin\theta$. If it equals an integer multiple of the x-ray wavelength, ray (1) and (2) will constructively interfere.	
Figure 3.6 Schematic of Bruker AXS D8 x-ray diffractometer. ³¹)
Figure 3.7 Raman spectrum of CCl ₄ (488 nm excitation), showing Stokes and anti-Stokes spectra and the central Rayleigh scattering. 21	

Figure 3.8 Raman spectra of Type IIa natural diamond in [001] backscattering geometry. (a) For $e_i \parallel [110]$, only polarization of incident light parallel to the polarization of scattered light, $e_s \parallel [110]$, is allowed. (b) For $e_i \parallel [010]$, the polarization of the scattered light must be perpendicular to the polarization of the incident light, $e_s \parallel [100]$. Due to a polarization "leak", the measured intensity is non-zero for forbidden polarizations.
Figure 4.1 n_e vs. T_e for different plasmas. ⁴³
Figure 4.2 A glow discharge tube and its major characteristics. ⁴⁴
Figure 4.3 Schematic of AJA sputtering system
Figure 4.4 Schematic of the microwave plasma-assisted CVD (MPCVD) system for heteroepita-xial diamond growth. ⁴⁷
Figure 4.5 Illustration of the TM ₀₁₃ electromagnetic mode inside a cavity. ⁴⁸ Solid lines represent electric fields; dashed lines the magnetic fields
Figure 4.6 Schematic of bias set up in CVD reactor with: (1) Mo cap (2) Ir/a-ALO substrate (3) Mo post (4) bias lead (5) Mo shield (6) Mo base plate (7) ceramic spacer (8) tungsten bias ring (9 ceramic spacer (10) grounded stainless steel spacer (11) cooling stage
Figure 4.7 Illustration of bias circuit. ⁴⁷ 39
Figure 4.8 Schematic of AsTex system. ³¹ 42
Figure 4.9 Illustration of the water-cooled sample stage in AsTex system. ³¹
Figure 4.10 Illustration of model of diamond nucleation and growth on a substrate. ⁴⁵
Figure 4.11 Diamond growth rate vs. growth temperature in 4% methane. The growth rate follows the Arrhenius relation but saturates above 1000 °C.
Figure 4.12 Diamond growth rate vs. methane concentration at 770 °C (upper two points) and 800 °C (lower two points). 48
Figure 4.13 Shapes of diamond crystals for different values of α , the growth parameter. The arrow indicates the fastest growth direction for each case. 50
Figure 4.14 α vs. methane concentration at different temperatures. ⁶³
Figure 5.1 Change of free energy (ΔG) vs. radius of nucleus according to CNT, where r^* is the radius of the critical nucleus. The first order phase transition becomes energetically favorable when the nucleus radius is beyond r_0 .
Figure 5.2 Illustrations of three thin film epitaxial growth modes as a function of surface coverage θ in terms of monolayers (ML): (a) island growth, or Volmer-Weber mode, (b) layer-plusisland growth or Stranski-Krastanov mode, and (c) layer-by-layer growth or Frank-van der

Figure 5.3 Illustration of BEN mechanism. 103	. 63
Figure 5.4 Optical emission spectrum of a CH_4 - H_2 plasma at 30 Torr and 2% CH_4 . Ar was use as an actinometer to estimate the concentration of atomic hydrogen. The wavelengths of emission lines of C_1 and C_2 type species are indicated. 114	
Figure 5.5 Intensity of H_{α} emission vs. methane and oxygen flow rates, representing the relationships between atomic hydrogen, methane, and oxygen concentrations. The methane concentration is 9% with a hydrogen flow rate of 100 sccm and methane flow rate of 10 sccm.	
Figure 5.6 Concentrations of (a) atomic hydrogen (b) two types of hydrocarbons (c) H_B/H_α and ratios of C_2/H and CH/H_α vs. bias voltage at 15 Torr and 2% CH_4 .	d (d)
Figure 5.7 Concentrations of (a) atomic hydrogen (b) H_B/H_α and (c) ratios of C_2/CH vs. position relative to substrate surface in vertical direction, where the solid triangles and hollow rhombohedra represent the data points without and with bias voltage under conditions of 30 Te and 2% CH_4 .	orr
Figure 5.8 Plan-view SEM images of BEN-treated Ir surfaces with increasing methane content. ¹²⁷	. 70
Figure 5.9 Plan-view SEM image of BEN-treated Ir surface showing Ir furrows, Ir balls, brigh spots and the domains, where the scale of the images inside the circles is 100 nm. 129	
Figure 5.10 Low-resolution SEM image of BEN-treated Ir surface showing the bright areas rered to as domains. 128	fe- . 71
Figure 5.11 Plan-view SEM images of (a) domain formation on Ir after 30 min BEN and (b) 1 min diamond growth in the domain. 129	5 . 72
Figure 5.12 Plan-view SEM image of Ir surface after 20 min bias. ⁹	. 73
Figure 5.13 (a) Plan-view SEM image and (b) HRTEM cross-sectional image of BEN treated surface after 60 min. ³¹	Ir . 74
Figure 5.14 (a) Plan-view SEM image and (b) HRTEM cross-sectional image of 90s diamond growth on a 60-min biased Ir surface. In (b) each white line is the (111) plane of Ir (bottom) at diamond (surrounded by blue dashed line) crystals. ³¹	nd
Figure 5.15 Plan-view SEM image of diamond surface after 10 min growth following 60 min biasing.	. 76
Figure 5.16 Heteroepitaxial diamond surface after 20 min growth (a) ⁴⁷ and (b) ¹²⁷ . Diamond surface after 60 min growth (c) ⁴⁷ and (d) ¹²⁷	. 77

Figure 6.1 Illustration of dislocation geometry: (a) a perfect single cubic lattice as reference; distorted crystal lattices with a dislocation line DC which is a positive edge type in (b); a left-handed screw type in (c); and a right-handed screw type in (d). 80
Figure 6.2 HRTEM image at the interface between diamond and Ir. The circled area by the blue dashed line is the diamond grain. The blue and white lines represent the diamond (111) and Ir (111) lattice planes, respectively. A misfit dislocation formed at the interface, indicated by
Figure 6.3 Illustration of an ELO process. (a) A thin epi layer serves as a substrate, where the solid lines generated from the substrate represent the threading dislocations. (b) A mask, e.g. SiO ₂ , is deposited and patterned by lithography. (c) Material overgrows the mask which blocks the threading dislocations during regrowth. The threading dislocation density is greatly reduced in the overgrown regions.
Figure 6.4 Illustration of PENDEO epitaxy. (a) A GaN epitaxial layer grown on a 6H-SiC substrate with AlN buffer layer serves as a substrate for the PENDEO process. (b) The GaN epilayer is plasma-etched to form alternating columns and trenches. (c) Regrowth of GaN columns has a large lateral-to-vertical growth rate ratio. 85
Figure 6.5 Illustration of air-bridged ELO: (a) a GaN/sapphire substrate; (b) GaN layer partly plasma etched to form ridges; (c) regrowth of GaN and (d) coalesced GaN overgrown layer in the center of masked region. In (b), except for the top surfaces of GaN ridges, other areas are covered by the Si ₃ N ₄ mask. ¹⁵¹
Figure 6.6 Illustration of cantilever epitaxy. (a) Substrates 6H-SiC, Si and Al ₂ O ₃ , are plasma etched to form trenches (etched area) and terrace (unetched). (b) GaN layers grow on substrate terraces.
Figure 6.7 Steps of the diamond ELO process by Ando et al. and Washiyama et al. 12
Figure 7.1 Hexagonal crystallographic unit cell of sapphire. The a-plane is shaded
Figure 7.2 Illustration of proposed epitaxial relationship of Ir and a-ALO, where the small and large spheres represent the O and Ir atoms, respectively
Figure 7.3 AFM images of annealed surfaces of (a) 0-a-ALO (b) 1C-a-ALO (b) 1M-a-ALO and (d) 0.7M-a-ALO wafers.
Figure 7.4 AFM images of 1C-a-ALO surface annealed at (a) 1300 °C and (b) 1500 °C for 24h.
Figure 7.5 XRD diffraction patterns of 24-nm Ir on 1C-a-ALO substrates sputtered at 3 mTorr, 100W and 850 °C: (a) with plasma cleaning at 3 mTorr, 30W and 850 °C for 5 min and (b) without cleaning prior to the Ir sputtering.

Figure 7.6 AFM images of a-ALO (a) before plasma cleaning and (b) after plasma cleaning at 3 mTorr, 30W and 850 °C for 5 min. The sparse bright spots in (a) are nanoparticles which cannot be removed by standard solvent cleaning.
Figure 7.7 Linewidth of (002) _{Ir} XRD rocking curve vs. (a) bias duration and (b) bias power 101
Figure 7.8 AFM image of 300-nm Ir on a-ALO plasma cleaned at 3 mTorr, 30W and 850 °C for 10 min
Figure 7.9 Ir sputtering rate vs. (a) sputtering gun power and (b) Ar pressure in the AJA system measured at room temperature
Figure 7.10 XRD diffraction pattern of 300-nm Ir on highly-oriented a-ALO. Small peaks originate from the small fraction of Cu K_{β} radiation in the incident x-ray beam
Figure 7.11 X-ray rocking curve of Ir (200) with Gaussian fit
Figure 7.12 Ir (200) rocking-curve linewidth vs. substrate deposition temperature
Figure 7.13 AFM images of 300-nm Ir sputtered by the process in Table 7.1 on a (a) 0-a-ALO (b) 1C-a-ALO (c) 1M-a-ALO and (d) 0.7M- a-ALO
Figure 7.14 High-resolution AFM images of 300-nm Ir on a (a) 0-a-ALO (b) 1C-a-ALO (c) 1M-a-ALO and (d) 0.7M-a-ALO
Figure 7.15 AFM images of 24-nm thick Ir on unannealed (a) 0-a-ALO and (b) 1M-a-ALO 108
Figure 7.16 AFM image of 150-nm Ir sputtered at 10 mTorr, 100W and 850 °C
Figure 7.17 Illustration of sample holder for substrate side coating
Figure 8.1 Fixturing for the CVD reactor: (1) Mo cap (2) Ir/a-ALO substrate (3) Mo post (4) bias lead (5) Mo shield plate (6) Mo base plate (7) ceramic spacer (8) tungsten bias ring (9) ceramic spacer (10) stainless steel plate (11) grounded cooling stage
Figure 8.2 Time plot of the standard procedure of heteroepitaxial CVD diamond growth 113
Figure 8.3 Plan-view SEM images of biased Ir surface: (a) the featureless amorphous carbon layer covering the Ir surface and (b) Ir nanopillars buried in the carbon layer
Figure 8.4 Four selected optical images of 550 nm diamond thin films, grown in a sequence. The burn marks on edges are caused by the Mo cap. (b) Film is about 100 nm thicker than other samples at its center.
Figure 8.5 Plan-view SEM image of 3h-grown diamond thin film showing a well-coalesced diamond (001) surface. Bright dots are small height fluctuations on the diamond surface 118
Figure 8.6 XRD diffraction pattern of 550-nm diamond on a Ir/a-ALO substrate. Small peaks originate from the small fraction of Cu K _β radiation in the incident x-ray beam

Figure 8.7 XRD φ-scan of 550-nm diamond on a Ir/a-ALO substrate
Figure 8.8 Cross-sectional tilted SEM image of a 70-µm delaminated diamond (001) piece showing a (111) cleavage. At bottom is the Ir layer
Figure 8.9 XRD diffraction pattern of a piece of 85-µm delaminated diamond
Figure 8.10 X-ray rocking curve of diamond (004) reflection with Gaussian fit
Figure 8.11 Raman spectra of IIa natural diamond and thick heteroepitaxial diamonds. The peak center and linewidth of natural diamond are at 1332 cm ⁻¹ and 1.65 cm ⁻¹ , respectively
Figure 8.12 Raman linewidth and frequency vs. thickness of a 85- μ m diamond sample. The linewidth decreases with thickness and the stress is largely relaxed after 30 μ m
Figure 9.1 Illustration of Au-masked diamond ELO (not to scale). The vertical wavy lines depict threading dislocations which are partially restricted in the diamond overlayer
Figure 9.2 Schematic of sample preparation for Au-masked diamond ELO: (a) patterned diamond substrate after PR exposure and development; (b) substrate after Au evaporation; and (c) completed substrate after Au lift-off
Figure 9.3 Optical images of patterned diamond substrates with (a) 4- μ m wide Au stripes with 16 μ m gaps and (b) 8- μ m wide Au stripes with 4 μ m gaps. In both cases, the stripes are parallel to the diamond <110> direction
Figure 9.4 Plan-view SEM images of (a) 10-μm thick ELO diamond with 8-μm wide Au stripes centered on the non-overgrown region. The pits are the terminations of dislocations at the top surface. (b) 2-μm thick ELO diamond with 4-μm wide Au stripes, just prior to diamond coalescence. The white arrows indicate the position of the Au stripes
Figure 9.5 Spatial variations of the Raman linewidth and intensity for a (a) 2-μm thick ELO diamond with 4-μm wide Au stripes and (b) 10-μm thick ELO diamond with 8-μm wide Au stripes. In both cases the diamond has not detached from the substrate. The linewidth is minimized at the overgrown region above the Au stripe
Figure 9.6 (a) Photograph of diamond (001) surface with both delaminated and non-delaminated regions and (b) comparison of the adherent and delaminated regions on 2-μm thick ELO diamond with 4-μm wide Au stripes. The delaminated film has the unstressed diamond Raman frequency whereas the strongly attached film shows large compressive stress. The red dashed line represents the unstressed diamond frequency at 1332.4 cm ⁻¹ . The polarizations of incident and scattered laser beams were parallel to <110>
Figure 9.7 SEM images of a 30-µm thick ELO diamond grown with 4-µm wide Au stripes. (a) Tilted image, the top surface is the (001) face and the sides are {110} fracture surfaces. The Au stripes are visible in the lower part of the crystal. (b) Expanded {110} fracture surface at the region near the Au stripe. The diamond only weakly contacts the Au stripe during overgrowth and forms a void at the top surface of the gold

Figure 9.8 Optical image of Au stripes taken through a 190-μm thick ELO diamond overlayer. The 8-μm wide stripes are oriented parallel to the <110> diamond direction
Figure 9.9 Plan-view SEM images of (a) 75-μm thick ELO diamond with 4-μm wide Au stripes and (b) 190-μm thick ELO diamond with 8-μm wide Au stripes
Figure 9.10 Raman center frequency of 190-μm thick ELO diamond with 8-μm wide Au stripes. The scan covers 8 mm, the diameter of the entire diamond crystal. Very low stress is apparent from the small Raman shift, 1332.4±0.26 cm ⁻¹ .
Figure 9.11 (a) Raman linewidth and (b) Raman frequency vs. thickness of a 75-µm thick ELO diamond with 4-µm wide Au stripes. The linewidth decreases with thickness and the stress is mostly relaxed on the top surface. (c) Photograph of diamond {110} surface. The arrow indicates the scan direction, along [001] _{dia} .
Figure 9.12 Schematic of PENDEO process during diamond growth
Figure 9.13 Illustration of sample preparation for PENDEO diamond ELO: (a) a 550-nm thick diamond substrate patterned with stripes of PR layer by standard photolithography; (b) Au (100 nm) mask layer thermally evaporated on a diamond substrate; and (c) diamond substrate covered by the Au stripes along the <110> direction. See Figure 9.12 for the two last steps of the process.
Figure 9.14 (a) Plan-view SEM image of a diamond stripe after etching with Au mask remaining (center). The Au mask shows damage, with holes visible. (b) 45° tilt SEM image at the boundary of a diamond stripe and the etched trench. The Au masked diamond stripe is on right side; the area on the left has been etched. Note the steep sidewalls of the diamond and the cone-like features in the etched area.
Figure 9.15 Plan-view SEM image of etched area showing the bare Ir surface. Small structures may be Ir coalescence boundaries. No trace of diamond residues is seen
Figure 9.16 Plan-view SEM images of the plasma-etched diamond substrate after regrowth. (a) A diamond stripe, showing the formation of {111} facets on the side walls. (b) Diamond stripes and etched areas shown at lower magnification. The diamond grew in the etched areas and formed oriented crystallites after 3h
Figure 9.17 Illustration of diamond ELO with SiO ₂ mask
Figure 9.18 Steps followed in ELO with the SiO_2 mask process. (a) 500-nm thick SiO_2 , the masking layer, was sputtered onto a Ir (001) surface, where the lines represent the dislocations lines in the Ir layer. (b) The SiO_2 surface was covered with a layer of PR, patterned by photolithography. (c) SiO_2 in the channels was etched by BOE, forming trenches
Figure 9.19 SEM image of exposed Ir surface after biased, showing nanoparticles randomly deposited on the surface

Figure 9.20 DIC optical image of damaged SiO ₂ pattern on Ir (001)/a-ALO substrate	te. After 30
min of -200V bias, the SiO ₂ and Ir surfaces were eroded by arcing	155
Figure 9.21 SEM images of diamond growth near a SiO ₂ boundary. The SiO ₂ layer region in the images. (a) Plan-view and (b) 5° tilt SEM image showing diamond growth near a SiO ₂ boundary.	
to SiO ₂	3

1. Chapter 1 Introduction

Diamond, a wide bandgap semiconductor, is known for its unique physical properties. Its large band gap, high carrier mobility, unsurpassed dielectric breakdown field, and resistance to radiation damage make diamond a good detector for energetic particles, especially fission neutrons. In the 1 MeV energy region of fission neutrons, diamond has the largest linear attenuation coefficient of any known material, 4% per mm. In this region, energy transfer is by elastic collisions, leading to a maximum energy transfer of 28% between a carbon atom and a neutron. Diamond, with atomic number Z=6, has a small photoelectric cross-section, so it is fairly insensitive to gamma rays. As a consequence, diamond is a superior alternative for the Si detector, provided that it can be fabricated as a large area single crystal of high quality. However, very few natural diamonds are suitable for detector applications, owing to their substantial concentration of chemical impurities. Although the chemical vapor deposition (CVD) method has produced wafer-size polycrystalline diamond, the presence of grain boundaries introduces carrier traps. The traps decrease the carrier mobilities and reduce the charge collection efficiency. Therefore, high-purity single crystal CVD diamond grown by epitaxial methods is the most promising choice for particle detectors.

Heteroepitaxial growth of diamond, where diamond is deposited on a non-diamond substrate, is a potential method for expanding the size of single crystal diamond to the wafer scale. Si substrates were first used for CVD diamond heteroepitaxial growth, but due to the large lattice mismatch between diamond and Si, only textured growth, with highly-oriented diamond grains, was achieved.^{2,3} The demonstration of diamond heteroepitaxy on oxide substrates such as MgO,

with an Ir buffer layer between the substrate and the diamond, was the first indication that true diamond heteroepitaxy was feasible.^{4,5} Later, the use of SrTiO₃^{6,7,8,9} as a substrate showed improvement in the reproducibility and quality of heteroepitaxial diamond. Ir epitaxy on a-plane sapphire (a-ALO)¹⁰, a very high-quality and mechanically stable substrate, suggested that heteroepitaxial diamond growth on wafers up to 5-10 cm in diameter should be possible. Somewhat later it was found that the use of multiple buffer layers, Ir and YSZ, on Si¹¹ was an effective system for low-stress growth.

The major concern in heteroepitaxy is the presence of dislocations, which can act to relieve the stress introduced by lattice mismatch, but can also introduce internal stresses. In III-V semiconductors, restricted growth methods, particularly the development of epitaxial lateral overgrowth (ELO), have been shown to reduce threading dislocation densities by 2 to 3 orders of magnitude. However, ELO methods require considerable adaptation to be effective under the conditions used for CVD diamond growth. The first attempts in patterned diamond growth showed that it could lead to a significant reduction of internal stress. ^{12,13}

This dissertation describes experiments on diamond heteroepitaxy that utilize lateral overgrowth methods. Growth is conducted with iridium buffer layers on a-plane sapphire substrates. Appreciable effort has been placed on developing reproducible methods for growth of epitaxial Ir on sapphire by sputtering and subsequent microwave plasma CVD diamond nucleation and growth on one centimeter square substrates. A novel and particularly effective method for lateral overgrowth that uses a thin metal mask has been discovered. The Au-masked ELO method successfully prevents dislocations from propagating into the growing crystal, thus reducing internal stress in the diamond layer. This method also appears to reduce significantly

the stresses that occur between diamond and its substrate. The net result is high-quality, single crystal diamond of nearly 1 cm diameter and arbitrary thickness.

This dissertation contains ten chapters. Chapter 2 describes the physical properties of diamond and some historical information. Chapter 3 covers the analytical tools used for diamond characterization. Chapter 4 describes the instrumentation used for a variety of thin-film depositions, namely, sputtering systems for Ir epitaxy and CVD reactors for diamond growth. Factors affecting CVD diamond growth are discussed here as well. Chapter 5 provides background for diamond heteroepitaxy on various substrates and the method of bias-enhanced nucleation. Chapter 6 summarizes a number of previous lateral overgrowth methods used for other semiconductors as well as previous studies on diamond. Chapter 7 describes Ir epitaxy by sputtering and characterization of sputtered films. Chapter 8 introduces the presently used methods for heteroepitaxial thin- and thick-film CVD diamond growth. Chapter 9 discusses three variants of ELO that have been devised to improve diamond heteroepitaxy and subsequent characterization of the crystal quality of the materials. Finally, Chapter 10 summarizes the accomplishments of this project and provides suggestions for future work.

2. Chapter 2 Diamond: structure and physical properties

2.1 Diamond crystal structure

The diamond structure is a face-centered cubic (FCC) lattice with a basis. It can be viewed as two superimposed FCC lattices, one displaced relative to the other along a body diagonal by one quarter of the lattice parameter a_0 , (0,0,0) to $(\frac{1}{4},\frac{1}{4},\frac{1}{4})$ from the origin, where $a_0 = 0.375$ nm, Figure 2.1 The four valence electrons of each carbon atom hybridize to form tetrahedral sp³ bonds with four other carbon neighbors. The nearest-neighbor bond length is 0.154 nm which is the shortest of any three-dimensional crystal, leading to a highly compact structure and the hardest known material.

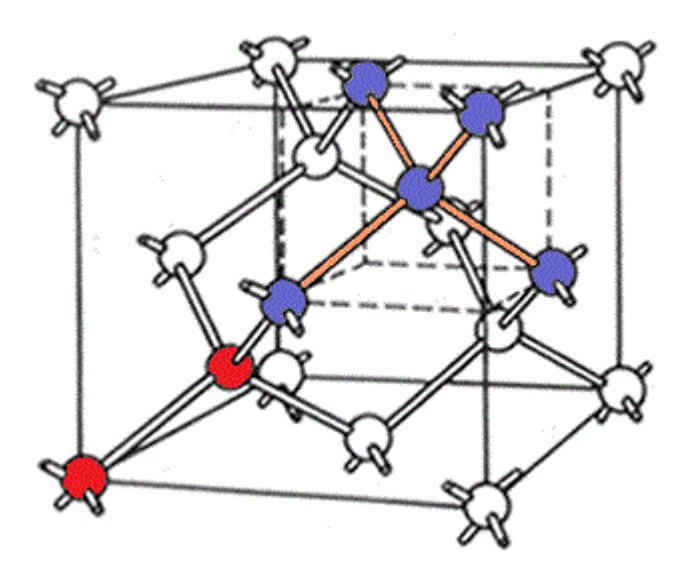


Figure 2.1 Diamond crystal structure which belongs to the space group $\operatorname{Fd}\overline{3}$ m.¹⁴ The red balls represent the basis from (0,0,0) to $(\frac{1}{4},\frac{1}{4},\frac{1}{4})$ and the blue balls are the neighboring carbon atoms connected by the nearest neighbor bonds, the orange sticks.

2.2 Electronic properties

The electronic band structure of diamond, similar to silicon, has an indirect band gap of 5.5 eV, shown in Figure 2.2 The conduction band minimum occurs at a distance $0.73 \overrightarrow{\Gamma X}$, which is the unit vector in the [100] direction, Figure 2.3, and valence band maximum is located at the Γ point. The strong sp³ bonding and short bond length of diamond give rise to the largest bandgap among the semiconductors, about 5 times larger than silicon. The bandgaps of common semiconductors are shown in Table 2.1 for comparison.

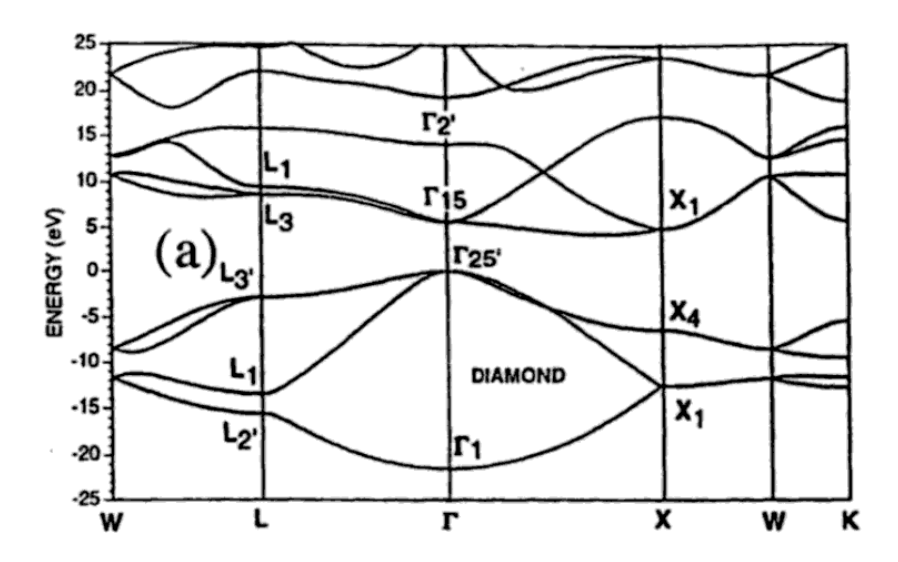


Figure 2.2 Diamond electronic band structure calculated by linearized augmented plane wave method (LAPW)¹⁵, where the conduction band minimum occurs at $0.73 \, \overline{FX}$, and the valence band maximum is at the center of the Brillouin zone. Therefore, the diamond bandgap is indirect and $5.5 \, \text{eV}$.

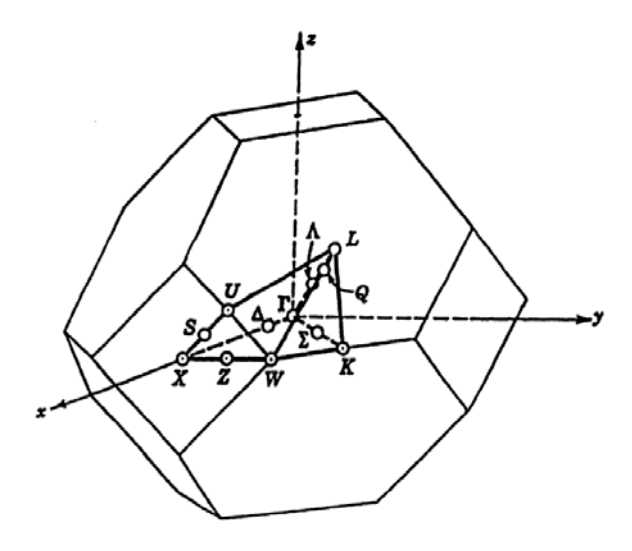


Figure 2.3 Brillouin zone of diamond. 15

Table 2.1 Bandgaps, E_g, of some common semiconductors.

Semiconductor	Symbol	E _g (eV)
Silicon	Si	1.1
Gallium Arsenide	GaAs	1.4
Silicon carbide	SiC	3.3
Gallium Nitride	GaN	3.4
Zinc oxide	ZnO	3.4
Diamond	C	5.5

Owing to the large bandgap of diamond, only a very small fraction of carriers are excited to the conduction band, even at temperatures of 600 °C. In Si, electric field-induced migration occurs at these temperatures, leading to device failure. Diamond also has a very high thermal conductivity, $2000 W/m \cdot K$, which is nearly 5 times larger than copper at room temperature, a high dielectric strength, 10^7 V/cm^{-1} and high electron and hole mobilities, 4500 and 3800

cm²/V·s¹⁶, respectively. Combining the advantages mentioned above, diamond is a promising material for high temperature and high frequency devices.

The hydrogen-terminated surface of CVD diamond exhibits negative electron affinity (NEA) because of the growth environment of a hydrocarbon plasma.¹⁷ NEA indicates that the energy of the vacuum level, i.e., the continuum of unbound electron states outside the semiconductor, lies below the conduction band minimum, Figure 2.4. Consequently, surface electrons can escape from the diamond, which makes diamond an attractive electron emitter.¹⁸

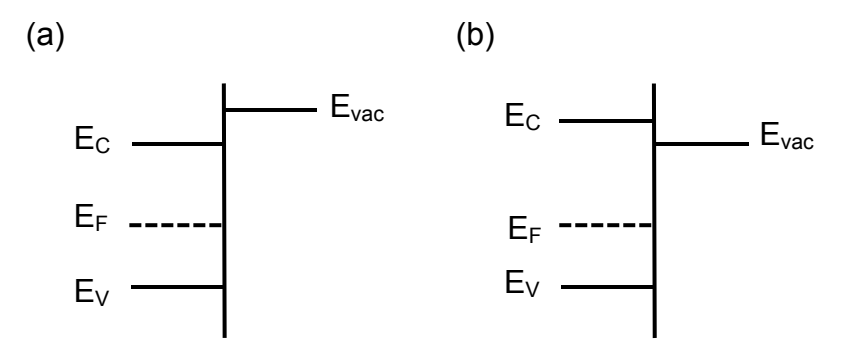


Figure 2.4 Schematic diagram of energy levels in materials with (a) positive electron affinity, such as silicon and (b) negative electron affinity, such as diamond. E_C is the energy minimum of the conduction band, E_V is the energy maximum of the valence band, E_F is the Fermi energy, and E_{Vac} represents the vacuum level.

2.3 Optical properties

Diamond is clear and colorless because of its large band gap and the lack of first-order infrared absorption. In addition, it has a refractive index of 2.42 at 532 nm. Figure 2.5 is the transmission spectrum of diamond, where the measurement shows little absorption except in the ultraviolet (UV) and infrared (IR) regions. The UV absorption below 227 nm, corresponding to 5.47 eV, represents the onset of inter-band transitions. The indirect bandgap prohibits electronic excitations without the creation of phonons. Hence, strong band to band luminescence is quenched.

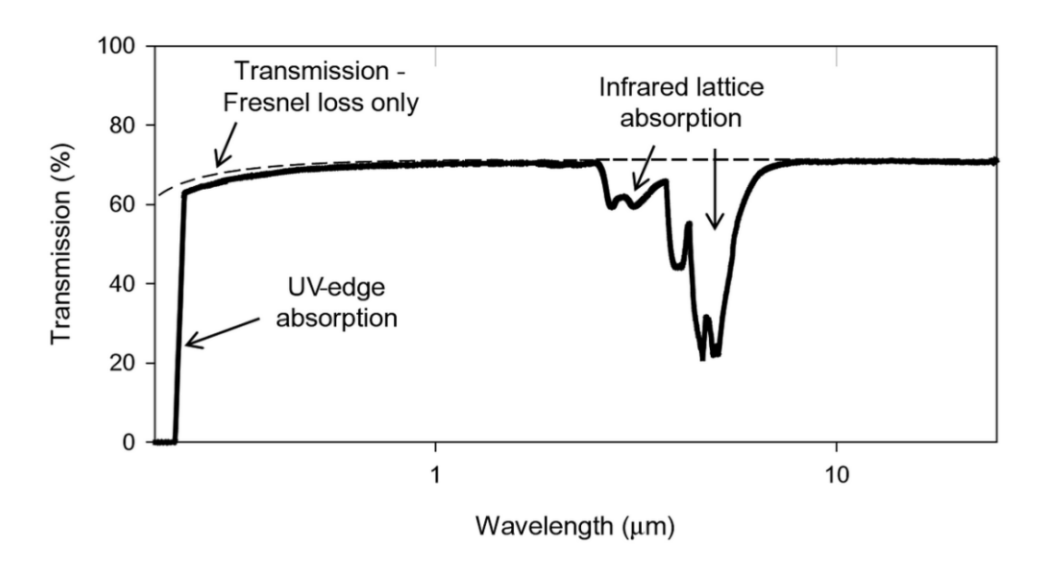


Figure 2.5 Transmission spectrum of diamond. 19

The IR absorption, at 2.6- $6.2 \mu m$, arises from vibrational multiphonon absorption. In Figure 2.5, the two-, and three-phonon absorption peaks are located at 2.6 and $3.75 \mu m$, respectively, which correspond to integer multiples of the highest phonon frequencies, 2665 and 3997 cm⁻¹.

The diamond Raman vibrational mode is the relative movement of two interpenetrating FCC lattices which comprise the diamond C-C bond, shown in Figure 2.6. This Raman mode is triply degenerate. The longitudinal and the two transverse vibrational branches converge at a single point in their phonon dispersion curves²⁰. The Raman linewidth is measured as 1.6 cm⁻¹ at room temperature, measured on differing samples.^{21,22,23,24}

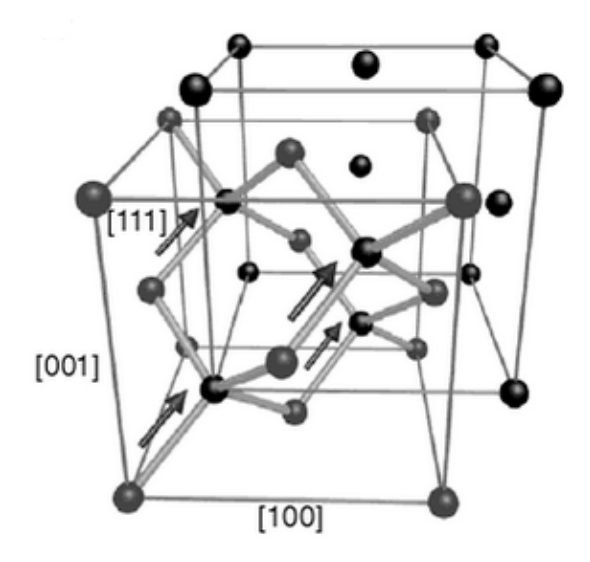


Figure 2.6 Raman-active vibrational mode of diamond. The arrows represent the relative displacement of a near-zero wavevector optical mode.¹⁹

2.4 The synthesis of diamond

The phase diagram of carbon, Figure 2.7, shows that, at ambient conditions, graphite is the ground state of carbon, whereas diamond is a metastable phase. Thus, the formation of natural diamond occurs in a high temperature and high pressure environment. In 1955, Bundy *et al.* invented the high pressure, high temperature (HPHT) method to mimic the conditions of natural diamond genesis. In this method, a pressure cell containing graphite powders with a catalyst, such as Fe, Co or Ni, is compressed to thousands of atmospheres and heated to over 2000 K, creating bulk diamond crystals. The size of HPHT diamond is limited by the cell, typically 1-3 mm² on each face. On the other hand, diamond deposition on a substrate was found to be feasible in its metastable region by chemical vapor deposition (CVD) methods. This synthesis method operates at sub-atmospheric pressures, 10¹-10² Torr, and growth temperatures near 1100 K. CVD diamond size can, in principle, be enlarged to the wafer scale, but has not yet been possible.

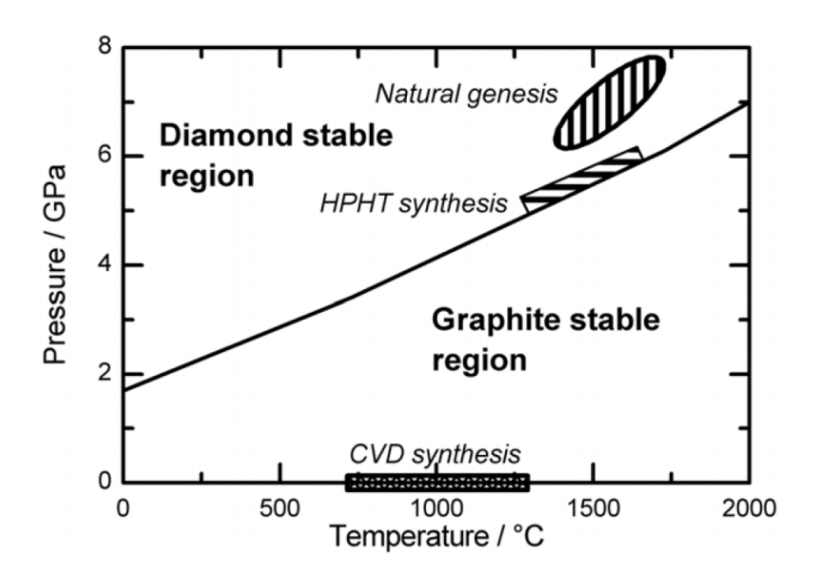


Figure 2.7 Pressure-temperature diagram of carbon.²⁷

2.5 Diamond types: Impurities

Because of its small lattice parameter, diamond can incorporate only few impurity species. The most common ones are boron and nitrogen. According to the included impurity types and their corresponding concentrations, diamonds can be classified into four types, listed in Table 2.2: Types Ia, Ib, IIa, and IIb. Most natural diamonds, 98%, are Type Ia. Diamond grown by the HPHT method belongs to Type Ib, which is yellow due to substitutional nitrogen. Type IIa diamonds are the cleanest, almost or entirely devoid of impurities. Hence, they are colorless.

Table 2.2 Diamond types according to impurities and corresponding concentrations.²⁸

Diamond type	Boron (ppm)	Nitrogen (ppm)	Color
Ia	-	2000	Clear to yellow
Ib	-	$10-10^3$	Green, brown, yellow
IIa	-	~1	Colorless clear
IIb	~100	~	Blue

3. Chapter 3 Characterization methods

3.1 Scanning electron microscopy

The scanning electron microscope (SEM) is in some ways similar to an optical microscope, replacing light with an electron beam to achieve nanoscale resolution. It uses a focused electron beam, with wavelength 10 pm, which is rastered across a small area, forming an image of the sample surface (Figure 3.1).

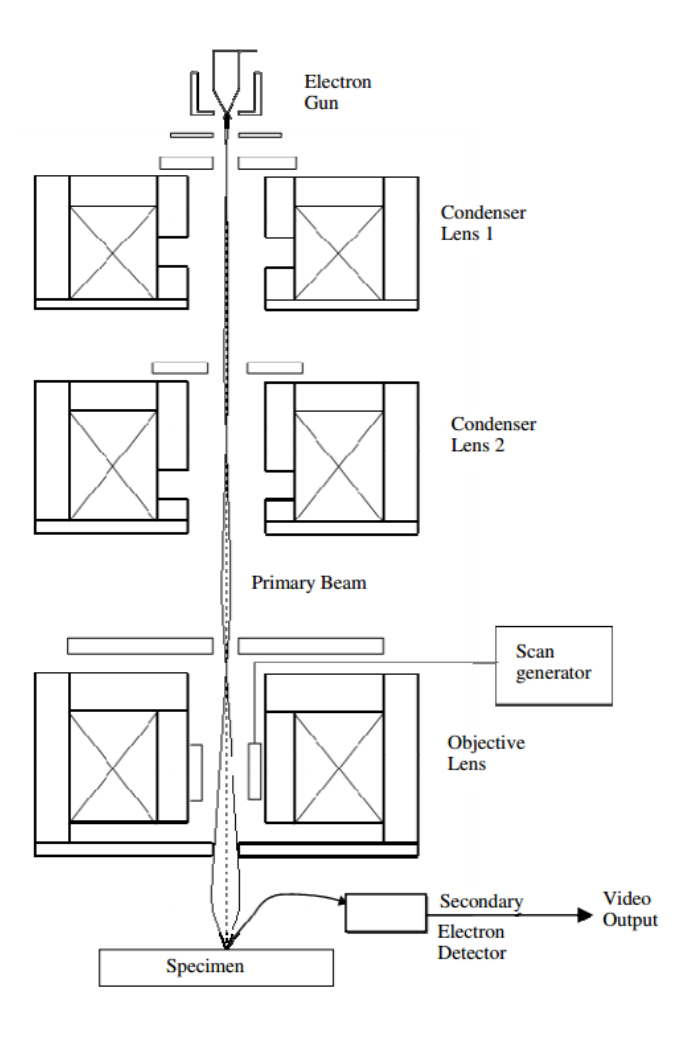


Figure 3.1 Schematic of a scanning electron microscope (SEM).²⁹

In a field emission SEM, the gun is composed of a sharp tungsten tip, with radius smaller than 100 nm which serves as cathode, and an anode plate. A large electric potential difference applied across the electrodes creates a very high electric field at the tip, typically above 10⁷ V/cm. As a result, the electrons at the Fermi level tunnel through the potential barrier into vacuum. Typically, the beam crossover diameter for cold cathode emission is about 10 nm rather than 10 µm for the thermionic gun of a conventional SEM. The electron beam then passes through pairs of magnetic condenser lenses to be collimated, followed by magnetic objective lenses which determine the area for the electron-beam raster scan. FESEM requires fewer magnetoptics to focus the electron beam, yielding higher resolution and brightness, than thermionic SEMs.

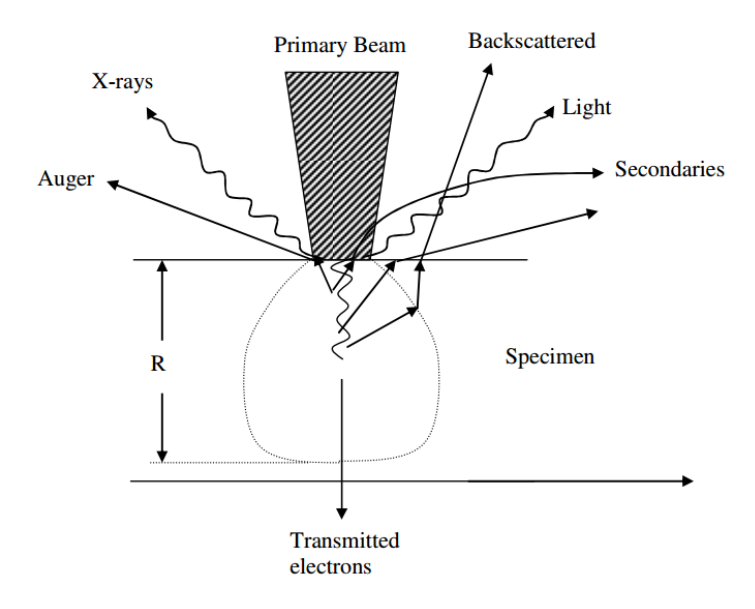


Figure 3.2 Interaction between primary beam and sample, where the range R depends on the primary beam energy and the specimen.²⁹

The electron beam impinging on the sample surface is called the primary beam. When the primary beam, with energy between 10-30 keV, strikes the sample surface, the electron-solid interaction produces a large number of scattered electrons and photons. Figure 3.2 illustrates the

interaction between the primary beam and the sample. Secondary electrons and backscattered electrons are the most important signals for SEM. The secondary electrons, in particular, are important in forming SEM images. They arise from weakly-bonded electrons close to the sample surface scattered by inelastic collisions, and typically have low energy, less than 50 eV. The detector, usually an Everhart-Thomley (E-T) type, accelerates the scattered electrons into a scintillator by applying positive bias on a collector grid. Photons are emitted and detected by a photomultiplier. The number of secondary electrons depends on the topographical features of the surface. Small particles, steep surfaces and edges enhance the emission. Therefore, the secondary electrons produce a higher resolution SEM image, relative to backscattered electrons, due to the large volume of interaction. SEM images described below have been acquired with a Hitachi 4700 II FESEM with a cold cathode field emission source.

3.2 Atomic force microscopy

An atomic force microscope is one of the scanning probe microscopies with very high resolution, on the order of 0.1 nm, used mainly to map surface topography. Instead of using light (optical microscope) or a focused electron beam (SEM), the probe is a sharp tip, with radius of 10 nm, attached to one end of a cantilever with a spring constant of order 1N/m. The scanning area, which depends on the instrument design, is typically a few 100 nm to a few 10 μm . According to the tip motion, the imaging modes of AFM can be classified as: contact, tapping and non-contact modes.

In this work, the Digital Instruments DI 3100 is used in tapping mode to image the sample topography. A Si tip is driven at the resonant frequency of the Si cantilever in air using a piezoelectric crystal.³⁰ The oscillating tip is then brought to near the sample surface. As the tip

scans the sample surface, the changes in topography cause damping of its oscillations. A photodetector captures the reflected light from a laser focused on the back side of the cantilever to track the tip movement. The amplitude of cantilever oscillation is maintained constant by a feedback loop in the system. Consequently, the surface topography is interpreted as a change of feedback signal amplitude. Figure 3.3 shows a schematic of the AFM system.

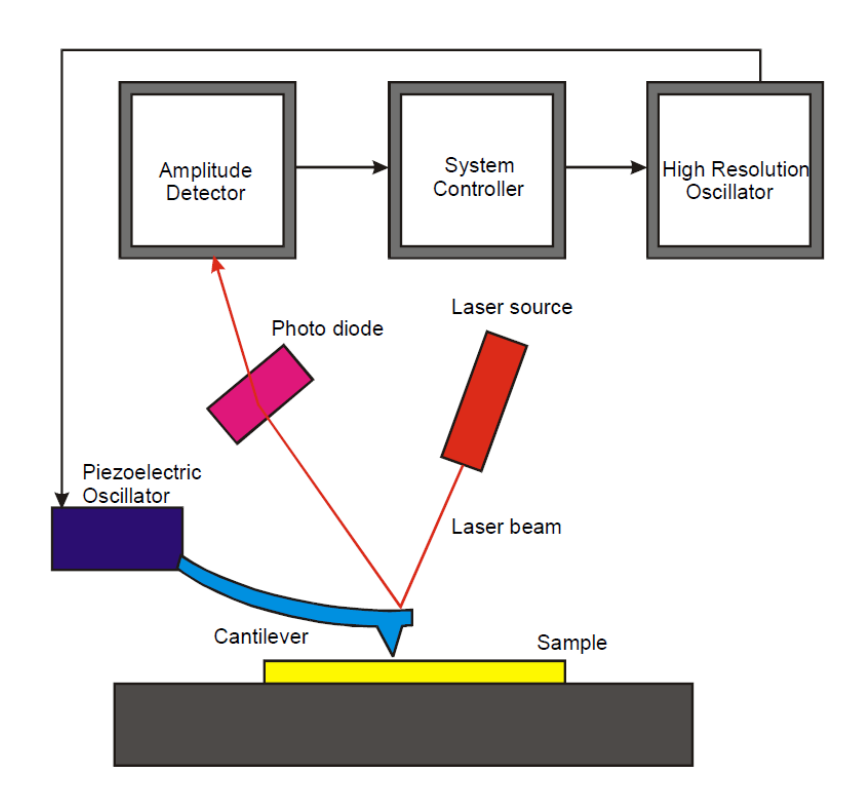


Figure 3.3 Schematic of Digital Instruments DI 3100 AFM in tapping mode.³¹

3.3 X-ray diffraction (XRD)

X-ray scattering enables scientists to probe crystalline structures at the atomic level, determining atomic arrangements and interatomic distances. For single crystal x-ray diffraction, the lattice planes of a crystalline specimen elastically scatter a monochromatic x-ray beam at a diffraction angle θ relative to the sample surface. A detector, which can be rotated in the scattering plane, records the intensity of the x-ray interferences while the incident beam rotates with respect to the sample. A typical XRD pattern plots the intensity of x-ray interferences as a function of 2θ , the angle between the incident and scattered beam. Figure 3.4 shows the schematic geometry of x-ray diffraction.

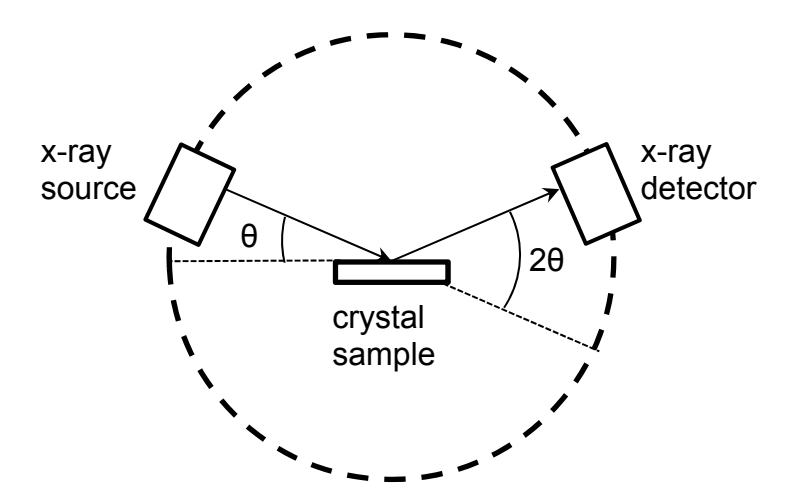


Figure 3.4 Schematic of XRD geometry.

In a diffraction pattern, strong peaks, which are constructive x-ray interferences, occur only at certain diffraction angles. By examining the path differences of the x-rays, the relation between wavelength λ , lattice spacing d, and the diffraction angle θ is found which is known as the Bragg condition: $n\lambda = 2dsin\theta$, where the integer n refers to the order of the diffraction. See Figure 3.5.

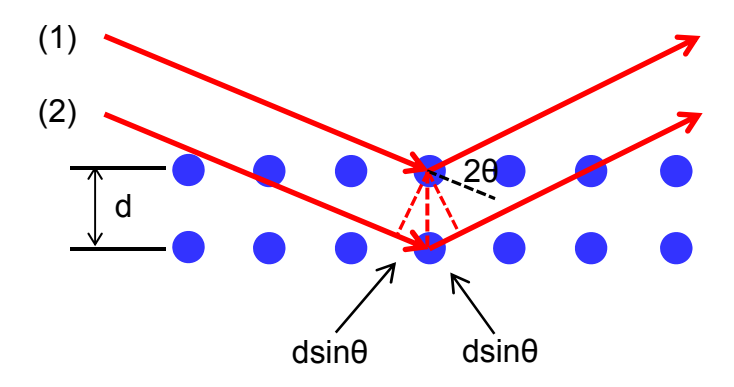
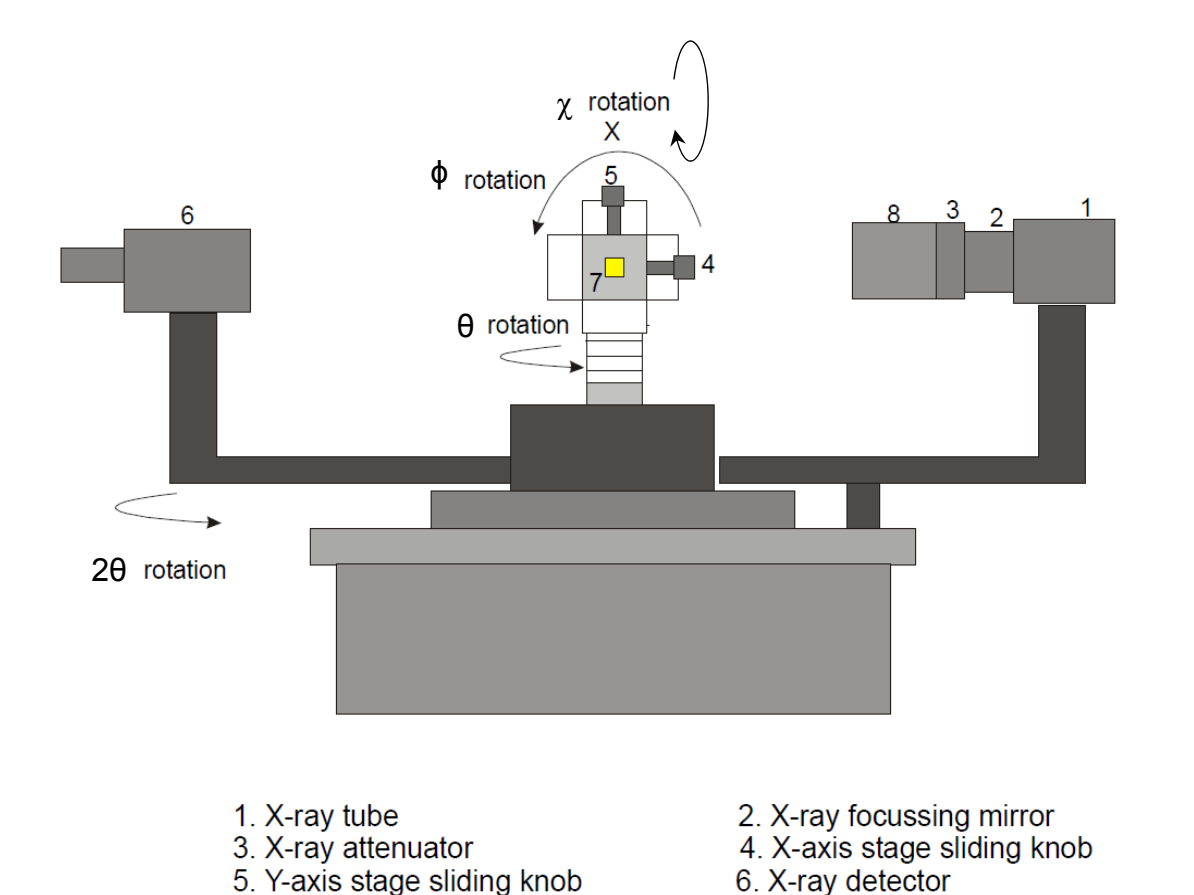


Figure 3.5 Illustration of Bragg condition. The solid circles represent a 2-D projection of the ordered atoms with lattice spacing d. Solid arrows are the incident and scattered x-ray beams with diffraction angle θ respect to the lattice plane. The path difference between ray (1) and (2) is $2dsin\theta$. If it equals an integer multiple of the x-ray wavelength, ray (1) and (2) will constructively interfere.

The Bruker AXS D8 instrument, Figure 3.6, with a 4-circle Eulerian cradle, is used for XRD measurements in this project. A Cu target serves as the x-ray source, producing Cu K_{α} and K_{β} radiation, the latter blocked by a Ni filter. For this diffractometer, the position of the incident beam is fixed, so the sample stage rotates to vary the diffraction angle. The stage has a vacuum chuck to hold the sample. The plane containing the incident and scattered beams is defined as the z plane or scattering plane. By moving the stage in the z direction, the converging beam can be focused at the sample surface; x and y translations position the beam on the sample. The stage rotates around three mutually perpendicular axes for precise alignment and rotational scans. ω -20 scans and rocking curves involve rotations about the x-axis, x-scans rotate about the y-axis, and the ϕ -scan rotates about the z-axis.



8. Germanium monochromator

Figure 3.6 Schematic of Bruker AXS D8 x-ray diffractometer. 31

7. rotatable sample stage

3.3.1 Rocking curve

In single crystal XRD, the rocking curve can be used to determine crystal quality. It is a θ or ω -scan with the detector fixed at the Bragg 2 θ angle. For an imperfect crystal, it is a Gaussian
peak whose full-width at half-maximum (FWHM) is a measure of the mosaic spread. Defects,
such as dislocations and impurities, will broaden the linewidth. A small linewidth and a
symmetric Gaussian peak are indications of crystal quality.

3.4 Raman spectroscopy

When an incident light beam with frequency v_0 , usually in the UV-visible region, impinges on a specimen, a small fraction of photons, typically 10^{-5} , is scattered inelastically, i.e., with a small frequency shift. This phenomenon was first discovered by C. V. Raman in 1928. The frequency differences, called Raman shifts, were found to be consistent with the vibrational modes of the molecule. In a Raman spectrometer, the scattered light is dispersed by a grating and is sent to a multichannel analyzer. The output of the analyzer is the inelastic spectrum, i.e., the number of photon counts per time interval, or intensity, as a function of photon energy, usually expressed in wave numbers, cm⁻¹, shifted from the laser frequency.

3.4.1 Theory of Raman scattering

Assume a sample is irradiated by a monochromatic incident light beam with an electric field E given by Eq. 3.1. If the electric susceptibility of the sample is χ , the local polarization P in the sample can be described by Eq. 3.2

$$E(\mathbf{r},t) = E(\mathbf{k},\omega)\cos(\mathbf{k}\cdot\mathbf{r} - \omega t)$$

$$P(\mathbf{k},\omega)\cos(\mathbf{k}\cdot\mathbf{r} - \omega t) = \chi(\mathbf{k},\omega,\mathbf{Q})E(\mathbf{k},\omega)\cos(\mathbf{k}\cdot\mathbf{r} - \omega t)$$

$$P(\mathbf{k},\omega) = \chi(\mathbf{k},\omega,\mathbf{Q})E(\mathbf{k},\omega)$$
3.1

where k and ω are the wave vector and frequency of the incident light, respectively. \mathbf{Q} is a lattice displacement which can be expressed by the phonon wave vector \mathbf{q} and its frequency ω_o , in Eq. 3.3.

$$Q(r,t) = Q(q,\omega_0)\cos(q \cdot r - \omega_0 t)$$
3.3

We further expand the $\chi(k, \omega, Q)$ as a Taylor series,

$$\chi(\mathbf{k},\omega,\mathbf{Q}) = \chi_0(\mathbf{k},\omega) + (\partial \chi/\partial Q)_0 \mathbf{Q}(\mathbf{r},t) + \cdots$$
3.4

replacing χ in Eq. 3.2 with Eq. 3.4, and find that the polarization has a quasi-elastic part, the Rayleigh scattering, and an induced term caused by phonons, which is the Raman term.

$$P(r,t,Q) = P_0(r,t) + P_{ind}(r,t,Q)$$
 3.5

where P_{ind} is

$$P_{ind}(r, t, \mathbf{Q}) = (\partial \chi / \partial Q)_0 \mathbf{Q}(\mathbf{Q}, \omega) \cos(\mathbf{k} \cdot \mathbf{r} - \omega_0 t) \mathbf{E}(\mathbf{k}, \omega) \cos(\mathbf{k} \cdot \mathbf{r} - \omega t)$$
 3.6

Eq. 3.6 can be further expressed as

$$P_{ind}(\mathbf{r}, t, \mathbf{Q}) = \frac{1}{2} (\partial \chi / \partial Q)_0 \mathbf{Q}(\mathbf{Q}, \omega) \mathbf{E}(\mathbf{k}, \omega) \{ \cos[(\mathbf{k} - \mathbf{q}) \cdot \mathbf{r} - (\omega - \omega_0) t] + \cos[(\mathbf{k} + \mathbf{q}) \cdot \mathbf{r} - (\omega + \omega_0) t] \}$$
 3.7

The first cosine term is called the Stokes process, corresponding to 1-phonon creation. The second cosine term, the anti-Stokes process, corresponds to 1-phonon annihilation. If the system is in thermal equilibrium, the vibrational state populations are given by the Planck factor, so that the anti-Stokes line is weaker than the Stokes line. Figure 3.7 shows the scattered spectrum for three vibrational frequencies.

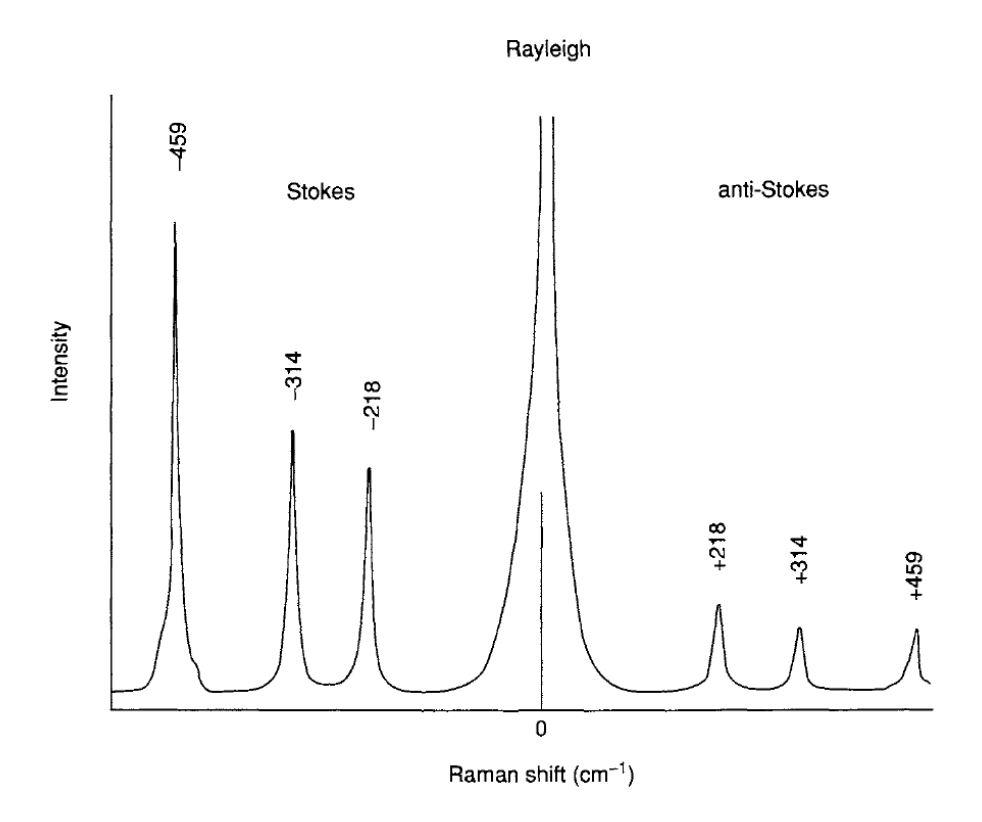


Figure 3.7 Raman spectrum of CCl₄ (488 nm excitation), showing Stokes and anti-Stokes spectra and the central Rayleigh scattering.³²

3.4.1.1 Polarized Raman spectroscopy

The term $(\partial \chi/\partial Q)_0 \hat{Q}(r,t)$ in Eq. 3.7 is known as the Raman tensor R. The intensity of Raman scattering can be written as

$$I = C \sum_{i} |\mathbf{e}_{i} \cdot \mathbf{R} \cdot \mathbf{e}_{s}|^{2}$$
3.8

where C is a constant, and e_i and e_s are unit polarization vectors of incident and scattered light, respectively. If this term is non-zero, it indicates that a phonon is "Raman-active" and will appear in the spectrum. This can be viewed as a Raman selection rule.

The triply degenerate zone-center, $\mathbf{q} \approx 0$, optical phonons of diamond have F_{2g} symmetry³³: One longitudinal phonon (LO) and two transverse phonons (TO) propagate along $\mathbf{q} = \mathbf{k}_i \cdot \mathbf{k}_s$, where \mathbf{k}_i and \mathbf{k}_s are the propagation direction of incident and scattered light, respectively. For these phonons, the Raman tensors $\mathbf{R}_j^{34,35}$, referred to the cubic axes $x \parallel [100]$, $y \parallel [010]$, and $z \parallel [001]$, are

$$\mathbf{R}_{x} = \begin{pmatrix} 0 & 0 & 0 \\ 0 & 0 & d \\ 0 & d & 0 \end{pmatrix}$$
 for TO₁

$$\mathbf{R}_{\mathbf{y}} = \begin{pmatrix} 0 & 0 & d \\ 0 & 0 & 0 \\ d & 0 & 0 \end{pmatrix}$$
 for TO₂

$$\mathbf{R}_{\mathbf{z}} = \begin{pmatrix} 0 & d & 0 \\ d & 0 & 0 \\ 0 & 0 & 0 \end{pmatrix}$$
 for LO

where the matrix element d is a characteristic of the material. Specifically, $d = d\alpha/dq$ is the change in the polarizability, α , with displacement of the two sublattices along \mathbf{q} . For a diamond single crystal, the Raman intensity in the backscattered direction normal to a (100) crystal surface is a function of the angles of the incident and scattered light polarizations \mathbf{e}_i and \mathbf{e}_s . According to the selection rules, only two intensities, I_{\parallel} and I_{\perp} can be observed when $\mathbf{e}_i \parallel \mathbf{e}_s \parallel [110]$ or $\mathbf{e}_i \parallel [010]$ and $\mathbf{e}_s \parallel [100]$, respectively.

3.4.1.2 Stress measurements by polarized Raman spectroscopy

The triple degeneracy of optical phonons in diamond will be lifted by stresses which lower the cubic symmetry. The sources of stress in diamond will be discussed in Chapter 9. The new phonon frequencies are given by solutions of the secular equation, Eq. 3.9, which derives from the lattice dynamical equations.^{36,37}

$$\begin{pmatrix} p\epsilon_{xx} + q(\epsilon_{yy} + \epsilon_{zz}) - \lambda & 2r\epsilon_{xy} & 2r\epsilon_{xz} \\ 2r\epsilon_{xy} & p\epsilon_{yy} + q(\epsilon_{xx} + \epsilon_{zz}) - \lambda & 2r\epsilon_{yz} \\ 2r\epsilon_{xz} & 2r\epsilon_{yz} & p\epsilon_{zz} + q(\epsilon_{yy} + \epsilon_{xx}) - \lambda \end{pmatrix} = 0 \quad \mathbf{3.9}$$

with $\lambda_i = \omega_i^2 - \omega_0^2$, i = 1, 2, 3, and $\Delta \omega_i = \omega_i - \omega_0 \sim \lambda/2\omega_0$, the stress-dependent Raman shift. The ϵ_{ij} are elements of the strain tensor ϵ referred to the cubic crystal axes, $x \parallel [100]$, $y \parallel [010]$, $z \parallel [100]$, and p, q, r are the deformation potential constants, related to the change in the spring constant due to the stress. To simplify the solutions, we only consider the cases with high symmetry: biaxial stress in (001), (110), and (111) planes and uniaxial stress along [100], [110], and [111] directions.

The in-plane biaxial stress σ can be expressed as a matrix in Eq. 3.10,

$$\sigma = \tau \cdot \begin{pmatrix} 1 & 0 & 0 \\ 0 & 1 & 0 \\ 0 & 0 & 0 \end{pmatrix}$$
 3.10

where τ is the stress amplitude. The strain tensor can be found by using Hooke's law $\epsilon_i = S_{ij}\sigma_j$, where the S_{ij} are elements of the elastic compliance tensor. Inserting the numbers of the three independent S_{ij} elements³⁸ for cubic symmetry and those of p, q, and r³⁹ in Eq. 3.9, the Raman

shift of each stress-shifted phonon mode can be calculated, Appendix. ^{35,39,40} In addition, the corresponding intensities can be calculated from Eq. 3.8, the Raman selection rules.

Therefore, using polarized Raman spectroscopy, the stress-shifted contribution to the Raman tensor can be found. In other words, by measuring the Raman peak shift, the stress state in a sample can be calculated. The results for different combinations of incident and scattered polarizations for backscattering geometry, $\mathbf{k}_i \parallel \mathbf{k}_s \parallel [001]$, are summarized in Table 3.1 and Table 3.2 from (001) and (110) surfaces, respectively. The Porto four-letter notation is used⁴¹: the first two letters indicate the direction and the polarization of the incident light, and the last two give the polarization and direction of the analyzed scattered light.

Table 3.1 Raman selection rules for backscattering from a (001) surface, with x'||[110], y'||[-110], and z'||[001].³⁵

Biaxial stress in a (001) plane or uniaxial stress along [001]				
Measurement geometry	TO_1 (doublet \parallel [100])	TO ₂ (doublet [010])	LO (singlet [001])	
z'(x'x')z'	0	0	d^2	
z'(x'y')z'	0	0	0	
z'(y'y')z'	0	0	d^2	
Bia	axial stress in a (110) plane	or uniaxial stress along [110]	
Measurement geometry	TO ₁ (doublet [100])	TO ₂ (doublet [010])	LO (singlet [001]	
z'(x'x')z'	d^2	0	0	
z'(x'y')z'	0	0	0	
z'(y'y')z'	d^2	0	0	
For the case	e of biaxial stress in a (111)	plane or of uniaxial stres	ss along [111]	
Measurement geometry	TO ₁ (doublet [100])	TO ₂ (doublet [010])	LO (singlet [001]	
z'(x'x')z'	$(1/3)\cdot d^2$	0	$(2/3) \cdot d^2$	
z'(x'y')z'	0	0	0	
z'(v'v')z'	$(1/3) \cdot d^2$	0	$(2/3) \cdot d^2$	

Table 3.2 Raman selection rules for backscattering from a (110) surface, with x'||[110], y'||[-110], and z'||[001].³⁵

Biaxial stress in a (001) plane or uniaxial stress along [001]				
Measurement geometry	TO ₁ (doublet [100])	TO ₂ (doublet [010])	LO (singlet [001])	
z'(x'x')z'	0	0	d^2	
z'(x'y')z'	0	0	0	
z'(y'y')z'	0	0	d^2	
Bia	axial stress in a (110) plane	or uniaxial stress along [[110]	
Measurement geometry	TO ₁ (doublet [100])	TO ₂ (doublet [010])	LO (singlet [001])	
z'(x'x')z'	d^2	0	0	
z'(x'y')z'	0	0	0	
z'(y'y')z'	d^2	0	0	
Bia	axial stress in a (111) plane	or uniaxial stress along [[111]	
Measurement geometry	TO ₁ (doublet [100])	TO ₂ (doublet [010])	LO (singlet [001])	
z'(x'x')z'	$(1/3)\cdot d^2$	0	$(2/3)\cdot d^2$	
z'(x'y')z'	0	0	0	
z'(y'y')z'	$(1/3)\cdot d^2$	0	$(2/3)\cdot d^2$	

3.4.2 Micro-Raman spectral method

The Raman spectra presented later were measured by a Kaiser Optical Systems HoloProbe Raman spectrograph, coupled to an Olympus BX-60 optical microscope with 100X objective and 532 nm laser excitation. The polarized Raman measurements used a fixed polarization for the incident beam and a $\lambda/2$ plate to rotate the polarization of the scattered beam. Spatial resolution was approximately 1.5 μ m. The system has two interchangeable gratings: a low-resolution grating with spectral range 0 to 4000 cm⁻¹, and a high-resolution grating with range 1000 to 1600 cm⁻¹. The instrumental resolutions for high- and low-resolution gratings are 2 and 5 cm⁻¹, respectively. The Raman spectrum from a nearly-perfect Type IIa natural diamond was used as a reference, with peak position at 1332.4 cm⁻¹ and a linewidth of 1.65 cm⁻¹. Figure 3.8 shows the background-subtracted polarized Raman spectra of the reference, taken with the high-resolution grating. The apparent breakdown of the selection rules is a result of imperfect polarizers.

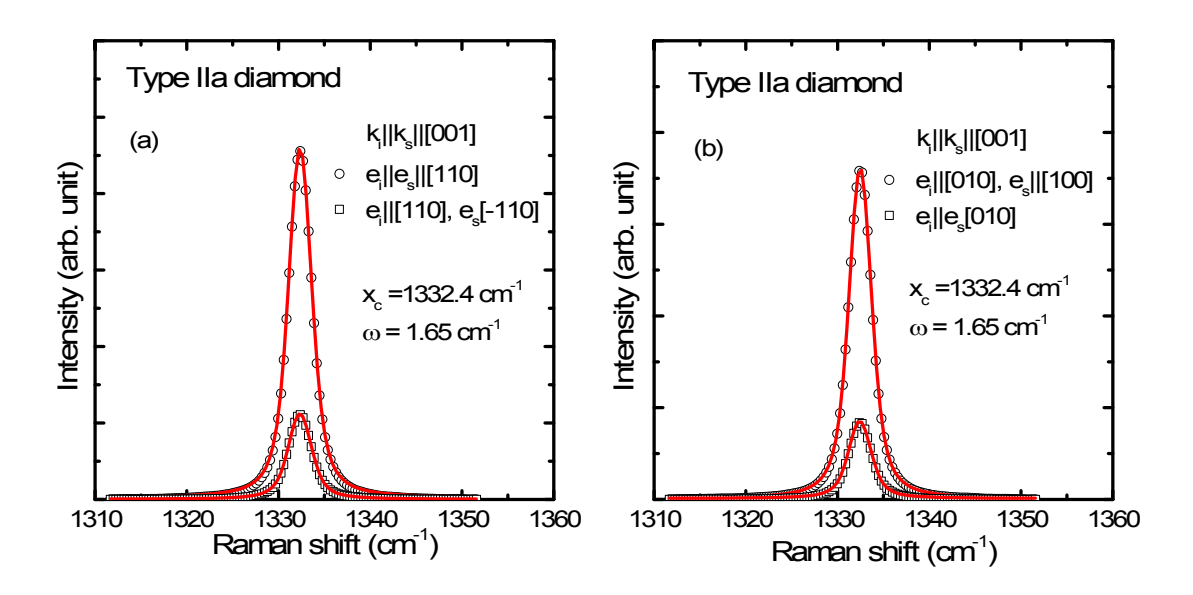


Figure 3.8 Raman spectra of Type IIa natural diamond in [001] backscattering geometry. (a) For $e_i \parallel [110]$, only polarization of incident light parallel to the polarization of scattered light, $e_s \parallel [110]$, is allowed. (b) For $e_i \parallel [010]$, the polarization of the scattered light must be perpendicular to the polarization of the incident light, $e_s \parallel [100]$. Due to a polarization "leak", the measured intensity is non-zero for forbidden polarizations.

3.4.2.1 Spectrum analysis

Analysis of the Raman scattering peak in diamond used the following process: (1) a fairly large region about the peak is identified, (2) the background is subtracted and (3) the peak is fitted, using a non-linear least squares method. The ranges analyzed are 1250-1410 cm⁻¹ and 1310-1350 cm⁻¹ for low- and high-resolution Raman spectra, respectively. In the range of interest, it is sufficient to take a linear background, found by interpolation from the intensities at the two ends of the range. The Raman linewidth contains a contribution from instrumental resolution. The instrumental contribution is taken to be a Gaussian function whereas the Raman spectrum of

diamond is a Lorentzian function. The instrumental resolution function was found by measuring the Raman spectra of a high-quality single crystal Si substrate and a Type IIa natural diamond, which have well-established linewidths at room temperature. After deconvolution, the instrumental Gaussian FWHM was found to be 2 and 5 cm⁻¹, for high- and low-resolution gratings, respectively. Accordingly, the background-subtracted modified spectra were fitted by a Voigt function, a convolution of a Gaussian and a Lorentzian function.

3.4.2.2 Spatial Raman scanning

Lateral scans of the incident beam across a sample are performed with a motorized sample stage, with spatial resolution 1.5 µm. Data were taken point-by-point, making sure that the incident beam focal point was at the sample surface. Spectra were acquired with counting times of approximately 10 sec. Scans were performed on diamond {100} and {110} surfaces in backscattering geometry. For spectra taken from (001) planes, the incident laser beam is parallel to the $[001]_{dia}$ axis, and only the scattered light propagating parallel to $[00\bar{1}]_{dia}$ direction is collected, i.e, $k_i \parallel k_s \parallel <100>_{dia}$. According to selection rules, Eq. 3.8, there are two ways to arrange the input and output polarization: input and output polarizations are parallel to [110], $e_i \parallel e_s \parallel$ [110] or are perpendicular to each other, $e_i \parallel$ [010] and $e_s \parallel$ [100], as shown in Figure 3.8. For spectra collected from a (110) surface, $e_i \parallel e_s \parallel$ [110] or $e_i \parallel$ [110] and $e_s \parallel$ [001]. For the CVD diamond grown with the epitaxial lateral overgrowth (ELO) method, Raman lateral scans were used to compare the Raman linewidth and frequency of non-overgrown and overgrown regions.

4 Chapter 4 Plasma-assisted heteroepitaxial growth

4.1 Properties of plasma

Plasma is a collection of ionized gas species, with coexistence of positive and negative charges, created when sufficient energy is provided. It shows charge neutrality on a macroscopic scale, preserved by the rearrangement of charges in the plasma to shield external and internal electrostatic fields. Within the Debye length, λ_D , significant departures from charge neutrality can occur,

$$\lambda_D = 743 (T_e/n_e)^{1/2} \text{ (cm)}$$
4.1⁴²

where T_e is the electron temperature, expressed in electron volts eV (1eV=11600K) and n_e is the electron density (cm⁻³). For a typical microwave plasma discharge, $T_e \approx 5 \ eV$ and $n_e \approx 10^{12} \ cm^{-3}$ resulting in $\lambda_D \approx 0.02 \ mm$. Figure 4.1 shows the relation between electron number density and temperature.

4.1.1 Glow discharge

A glow discharge, a kind of plasma, is created at a reduced pressure when an electric potential, DC or AC, applied across two metal electrodes exceeds a threshold, weakly ionizing a low-pressure gas. In a glow discharge, the electrons, having much higher energy than ions, $T_e \gg T_i$, are colliding with gas molecules and ionize them at lower temperature.

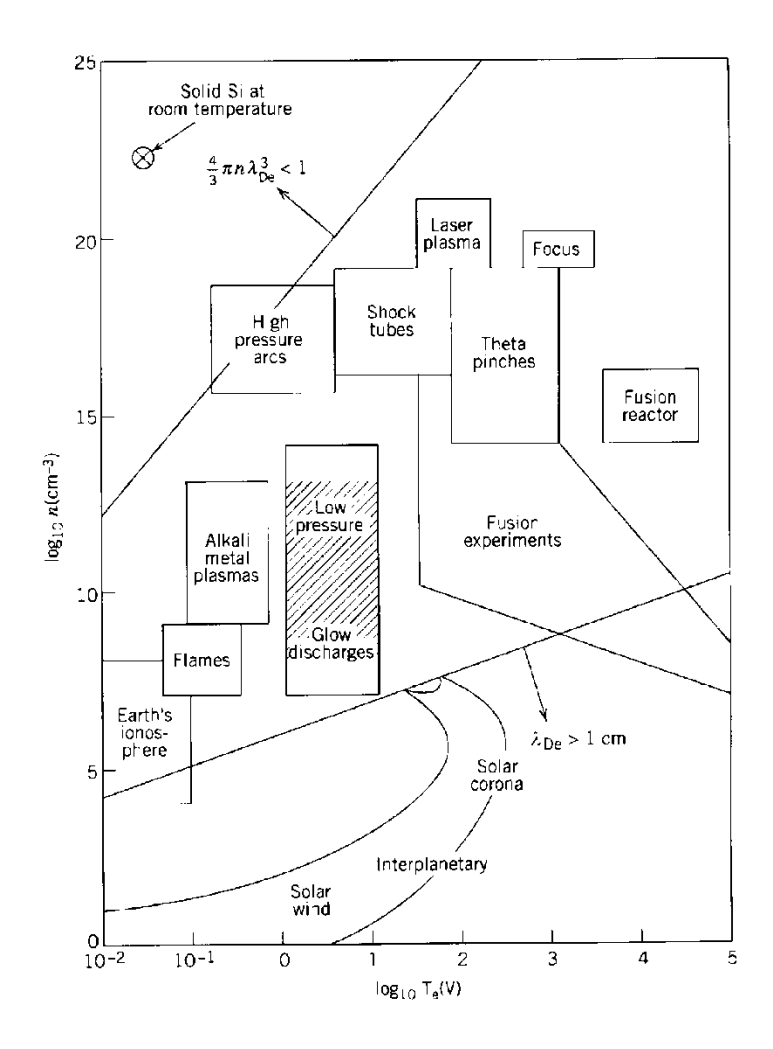


Figure 4.1 n_e vs. T_e for different plasmas.⁴³

Figure 4.2 illustrates a DC glow discharge in a tube where the features are characterized by luminosity, potential, field strength, space charge density and current density. The cathode region comprises the Aston dark space, the cathode glow and the cathode dark space in the middle. The negative glow is next to the cathode region. It has the highest current density, thus the highest brightness. The Faraday dark space and the positive column are next to the glow on the anode side. The latter is considered to be the main discharge because it generally extends to the anode side, occupying most of the entire glow volume. In the anode region, there consists the anode dark space and anode glow.

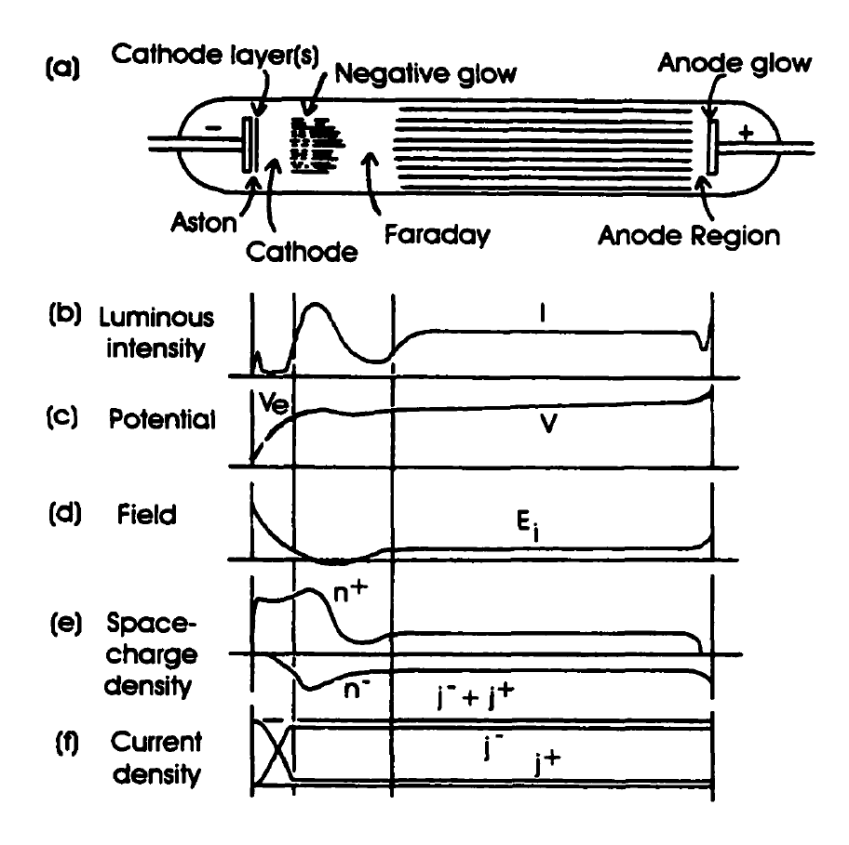


Figure 4.2 A glow discharge tube and its major characteristics. 44

4.2 DC magnetron sputtering

Sputtering deposition, one of the physical plasma depositions which only involves a phase transition at the substrate surface, is a process in which the positive ions, extracted from a discharge, are accelerated by an electric potential, ranging from a few hundred to a few thousand volts, toward to a neutral or negatively biased electrode, i.e. the target. Atoms are ejected after the ions strike the target surface and the ejected atoms condense on the substrate. In magnetron sputtering deposition, electrons in plasma are trapped near the target with a closed magnetic field and the substrate is placed in proximity to the magnetron sputtering cathode. It consequently, results in an enhancement of the initial ionization which allows plasma formation at rather low

pressure, several mTorr. At low pressure, voids incorporated into the growing layer are reduced. For a conductive material a DC electric field is applied; otherwise, a RF (typically 13.56 MHz) power supply is used. In this dissertation, two sputtering systems were used for sputtering processes—the AJA and APX instruments. The AJA system was used exclusively for Ir epitaxy to avoid contamination and the APX system was used for back and side coatings of Ir on a-ALO substrate, described in Chapter 7.4.

4.2.1 Configurations of AJA sputtering system

The AJA sputtering system was acquired from AJA international. The system body contains two chambers separated by an exchange valve (VAT), Figure 4.3, a load-lock chamber for sample loading, and the main chamber where the sputtering takes place. Each chamber is connected to a dedicated Pfeiffer turbomolecular pump (TMP), each of which is backed by a dry roughing pump. The lowest base pressure in the main chamber is 2×10^{-8} Torr. A transfer arm moves the sample holder from load lock to main chamber, allowing the main chamber to always remain at low pressure.

This system is designed for upward sputtering, which tends to suppress particulate contamination. The system is equipped with two DC and one RF sputtering guns located at the bottom of the main chamber. The maximum powers of the DC and RF guns are 750W and 300W, respectively. The sample plate is mounted on a shaft extending from the top plate and faces downwards toward the sputtering guns. A variable speed rotating "propeller" engages the sample plate or "puck", allowing for substrate rotation during sputtering improving deposition homogeneity. A motorized gate valve shutter is at the inlet of the TMP to the main chamber so that the process pressure can be controlled. The sputtering gas used is ultrapure Ar (99.999%)

from a pressurized cylinder. The stainless steel gas line from the tank is always pressurized to eliminate external contamination. Two quartz lamps behind the sample holder serve as a heater with a maximum temperature at the sample plate of 850 °C. A thermocouple near the sample plate monitors its temperature. Additional details are given in Chapter 7.2.

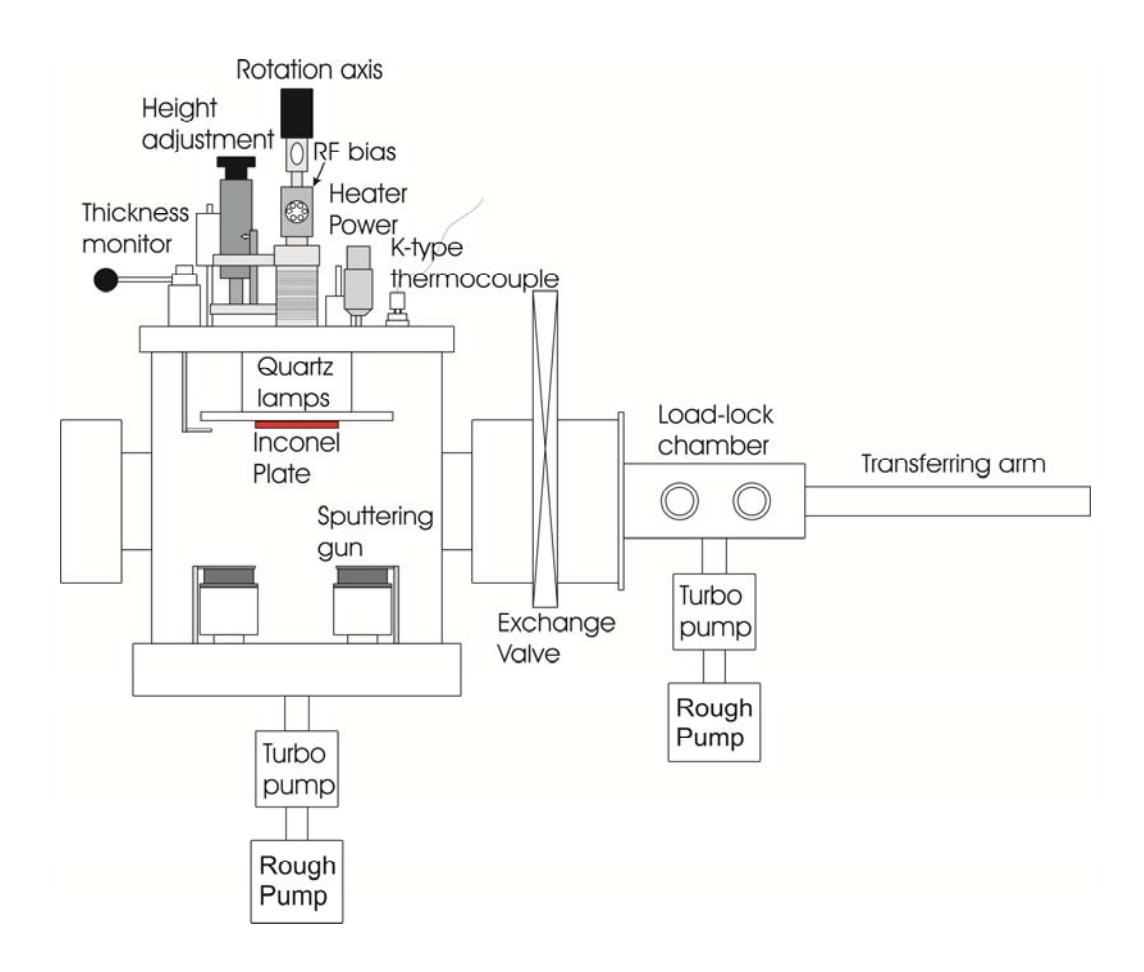


Figure 4.3 Schematic of AJA sputtering system.

4.2.1.1 Oxidation issue in AJA

A uniform discoloration of the Inconel sample plate was observed after sputtering. To identify the material, Raman spectra were collected from the plate surfaces which suggested transition metal oxides. Suspecting an air leak, a mass spectrometer helium leak detector was connected to the outlet of turbo pump. A few extremely small leaks were identified and fixed. The discoloration on the sample plate, however, was still present after heating to 850 °C in several mTorr Ar; it did not appear after the plate was heated in a vacuum near 10⁻⁸ Torr. The problem has not been fully solved, but it appears that impurities in the Ar may the source. The discoloration did not appear to affect Ir epitaxy.

4.3 Chemical vapor deposition (CVD)

Chemical vapor deposition proceeds by a chemical reaction, or a set of reactions, near a substrate surface. The CVD processes can be categorized into two types: thermal and activated. ⁴⁵ In thermal CVD, near thermal equilibrium, the chemical reaction of the gas flow is initiated on a hot substrate surface. In activated CVD, far from thermal equilibrium, the reactions are kinetically controlled. Thus, an external energy source, such as a hot filament or plasma, is required to ionize the gas species. For plasma-assisted CVD (PCVD), the types of chemical reactions on the substrate depend strongly on the properties of the plasma. CVD makes the deposition possible, at relatively low temperatures, of a large variety of elements and compounds in the form of both amorphous and crystalline layers.

4.3.1 Configurations of the CVD reactor

Figure 4.4 shows a schematic diagram of the microwave plasma assisted CVD reactor used for heteroepitaxial diamond thin film growth. This reactor will be referred to as "the CVD system". The CVD system comprises four sections: (1) energy source (2) gas handling system (3) water-cooled sample stage, and (4) computer automation.

4.3.1.1 Energy source of CVD reactor

The energy source is a 2.45 GHz microwave generator whose magnetron is capable of outputting a maximum power of 7 kW (Cober SF6). A rectangular waveguide and coaxial transition direct the microwaves to a cylindrical brass cavity. The cavity can be tuned to the microwave frequency by a movable end plate and coupling can be varied with an electrostatic probe. The cavity is operated in its TM_{013} mode, which creates a plasma above the substrate surface in a hemispherical quartz dome, as shown in Figure 4.5.

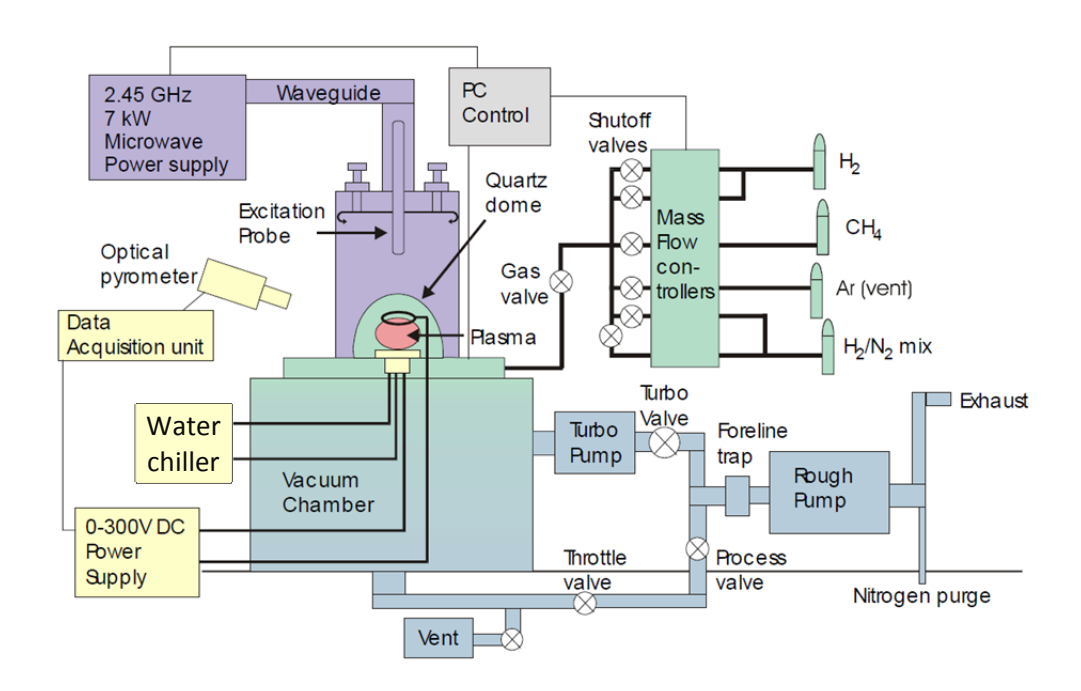


Figure 4.4 Schematic of the microwave plasma-assisted CVD (MPCVD) system for heteroepitaxial diamond growth.⁴⁷

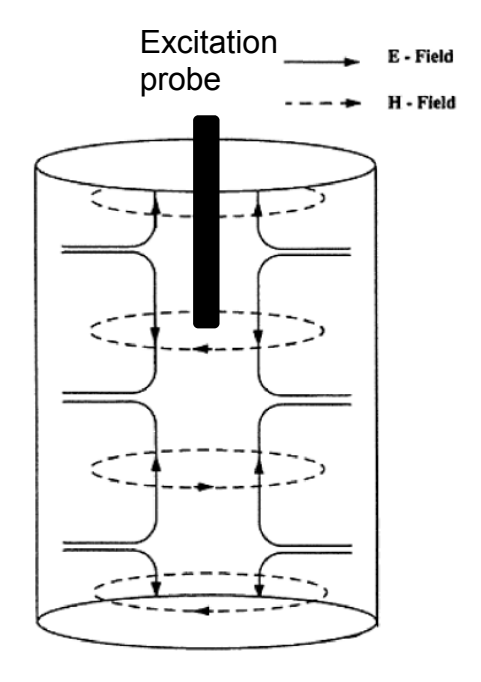


Figure 4.5 Illustration of the TM_{013} electromagnetic mode inside a cavity.⁴⁸ Solid lines represent electric fields; dashed lines the magnetic fields.

4.3.1.2 Gas handling of CVD reactor

The gas sources for the CVD system are ultrahigh purity hydrogen (99.9995%) and methane (99.99%). Prior to starting a growth process, the reaction chamber, the quartz dome and the stainless steel vacuum chamber are pumped down by a water-cooled Pfeiffer TMP through a VAT gate valve. An Alcatel, Fomblin filled, oil pump serves as backing for the TMP and as a process pump during growth. The reaction gases are mixed in a stainless steel manifold before flowing into the main chamber; flow rates are controlled by individual MKS mass flow controllers. A MKS type 635 throttle control valve interfaced to a pressure controller (MKS 651C) maintains the process pressure between 0-100 Torr. For safety, exhaust gases are purged with compressed N₂ gas at the outlet of the roughing pump before being exhausted.

4.3.1.3 Biasing set up and circuit

A water-cooled stainless steel sample stage keeps the substrate cool so that high microwave powers can be used. The bias set up fixturing is shown in Figure 4.6. During biasing, an external DC power supply (Kepco, 0-300V/0-200 mA) applies a voltage to the substrate. A grounded tungsten ring immersed in the plasma serves as a return path for the bias current. Figure 4.7 shows the circuit for biasing. Two 50 Ω resistors are serially connected in the bias circuit to suppress arcing and to monitor the current.

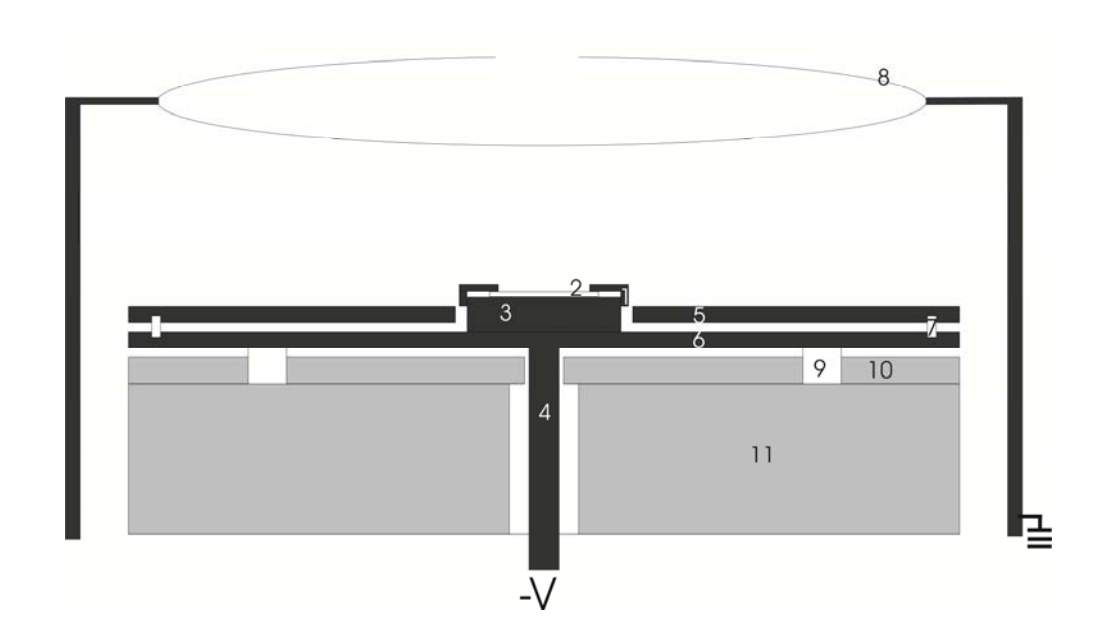


Figure 4.6 Schematic of bias set up in CVD reactor with: (1) Mo cap (2) Ir/a-ALO substrate (3) Mo post (4) bias lead (5) Mo shield (6) Mo base plate (7) ceramic spacer (8) tungsten bias ring (9) ceramic spacer (10) grounded stainless steel spacer (11) cooling stage.

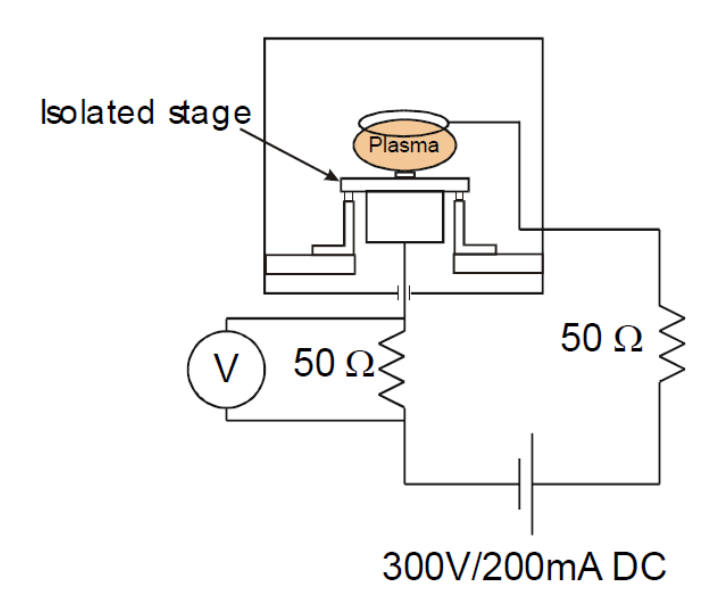


Figure 4.7 Illustration of bias circuit.⁴⁷

4.3.1.4 Computer controlling/monitoring system

All CVD processing is controlled by a PC running Labview, which also records the process parameters in a data file at short time intervals. Prior to a growth run, a stage file is prepared with input parameters: gas flow rates, process pressure, and stage duration. The typical growth parameters monitored are given in Table 8.1. Temperature is measured by an optical pyrometer through a window of the microwave cavity. The pyrometer is usually focused on the top surface of Mo cap, with emissivity ε =0.35.

4.3.1.5 Substrate loading in CVD reactor

The substrate is first placed on the Mo sample post which is then screwed into the Mo base plate attached to the bias lead; a Mo cap is placed on the substrate. The Mo plate rests on ceramic spacers for isolation. The assembly is placed onto the cooling stage. A stand, which resides in the bell jar below the microwave cavity, supports the cooling stage for easy access. Finally, the entire fixture, including the cooling stage, is slid vertically and is bolted to the bottom of the cavity. Since the system is not equipped with a load lock, sample loading is always performed in air. Pump down from 1 atmosphere takes four hours to reach a pressure of 5×10^{-7} Torr. Overnight pumping allows the system to reach a base pressure of 2×10^{-7} Torr.

4.3.2 Configurations of AsTex reactor

The AsTex CVD system, henceforth "the AsTex system", was acquired from Seki Technotron (Japan), Figure 4.8. Only the reactor body and microwave source were supplied; the gas handling, vacuum system, and sample cooling stage were designed and constructed at MSU.

4.3.2.1 Energy source of AsTex reactor

The energy source is a 2.45 GHz microwave generator with a maximum output power of 1.5 kW. A triple-stub tuner impedance matches the source to the cylindrical cavity operated in its TM_{013} mode. The plasma is confined to the region just above the substrate, which is mounted on a variable-height stage. A quartz plate forms a window for the microwaves and provides a vacuum-tight seal to the main reactor chamber.

4.3.2.2 Gas handling of AsTex reactor

An air-cooled Pfeiffer TMP pump is backed by an oil roughing pump (Oerlikon Leybold) that exhausts the main chamber to a base pressure of 2×10^{-7} Torr. Mass flow controllers (MKS1249) control the gas flow. Pressure is controlled by a pressure controller (MKS type 653), with an interface (MKS type 651C), backed by the roughing pump. Exhaust gases are mixed with compressed N_2 before venting.

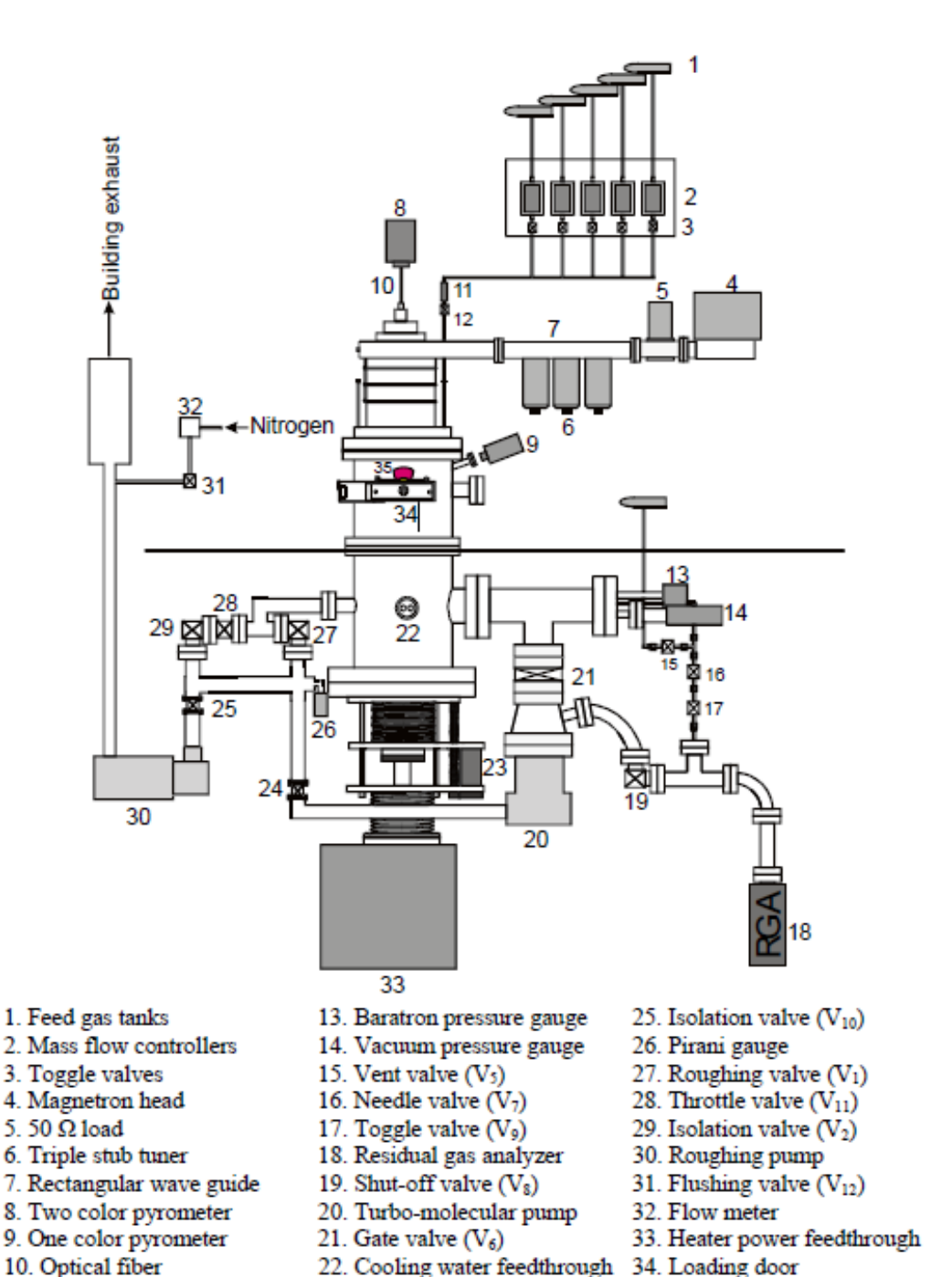


Figure 4.8 Schematic of AsTex system.³¹

12. Inlet gas valve (V₄)

Optical fiber
 Inline gas filter

23. Stage control motor

24. Backing valve (V3)

Growth chamber

4.3.2.3 Temperature measurement

The AsTex system is equipped with two types of optical pyrometers, located in different positions, to monitor the sample temperature. A two-color pyrometer (Williamson), which is sensitive to 2.2 and 2.4 µm IR radiation, is located above the substrate with a view of the substrate through a quartz plate. Optical fibers are used to transmit the IR radiation to a detector; a red-light laser beam is used to center the fibers on the substrate. The other pyrometer is a single color type (Ircon) that views the substrate through a side port window.

4.3.2.4 Substrate loading in AsTex reactor

Access to the growth chamber is through a small rectangular door. Figure 4.9 shows the reactor components relevant to diamond growth. A Mo sample post is threaded into the cooled stage, a substrate placed on the post, and the Mo cap placed over the substrate and post. A Mo shield resides above the cooling plate to protect it from the plasma. A corona ring placed over the edge of the shield suppresses microwave leakage below the stage. The entire stage is translated vertically to the growth position.

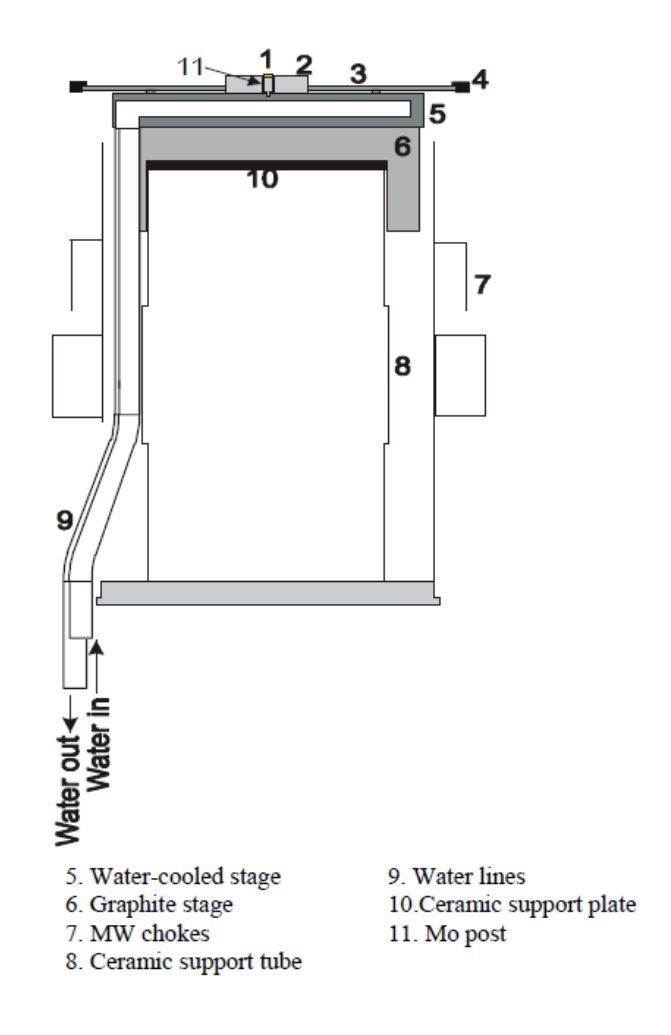


Figure 4.9 Illustration of the water-cooled sample stage in AsTex system.³¹

4.3.3 Diamond CVD methods

1. Substrate

2. Mo cap

3. Mo plate

4. Corona ring

As mentioned in Chapter 2.4, CVD opens the possibility for diamond crystallization in a thermodynamically metastable region. In early studies, formation of graphite and diamond were found to simultaneously occur during CVD growth. It was realized that suppressing graphite deposition was needed to improve diamond quality, which was achieved by preferential etching of graphite by atomic hydrogen.^{49,50,51} Therefore, CVD diamond growth has subsequently been conducted in a hydrogen-rich hydrocarbon gas mixture.

The model of CVD diamond growth considers the major reactants to be hydrogenated carbon radicals and atomic and molecular hydrogen. Hydrogen molecules are dissociated to atomic hydrogen by an external energy source, which also forms hydrocarbon radicals. The hydrocarbon radicals attach to the carburized hydrogen-terminated substrate surface by forming sp² or sp³ chemical bonds, accompanied with the detachment of hydrogen molecules. The formation of a diamond film takes place owing to the higher etching rate of sp² carbon relative to sp³ carbon by hydrogen. The primary chemical reactions are summarized in Eq. 4.2-4.4 and the illustration in Figure 4.10, where methane is an example of a hydrocarbon molecule:

$$H_2 \rightarrow 2H^0$$
 4.2

$$CH_4 + xH^0 \to CH_{4-x} + xH_2$$
 4.3

$$- \stackrel{\downarrow}{C} - H + CH_4 \rightarrow - \stackrel{\downarrow}{C} - \stackrel{\downarrow}{C} - H + yH_2$$
4.4

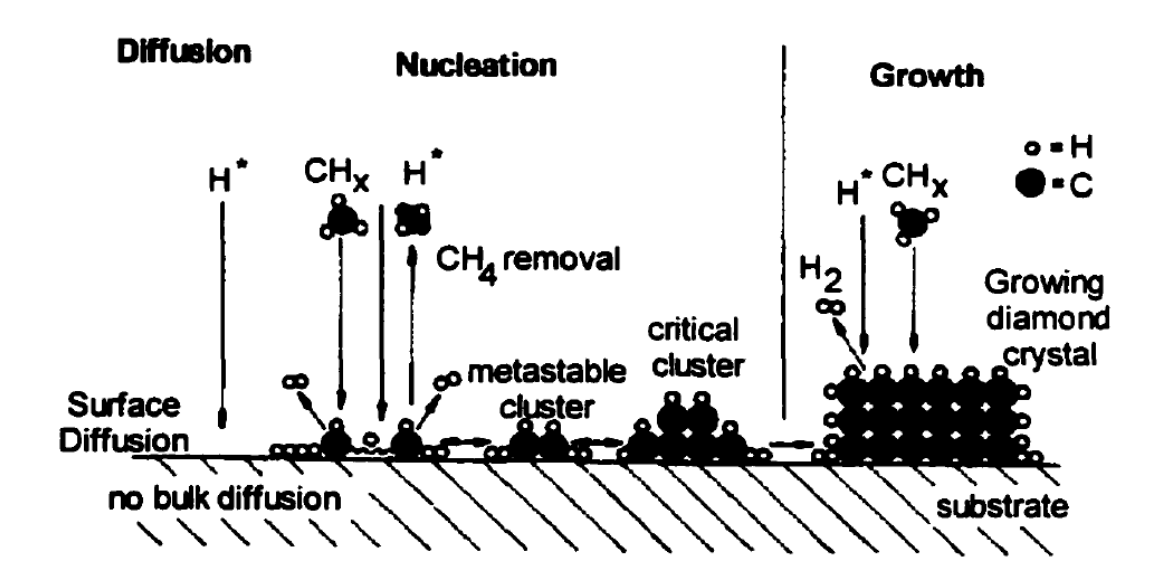


Figure 4.10 Illustration of model of diamond nucleation and growth on a substrate.⁴⁵

Prior to diamond growth, the treatment of the substrate surface differs for two epitaxial processes. A diamond substrate for homoepitaxy is prepared by acid cleaning and by plasma etching in an O₂/H₂ mixture to remove impurities and surface damage. The treatment of a non-diamond substrate surface for heteroepitaxy is quite different and will be discussed in detail in Chapter 5.4.

The first studies of diamond crystallization on non-diamond substrates, Si, Mo, and W (carbide-forming) and Cu, Au (non-carbide forming), were performed⁵² in a thermal CVD system. Later, diamond growth on hetero-substrates by microwave plasma-assisted CVD (MPCVD) and hot filament CVD (HFCVD) was demonstrated.^{53,54} MPCVD is advantageous for large-area deposition and high growth rates. In this dissertation, all diamond films were grown by MPCVD.

4.3.3.1 Effects of growth parameters

The variables for CVD diamond growth are: substrate temperature, methane concentration, process pressure, and microwave power density. To achieve high quality diamond epitaxial films, all the parameters have to be optimized. We summarize below how these growth conditions influence the outcome of a diamond film.

Substrate temperature depends mainly on plasma density which is controlled by absorbed microwave power and process pressure. In some CVD systems, an external heater may also be used. For homoepitaxial CVD diamond growth, the typical growth temperature is in a range of 700-1200 °C. In this temperature range, diamond growth is controlled by chemical kinetics rather than by surface diffusion. Figure 4.11 shows that the growth rate R_g , below 1000 °C obeys an Arrhenius relation, $R_g = Aexp(-E_a/k_BT_g)$, where T_g is the growth temperature and E_a is a facet-dependent activation energy. Generally, {100} planes have the highest E_a , leading to the slowest growth rate compared to other crystal planes. 55,56,57 At temperatures below 700 °C obeys are growth rate is low, resulting in highly pitted or non-epitaxial diamond. High quality CVD diamond growth exists only for a small range of growth parameters.

Hydrocarbon, e.g. methane, concentration is another major factor. It is usually denoted by the flow rate ratio of methane to hydrogen. The diamond growth rate is proportional to methane concentration over a significant range, Figure 4.12.

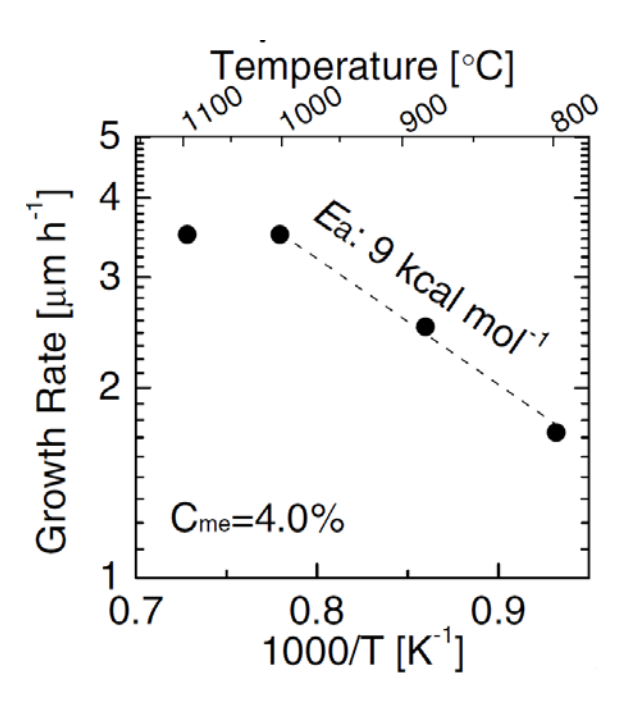


Figure 4.11 Diamond growth rate vs. growth temperature in 4% methane.⁵⁹ The growth rate follows the Arrhenius relation but saturates above 1000 °C.

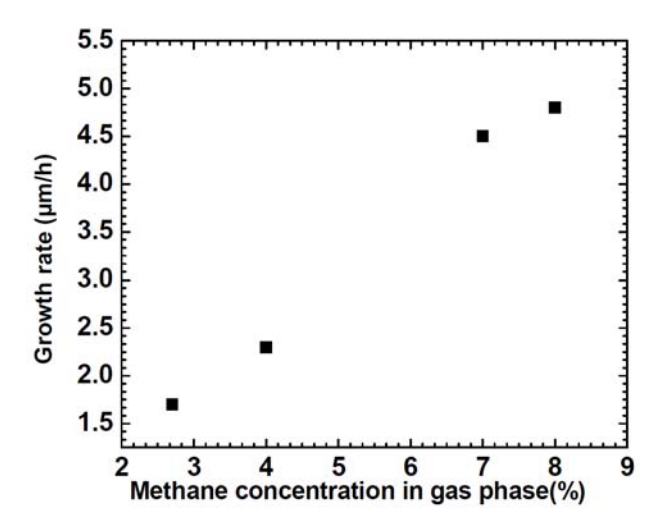


Figure 4.12 Diamond growth rate vs. methane concentration at 770 °C (upper two points) and 800 °C (lower two points).³¹

As the total gas pressure increases, the plasma volume shrinks, accompanied by a shorter mean free path. The plasma temperature increases owing to the higher possibility of particle collisions. In MPCVD the electrons are accelerated by the microwave electric field but the heavy ions cannot follow the frequency at pressures in the 1 to 10¹ Torr range. Thus, the plasma temperature in this regime is represented by the electron temperature. As pressure increases towards 10² Torr, both electron and ion temperatures increase, the plasma becomes hotter as electrons and ions thermalize. Due to the low density of excited radicals, the growth rate is low at low pressure. In the high pressure regime, the growth rate increases because of the higher densities of ionized species. In a pressure regime between 150-200 Torr, homoepitaxial diamond rates up to 40 um were observed.⁶⁰

The plasma volume is also microwave power dependent; it expands as microwave power increases. Growth rate generally increases with higher microwave plasma density. It was observed that increasing the plasma density from 65 to 125 W/cm³ led to a growth rate increase for diamond homoepitaxy from 3 to 8.5 μ m/hr.⁵⁹ Later work extended power densities from 300 to 1000 W/cm³, with growth rates of 20 to 75 μ m/h.⁶¹

4.3.3.2 Growth anisotropy: the α parameter

Diamond growth textures can be parameterized by the diamond growth parameter, α , defined as 62

$$\alpha = \sqrt{3} \, V_{100} / V_{111} \tag{4.5}$$

where V_{100} and V_{111} are the growth rates in the [100] and [111] directions. Figure 4.13 shows the shapes of diamond crystals for different α values. It is clear that, for α =1, the fastest growth is along [111] direction. Thus, the (111) plane will eventually vanish. For α =3, on the other hand, the growth rate along [100] direction becomes the fastest. Then, a diamond octahedron forms.

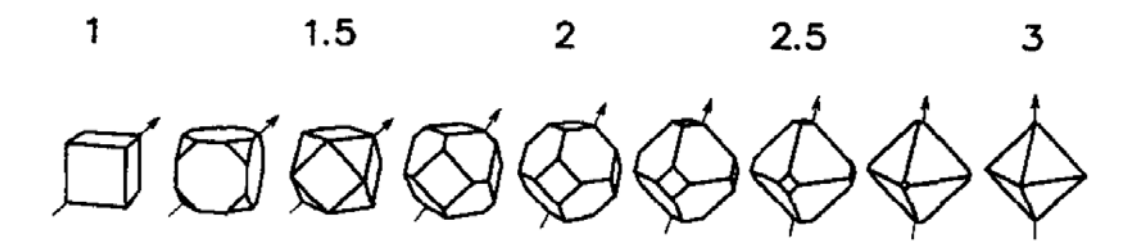


Figure 4.13 Shapes of diamond crystals for different values of α , the growth parameter. The arrow indicates the fastest growth direction for each case.⁶³

The dependence of α on temperature and methane concentration has been studied, Figure 4.14. However, the actual diamond growth mode is much more complicated, requiring other growth parameters to understand fully facet formation.⁶⁴

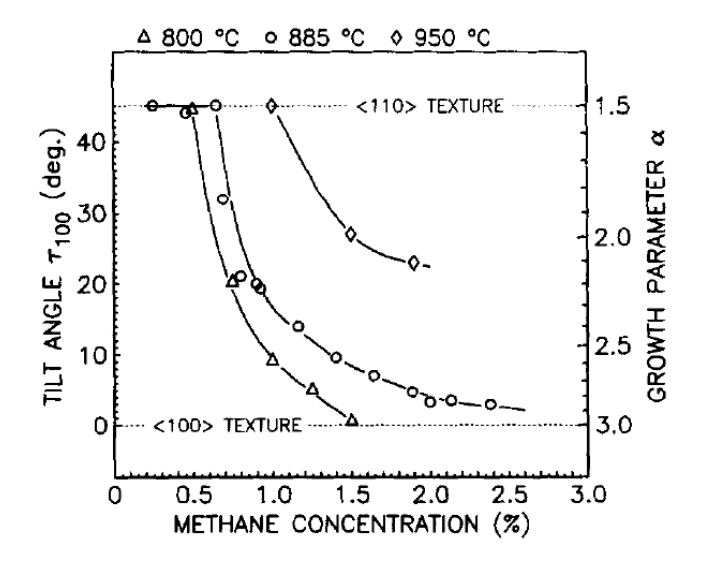


Figure 4.14 α vs. methane concentration at different temperatures.⁶³

5 Chapter 5 Diamond nucleation and heteroepitaxy

5.1 Nucleation

Nucleation is a prerequisite to crystal growth. It is a process whereby a substance undergoes a phase transition initiated by forming a small ensemble of atoms or molecules of the new phase, called a nucleus, within the parent phase. For example, in water, small nuclei, the ice phase, form in the liquid phase as the temperature approaches 0 °C from above. To understand the transformation, classical nucleation theory $(CNT)^{65,66,67,68}$ considers the free energy G of the system, treating the nucleus as a bulk core surrounded by an interface. When nucleation takes place, the change in Gibbs free energy, shown in Eq. 5.1, is the sum of a bulk term (first term) and a surface term (second term);

$$\Delta G = -n \cdot \phi + \sigma \cdot A \tag{5.1}$$

where n is associated with the number of atoms in a cluster, ϕ (= $\Delta G/\Delta n$) is the affinity of the transformation associated with the change of chemical potential, σ is the surface energy and A is the surface area. Figure 5.1 shows a plot of free energy change ΔG vs nucleus radius r, where r^* is the radius of the critical nucleus. In the first regime ($r < r^*$), the nucleus formation from the free atoms or molecules is not thermodynamically stable, so the small nuclei in the parent phase appear and decay continuously. Once some nuclei exceed the critical nucleus size, the growth of nuclei leads to a decrease in ΔG . After the radii of nuclei are larger than r_0 , $\Delta G < 0$; that is, the phase transition now is energetically favorable, i.e., a spontaneous process.

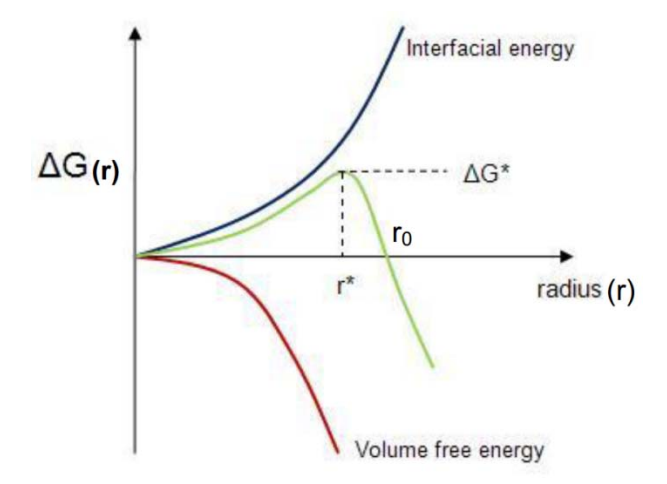


Figure 5.1 Change of free energy (ΔG) vs. radius of nucleus according to CNT, where r^* is the radius of the critical nucleus. The first order phase transition becomes energetically favorable when the nucleus radius is beyond r_0 .⁶⁹

Since the creation of a nucleus implies the formation of an interface at the boundary of a new phase in a uniform substance, homogeneous nucleation may be difficult. However, heterogeneous nucleation, which is considered as a surface catalyzed process starting at preferential sites such as surfaces or impurities, is more common. In terms of free energy change, the free energy barrier is lowered more than that of homogeneous nucleation owing to wetting, shown in Eq. 5.2.

$$\Delta G_{hetero} = \Delta G_{homo} \cdot f(\theta)$$
 5.2

where $f(\theta) = 2 - 3\cos\theta + \cos^3\theta/4$, and θ is the contact angle of the nucleus with respect to the core surface for the case of a liquid. Heterogeneous nucleation is essential for heteroepitaxial thin film growth as described in Chapter 5.3.

5.2 Crystal growth modes

If there is no interdiffusion between the substrate and the deposited material, thin film epitaxial growth is classified into three modes, according to the morphology of the first few monolayers: island, layer by layer, and layer plus island growth.⁷⁰ The modes are shown in Figure 5.2.

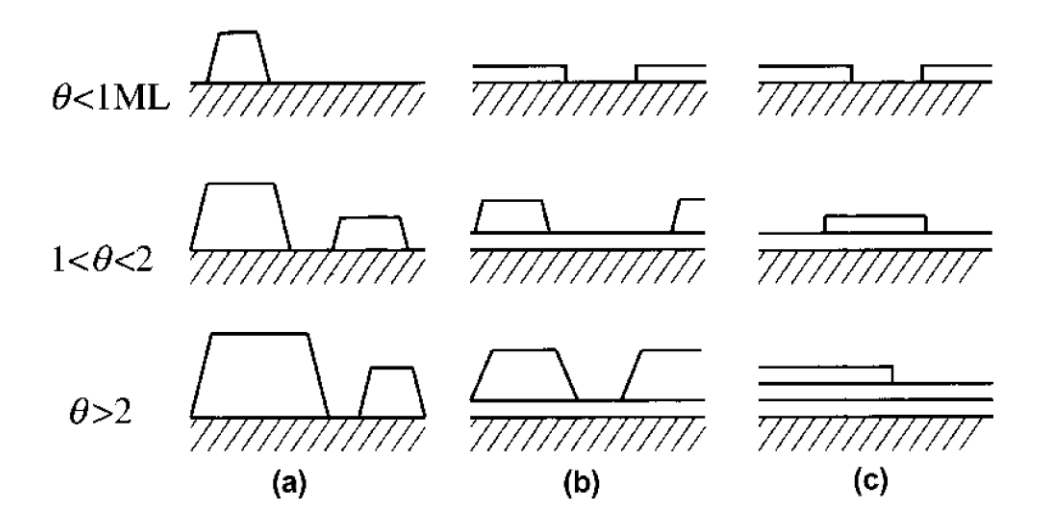


Figure 5.2 Illustrations of three thin film epitaxial growth modes as a function of surface coverage θ in terms of monolayers (ML): (a) island growth, or Volmer-Weber mode, (b) layer-plusisland growth or Stranski-Krastanov mode, and (c) layer-by-layer growth or Frank-van der Merwe mode.⁷⁰

In island growth, also known as Volmer-Weber (VW) mode, adatom cohesive force is higher than surface adhesive force. Hence, the growing material prefers to form islands on the substrate surface which then coalesce in a lateral direction. In terms of surface energy, this mode can be expressed as $\gamma_d + \gamma^* > \gamma_s$, where γ_d , γ_s and γ^* are the surface energies of deposited layer, substrate, and interface, respectively. On the other hand, when the adatom cohesive force

is lower than the surface adhesive force, the material tends to wet the substrate surface completely with the first few monolayers. This is the Frank-van der Merwe (FM) mode or layer-by-layer growth, where the relation of surface energies is $\gamma_d + \gamma^* < \gamma_s$. The layer plus island growth, or Stranski-Krastanov (SK) mode, is a combination of VM and FM modes. The growth of first few monolayers proceeds by the FM mode until it reaches a critical thickness, which depends on the strain and the chemical potential in the film. Then, the VW mode becomes energetically favorable. The initial expression of surface energies, therefore, starts as $\gamma_d + \gamma^* < \gamma_s$, and eventually turns into $\gamma_d + \gamma^* > \gamma_s$ (VW mode) as γ^* increases with the deposition thickness due to the stress.

5.3 Heteroepitaxial diamond growth

5.3.1 Epitaxy

Epitaxy is the process of single crystal layers depositing on a single crystal substrate of which one crystal plane serves as a template for the crystal structure of the deposit. This can be described in terms of Miller indices of the crystal planes and directions. For example, $(001)_d < 001 >_d || (001)_s < 001 >_s$ means that a (001) plane of the deposit resides on a (001) plane of the substrate where the < 001 > direction of deposited crystal is parallel to the < 001 > substrate direction. In many cases, the coincident growth planes are identical and of low index, such as (001) and (111) for cubic systems and (0001) for the hexagonal system. For cubic systems, twinning in particular may easily occur on (111) planes due to the geometric symmetry, reducing the crystal perfection in epitaxial films. As a consequence, (100) epitaxy is preferred for many materials including diamond.

When the deposited layer and the substrate are the same material, this process is specifically called *homoepitaxy*. In contrast, *heteroepitaxy* describes the process where the deposited layer and substrate are different materials. Because of the different lattice constants of epitaxial layer and substrate in heteroepitaxy, the lattice mismatch f is an important parameter for choosing suitable substrates. It is defined by $f = (a_d - a_s)/a_s$, where a_d and a_s are the lattice constants for deposited layer and substrate, respectively. If the crystal structures of deposited material and substrate differ, the mismatch is calculated from the atomic spacing of the contacting planes of deposited layer and substrate, instead of lattice constants. Lattice mismatch is one of the most important criteria for choosing a suitable substrate in heteroepitaxial growth.

Although homoepitaxy is prevalent in single crystal diamond growth, the lateral areas of CVD crystals have been limited by small, high-cost HPHT diamond substrates. Recently, a method of making tiled clones was developed to enlarge diamond crystal areas.⁷¹ The alternative to homoepitaxy is diamond heteroepitaxy, which represents another approach for overcoming the substrate size limitation by depositing diamond on wafer-size non-diamond substrates. A number of substrates have been used to achieve relatively large-area and high quality diamond growth. Substrate criteria for heteroepitaxial diamond growth will be discussed in Chapter 5.3.3.

5.3.2 Definition of diamond heteroepitaxy

To make a distinction from the sparsely faceted diamond grains that may appear on nondiamond substrates, we adopt the following criteria as a working definition of diamond heteroepitaxy:

(1) Area of a single-facet continuous diamond film to be at least 1 mm²;

- (2) Crystal structure and the epitaxial alignment of diamond with the substrate confirmed by x-ray diffraction with XRD linewidths less than 1°; and
- (3) sp³ bonding confirmed by polarized Raman scattering, resulting in a single frequency peak at 1332.4 ± 10 cm⁻¹.

This definition distinguishes a heteroepitaxial film from highly-oriented diamond (HOD), usually produced by deposition on Si wafers. HOD occurs by coalescence of µm-sized grains followed by a process of selective growth, in which certain grain orientations overgrow others. The best HOD films have an XRD mosaic spread generally greater than 1°.

5.3.3 Substrate criteria for diamond heteroepitaxy

Due to the stringent conditions for heteroepitaxial growth, the choice of a suitable substrate is an important consideration. The important factors for substrate selection are listed below:

- (1) Crystal structure. Since the single crystal substrate serves as a template for the deposited layer in heteroepitaxy, a crystal structure similar to the deposited material is advantageous, but not absolutely necessary. Substrates with cubic structure, such as Si and cubic oxides, have been commonly used
- (2) Lattice parameter. A small lattice mismatch *f*, typically less than 10%, is desired. The lattice mismatch induces strains at the interface which can be accommodated by the formation of misfit dislocations. A larger lattice mismatch gives rise to greater strain at the interface and a higher density of misfit dislocations. The misfit dislocations at the interface can evolve into different kinds of dislocations. A discussion of dislocation types will be presented in Chapter 6.1. Because of the short C-C sp³ bond in diamond, all substrates have larger lattice constants than diamond.

- (3) Surface energy. To form a flat and continuous film in epitaxial growth, the FM growth mode is preferred, which requires similar surface energies of deposited layer and substrate. A large difference in surface energy inhibits nucleus formation. For a moderate difference of surface energy, the VW mode, with a higher density of coalescence boundaries, is energetically favorable. This opens opportunities for dislocation generation at coalescence boundaries. Diamond has a rather high surface energy, 5.3 J/m² for the (111) plane and 9.2 J/m² for the (100) plane.³⁸ For comparison, Si has surface energy 1.23 J/m² for the (111) plane and 2.13 J/m² for the (100) plane.⁷² Consequently, creating uniform diamond nucleation on a non-diamond substrate is a challenge for diamond heteroepitaxy.
- (4) Thermal expansion coefficient α. For CVD diamond growth, the growth temperature is well above room temperature. Cooling from the growth temperature to room temperature results in stress arising from the differential thermal contraction between film and substrate. The large thermally-induced stress can lead to fracture of epitaxial film and substrate. To minimize this thermal stress, a substrate with thermal expansion coefficient matching the deposited material is advantageous. This is non-trivial, owing to the small thermal expansivity of diamond. The thermal expansion coefficients of popular substrates are shown in Table 5.1.

Table 5.1 Thermal expansion coefficients of some substrates used in diamond heteroepitaxy (at 300 K). ^{73,74,75,76,77,78}

Material	Diamond	Silicon	Iridium	SrTiO ₃	MgO	Sapphire
$\alpha (10^{-6}/\mathrm{K})$	1	2.56	6.4	9.4	10.4	5.3

- (5) Physical and chemical stability. A substrate should have a melting point much greater than diamond growth temperatures (700-1200°C) with a single, stable structure. High stress fracture strength is an advantage. For diamond heteroepitaxy the substrate should have low carbon solubility to avoid the formation of carbide phases which may impede epitaxial alignment^{79,80}. The substrate can, however, make a substantial chemical bond with carbon.
- (6) Substrate area and finish. Areas greater than 1 mm² with smooth, epi-polished surfaces are advisable. In some cases, one or more thin epitaxial buffer layers can be used to make a transition between the bulk substrate and the heteroepitaxial material.

Due to the unique properties of diamond and the aggressive CVD growth environment, no ideal non-diamond substrate exists. It is useful to divide diamond heteroepitaxy into two categories: (1) deposition onto a bulk single crystal substrate and (2) deposition onto a substrate with one or more epitaxial buffer layers. The latter is more complicated due to the requirement of multiple epitaxial processes. As a practical matter, large-area and high-quality diamond heteroepitaxy has only been realized on substrates with an epitaxial Ir buffer layer.

5.3.3.1 Heteroepitaxial diamond growth on bulk substrates

Silicon substrates were initially used for diamond growth and diamond (001) heteroepitaxy was attempted early. However, true heteroepitaxial diamond on Si was not observed. Rather, highly oriented (HOD) material was obtained, as mentioned in Chapter 5.3.2. Due to the small lattice constant of diamond, 0.357 nm, the lattice mismatch between silicon and diamond is 52%. It was suggested that diamond nucleation on silicon substrates involved a β-SiC transfer layer, with lattice mismatch of 22%. ^{81,82,83} By carefully controlling the growth conditions, others observed the direct deposition of diamond on Si. ^{83,84,85} Despite many attempts, an XRD linewidth less than 1° was never observed.

The properties of cubic boron nitride (c-BN) are similar to diamond. It has a similar crystal structure, 1.3% lattice mismatch, and similar surface energy, 4.8 J/m² for the (111) plane. Single crystal c-BN is itself difficult to produce, so (111) oriented particles embedded in a tantalum disk or a platinum plate have been tried as a substrate for diamond (111) heteroepitaxy. Although deposition of a well-coalesced diamond epitaxial film was observed, the lack of c-BN substrates makes its use for diamond heteroepitaxy impractical. 88

The use of metal substrates with small lattice mismatch to diamond such as nickel and platinum has been studied. Ni, with misfit 1.3%, is known as an effective solvent-catalyst metal for HPHT diamond crystallization.⁸⁹ However, its high carbon solubility and strong catalytic activity lead to the appearance of a graphite interlayer which forms immediately in a CVD environment, destroying diamond orientation. The formation of a nickel carbide interlayer forms under some growth conditions, leading to textured diamond deposition. Certain processing

methods led to orientation improvement, but only HOD was observed with its orientation derived from the carbide layer, not the metal surface.^{79,80}

Pt, with lattice misfit of 11% to diamond, is not expected to form a carbide. Small diamond crystals have been reported on Pt at an early stage of growth leading to HOD deposition on the Pt (111) surface.⁹⁰

5.3.3.2 Heteroepitaxial diamond growth on Ir

Since the first demonstration of diamond (001) epitaxial growth on its (001) surface⁴, iridium has emerged as the best buffer layer for diamond heteroepitaxy. The crystal structure of Ir is FCC with a lattice constant of 0.384 nm, resulting in a 7% lattice mismatch to diamond. Iridium has a very high melting point, 2450 °C, no crystal phase transitions or carbide formation, and the lowest carbon solubility (by weight) in the platinum group.⁹¹

In the first use of Ir for heteroepitaxy, Ohtsuka *et al.*^{4,5} sputtered a 500 nm Ir (001) epitaxial layer on $10\times10~\text{mm}^2$ (001) MgO substrates at 750 °C. Prior to diamond growth, the Ir surface was treated by bias enhanced nucleation (BEN). As a result, highly-oriented pyramidal diamond crystals were formed on the BEN exposed area which coalesced to a film of thickness 1.5 μ m. This result stimulated a great deal of subsequent research on diamond heteroepitaxy.

To ensure the reproducibility of surface preparation and to enlarge the substrate area, commercial epi-polished strontium titanate (STO) was used for Ir deposition, principally by two groups. ^{6,7,8,9} The lattice constant of STO is 0.391 nm, with lattice mismatch to Ir of 1.8%. The Ir layer was deposited by electron beam (e-beam) evaporation at temperatures above 800 °C. The XRD rocking curve linewidth of Ir (002) was 0.17°. ⁶ XRD pole figures showed an epitaxial

relation $(001)_{Ir}[100]_{Ir} \parallel (001)_{STO}[001]_{STO}$. STO substrates are reduced at high temperatures and blacken; they have low mechanical fracture strength. Sapphire, Al_2O_3 , henceforth ALO, on the other hand, has good chemical stability at high temperatures and is available in large-area wafers with excellent crystallographic quality. Electron-beam evaporated Ir on a-plane sapphire (a-ALO) was studied by Dai *et al.*^{8,10} Although ALO is hexagonal, its atomic spacing along [0001] direction is a good match to the Ir lattice in the $[01\overline{1}]$ direction, with lattice mismatch 1.1%. The epitaxial relation is $(001)_{Ir} \parallel (11\overline{2}0)_{ALO}$ with $[011]_{Ir} \parallel [1\overline{1}00]_{ALO}$ and $[011]_{Ir} \parallel [0001]_{ALO}$. The Ir (002) rocking curve width was comparable with Ir/STO, 0.21°. In this dissertation, we have used Ir/a-ALO as the substrate of choice for diamond heteroepitaxy.

Ir, with additional buffer layers on silicon, has been explored as another alternative for diamond heteroepitaxy, principally because of the low thermal expansivity of silicon. For example, a calcium fluoride (CaF_2) interlayer was deposited on a silicon substrate followed by an epitaxial Ir layer^{92,93}, but CaF_2 was not a practical choice due to its high thermal expansion coefficient and low thermal stability. Later CaF_2 was replaced with an yttria-stabilized zirconia (YSZ) buffer layer and the crystallographic relationship $(001)[110]_{Ir} \parallel (001)[001]_{YSZ} \parallel (001)[110]_{Si}$ reported.¹¹

5.4 Enhancement of diamond nucleation

Due to high surface energy, diamond nucleates sparsely on a non-diamond substrate, with nucleation density 10^3 - 10^5 cm⁻², mostly at defects.⁵² A surface pretreatment prior to diamond deposition is always necessary to enhance nucleation density. Scratching⁹⁴, seeding⁹⁴, electrical biasing⁹⁵, covering⁹⁶, coating⁹⁷, ion implantation⁹⁸, pulsed laser irradiation⁹⁹ and carburization¹⁰⁰ are methods used to realize nucleation enhancement. Various enhancement mechanisms

proposed were: (1) seeding effect; (2) minimization of surface energy on sharp convex surfaces; (3) breaking of surface bonds or dangling bonds at edges; (4) strain; (5) carbon saturation at edges; (6) surface cleaning by removal of oxides; and (7) formation of non-volatile graphitic clusters. Initially, the first two methods were the most efficient in nucleating diamond on silicon with nucleation density limited to 10^6 - 10^8 cm⁻². An improvement, known as bias enhanced nucleation (BEN)⁹⁵, increased nucleation densities up to 10^{10} cm⁻².

5.4.1 Bias enhanced nucleation (BEN)

Substrate pretreatment by BEN is a process of ion bombardment. It is implemented on a substrate surface held at a negative potential in a hydrogen/methane plasma. The accelerating electric field and presence of methane lead to the bombardment of the substrate with positively charged hydrocarbon radicals. The diamond nucleation density was found to increase with the bias current density, the ion flux on the substrate surface. The major variables in BEN are the substrate temperature, methane concentration, bias voltage, and the bias duration. The first few BEN experiments were performed on a Si substrate biased at –60 to -100V in 15 Torr hydrogen plasma with 2 to 40% CH₄ with a substrate temperature of 850 to 900 °C. After 5 min growth in 0.5% CH₄, polycrystalline diamond growth was observed. 95,103,104

5.4.1.1 Proposed mechanism of BEN

For BEN on Si, the ion bombardment leads to: (1) ion subplantation, (2) deposition of an amorphous carbon layer, (3) surface diffusion, and (4) formation of a SiC interlayer. Figure 5.3 shows a proposed BEN mechanism appropriate to Si. Hydrocarbon radicals are formed in the plasma above the substrate surface which then impinge on the substrate surface and diffuse to stable sites 105,106,107 resulting in the deposition of an amorphous carbon layer. The energetic

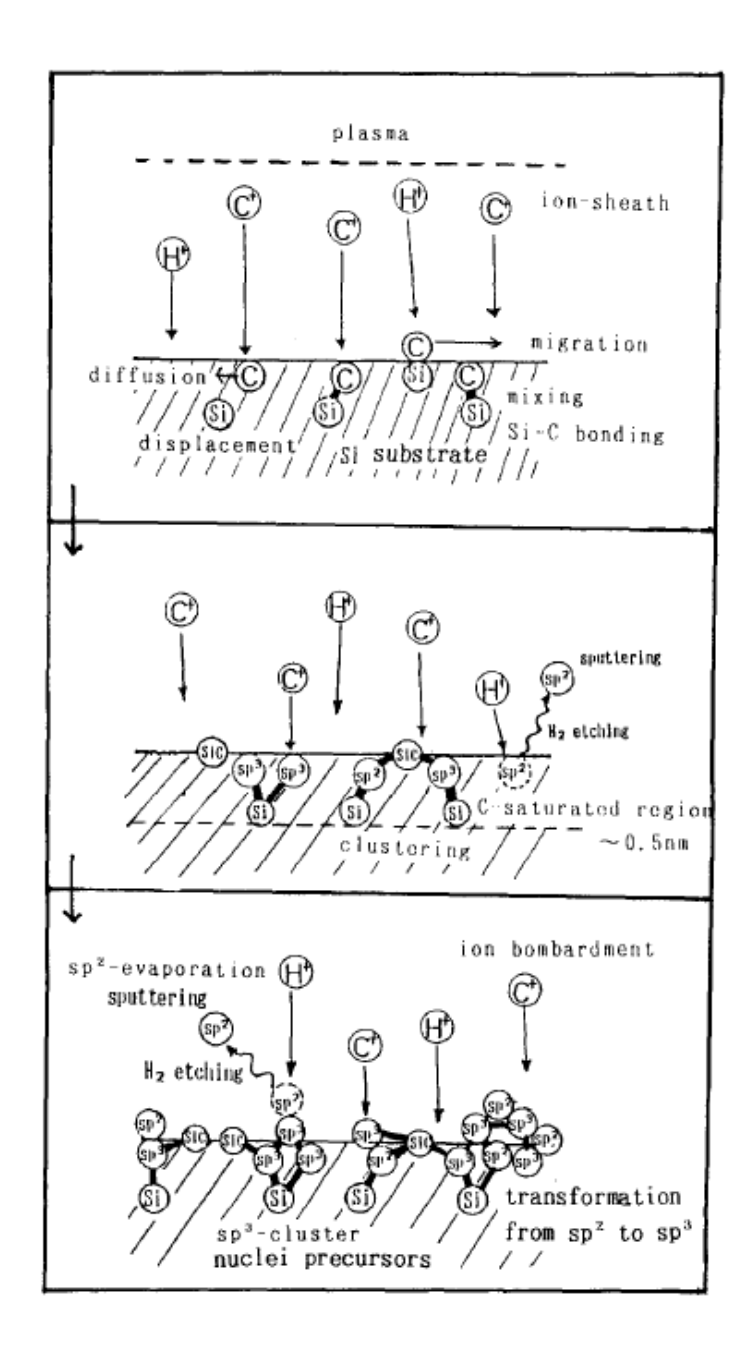


Figure 5.3 Illustration of BEN mechanism. 103

bombardment also roughens the substrate surface. The hyperthermal (1-10³ eV) hydrocarbon species are implanted^{110,111,112} just below the substrate surface, a process called subplantation. Owing to preferential etching of sp² bonds by energetic atomic hydrogen, sp² graphitic surface carbon is eliminated or transformed to sp³-rich clusters.¹¹³ Hydrogen-terminated surfaces prevent

the formation of further sp² bonds. The remaining sp³-rich clusters are believed to be the precursors of diamond nuclei. Excessive methane concentration leads to the formation of sp²-rich structures while excessive acceleration of ions destroys sp³ structures. As a consequence, obtaining optimal nucleation density requires striking a balance between methane concentration and bias voltage.

BEN on Si does not fully explain the BEN process on Ir. The bias conditions for Ir and its surface modification are significantly different from Si. The most important distinction is that no diamond nuclei or diamond growth have been observed on Ir immediately after BEN. The mechanism of BEN on Ir is, in fact, not fully understood. We discuss experimental results for Ir BEN and the ensuing diamond growth in Chapter 5.4.1.3.

5.4.1.2 Bias and plasma chemistry

A typical optical emission spectrum of a CH_4 - H_2 plasma is shown in Figure 5.4 which reveals the main active species are atomic hydrogen, with emission wavelengths for H_{α} (656 nm) and H_{β} (486 nm), and many hydrocarbon signals. The simple hydrocarbons can be classified into two categories by their bonding types: C_1 (431nm) containing σ bonds, such as CH_3 , CH_2 and CH_3 , and CH_4 and CH_5 (516 nm), composed of π bonds, such as CH_5 , CH_6 and CH_7 and CH_8 are concentration of each active species near the substrate is a function of hydrogen plasma pressure and methane concentration. At moderate pressure, 10^0 to 10^2 Torr, the concentration of atomic hydrogen, and CH_6 emissions, increases with pressure. The CH_6 CH_6 ratio, representative of the plasma electron temperature, however, decreases with pressure due to reduction of the mean free path of gases. On the other hand, the concentration of atomic hydrogen decreases with increasing methane concentration CH_6 CH_6 resulting in a slower etching rate of sp² carbon. Therefore, a low methane concentration was initially used for high quality CVD diamond epitaxy.

In BEN, owing to the acceleration of electrons in the plasma sheath, the degree of ionization near the substrate surface increases, giving rise to the ignition of a bright DC glow discharge above the substrate surface, the secondary plasma. 116,117,118,119 The DC glow indicates a change of plasma chemistry and the concentrations of active species near the substrate surface. It was discovered that highly oriented diamond nucleation on Si requires a glow discharge that covers the entire substrate surface. Figure 5.6 shows that all concentrations of active species increase with bias and eventually saturate at a high voltage. The ratios of $H_{\rm B}$ / $H_{\rm a}$ and C_2 /CH behave similarly as well. 116,120,121 It was found that diamond crystal quality could be correlated with the emission intensities of CH and C_2 . Diamond grown under conditions with a strong CH signal had good crystal quality whereas poorer diamond formed under conditions giving a maximized

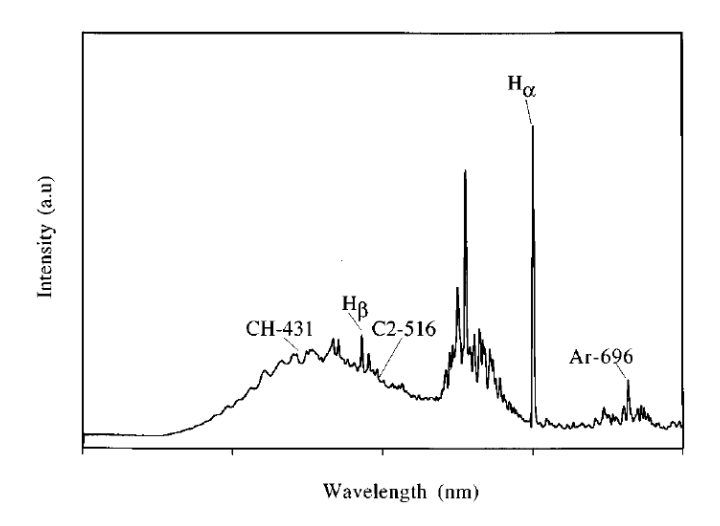


Figure 5.4 Optical emission spectrum of a CH_4 - H_2 plasma at 30 Torr and 2% CH_4 . Ar was used as an actinometer to estimate the concentration of atomic hydrogen. The wavelengths of emission lines of C_1 and C_2 type species are indicated. 114

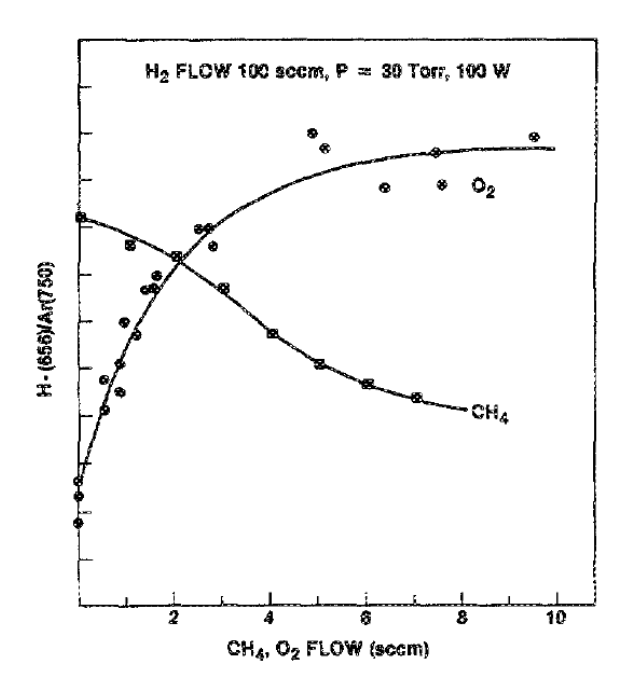


Figure 5.5 Intensity of H_{α} emission vs. methane and oxygen flow rates, representing the relationships between atomic hydrogen, methane, and oxygen concentrations. The methane concentration is 9% with a hydrogen flow rate of 100 sccm and methane flow rate of 10 sccm.¹¹⁵

 C_2 signal. ¹²² Despite preferential formation of sp² bonds at high C_2 content, the increased atomic hydrogen concentration near the substrate surface etched sp² bonds more rapidly. ¹²¹ Thus, there is a competition between the deposition of a sp³-rich layer and substrate surface etching. ¹²⁰ On the other hand, as methane concentration increases during BEN, the electron temperature increases and the C_2 /CH ratio decreases. Then, saturation of H_B / H_α and C_2 /CH occur at higher voltage or higher pressure. Plasma chemistry also varies with vertical position above the substrate during BEN. From the plasma edge to the substrate surface, the concentration of atomic hydrogen decreases and becomes constant. In contrast, the electron temperature and the ratio of C_2 /CH increase and saturate as the substrate is approached. ¹¹⁴

In summary, BEN modifies the production of C_2 components and atomic hydrogen near a substrate surface. In addition, the high electron temperature further enhances C_2 formation. As a result, the carbon-saturated clusters with both sp^2 and sp^3 bonds easily form at the stable sites on substrate surface. Then, by preferential etching by atomic hydrogen, the weak sp^2 bonds will be removed. The remaining stable sp^3 -rich carbon clusters are the precursors for the formation of diamond nuclei.

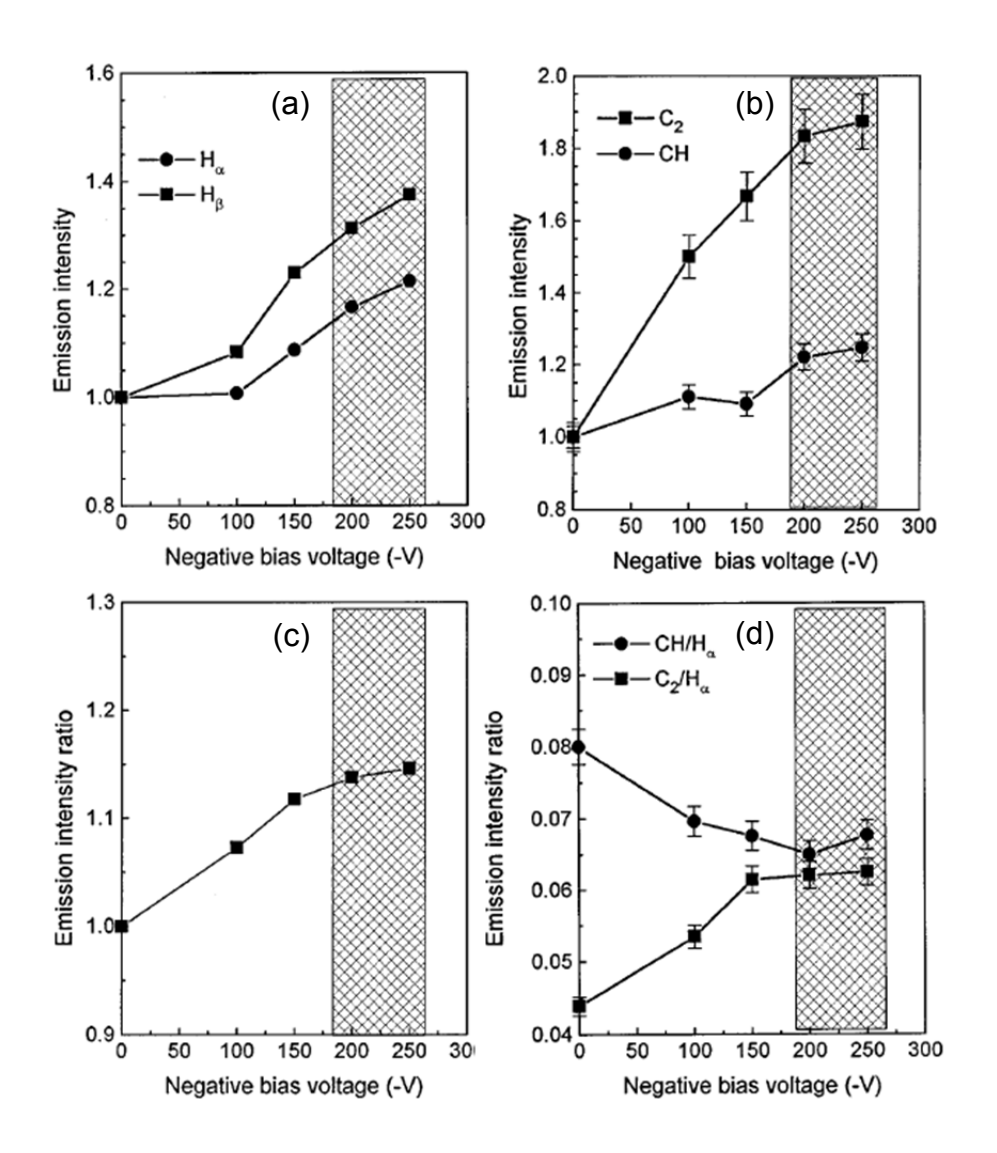


Figure 5.6 Concentrations of (a) atomic hydrogen (b) two types of hydrocarbons (c) H_B/H_α and (d) ratios of C_2/H and CH/H_α vs. bias voltage at 15 Torr and 2% CH_4 . ¹²¹

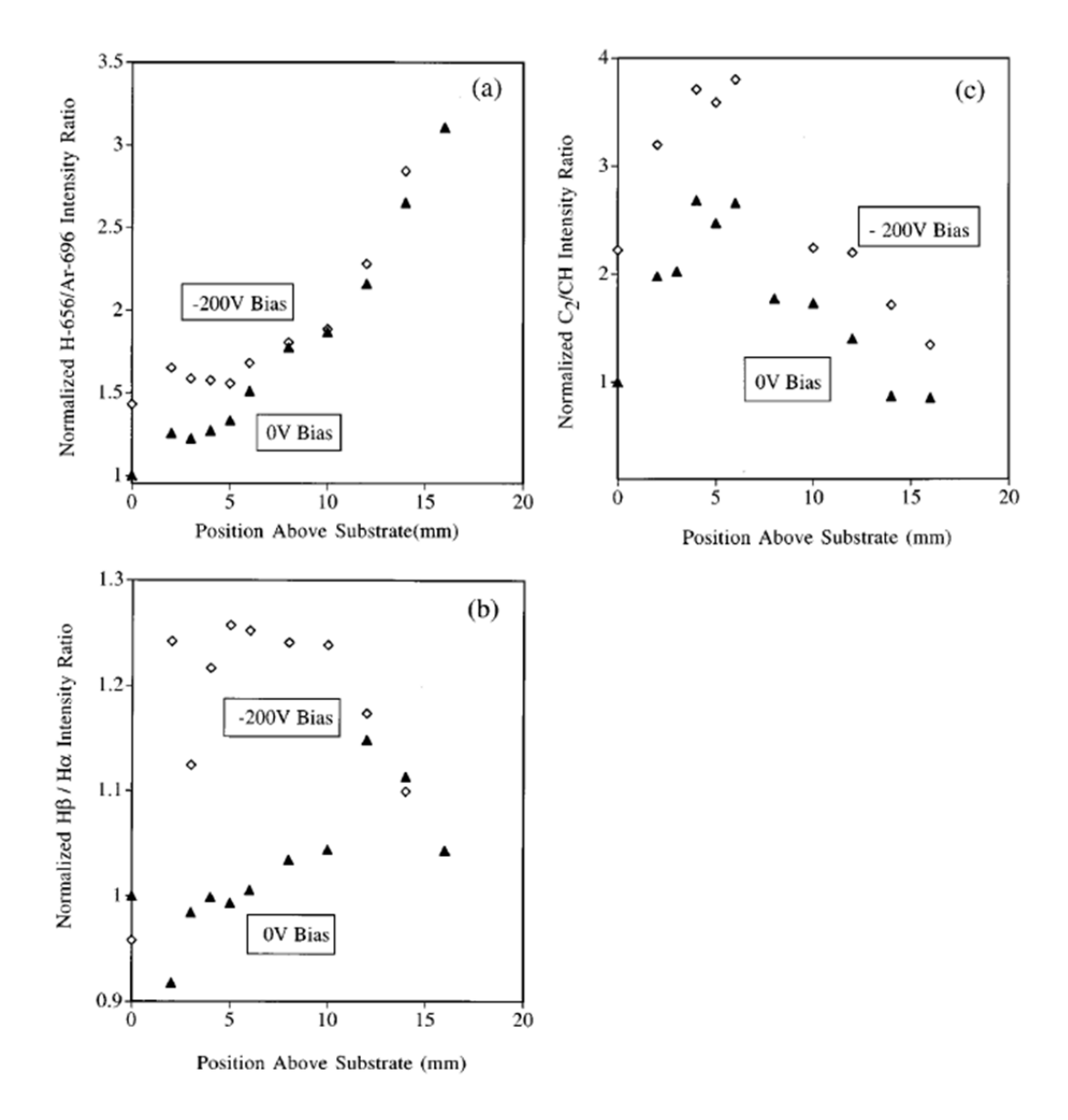


Figure 5.7 Concentrations of (a) atomic hydrogen (b) H_B/H_α and (c) ratios of C_2/CH vs. position relative to substrate surface in vertical direction, where the solid triangles and hollow rhombohedra represent the data points without and with bias voltage under conditions of 30 Torr and 2% CH_4 .¹¹⁴

5.4.1.3 Bias enhanced nucleation on iridium

BEN on Ir is typically carried out with a negative bias of 150 to 350 V applied to the substrate, and 2-5% methane in hydrogen. The duration of BEN depends on the bias voltage and the methane concentration. Bias times more than 30 min are often used to achieve nucleation densities on diamond of order 10¹¹ cm⁻².

BEN on Ir leads to Ir surface modification and deposition of a thin amorphous carbon layer. 9,31,123,124,125,126,127 It was discovered that the Ir surface was etched into furrows during BEN 126 and that the orientation of the furrows changes from $<110>_{Ir}$ to $<100>_{Ir}$ with increasing

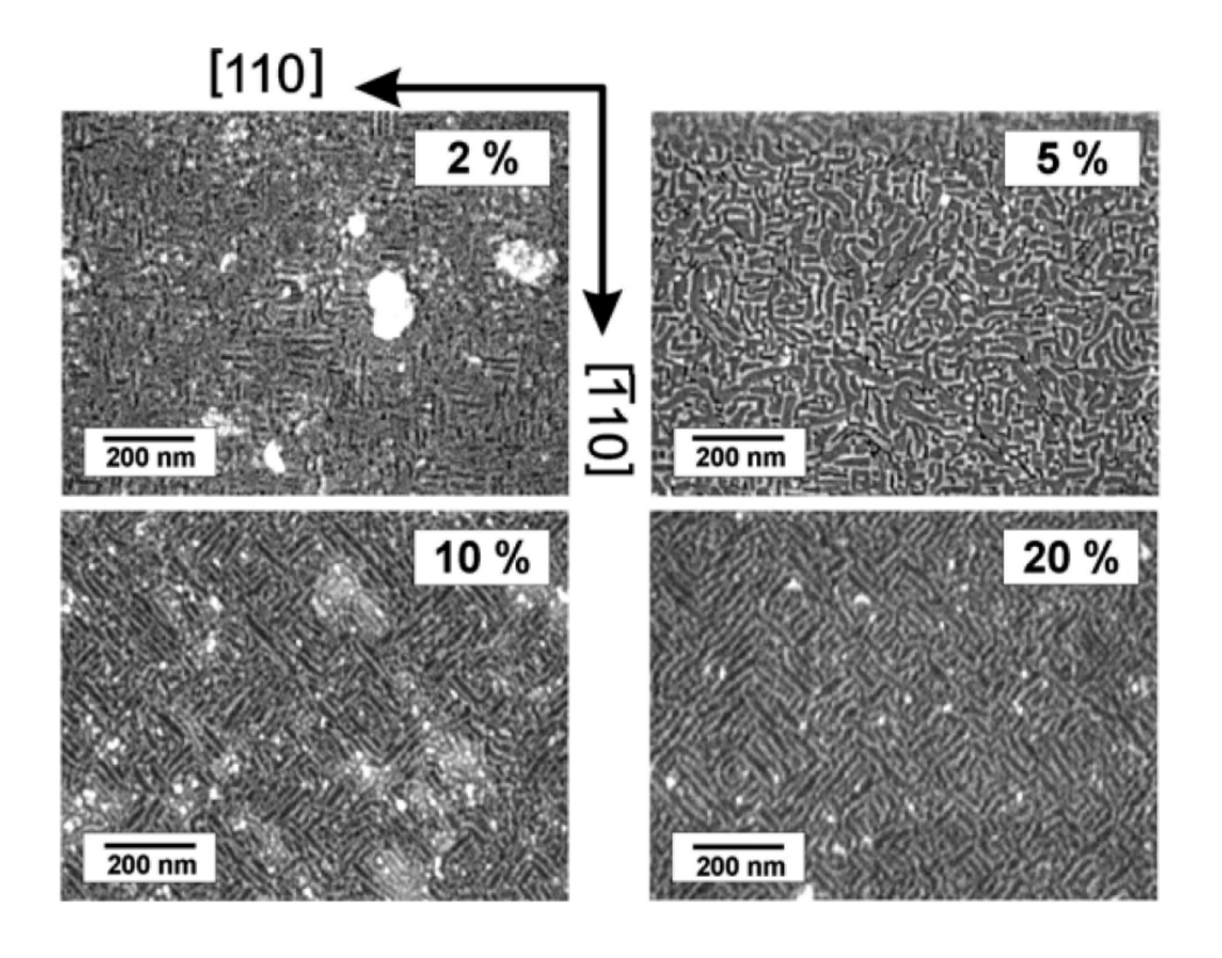


Figure 5.8 Plan-view SEM images of BEN-treated Ir surfaces with increasing methane content. 127

methane content¹²⁷, Figure 5.8. The Ir furrows were partly covered by a layer which appears bright in SEM images, Figure 5.9. The bright areas occur in clusters named "domains". ¹²⁸

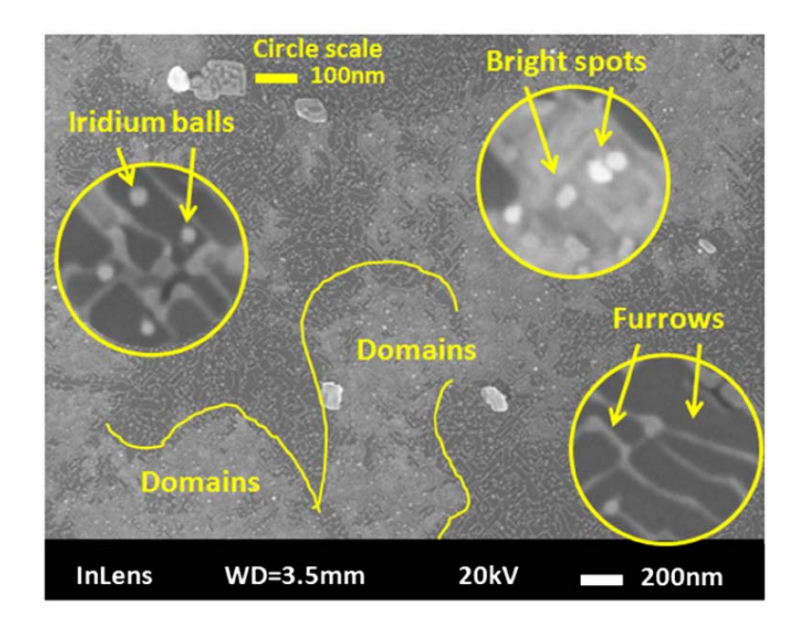


Figure 5.9 Plan-view SEM image of BEN-treated Ir surface showing Ir furrows, Ir balls, bright spots and the domains, where the scale of the images inside the circles is 100 nm. ¹²⁹

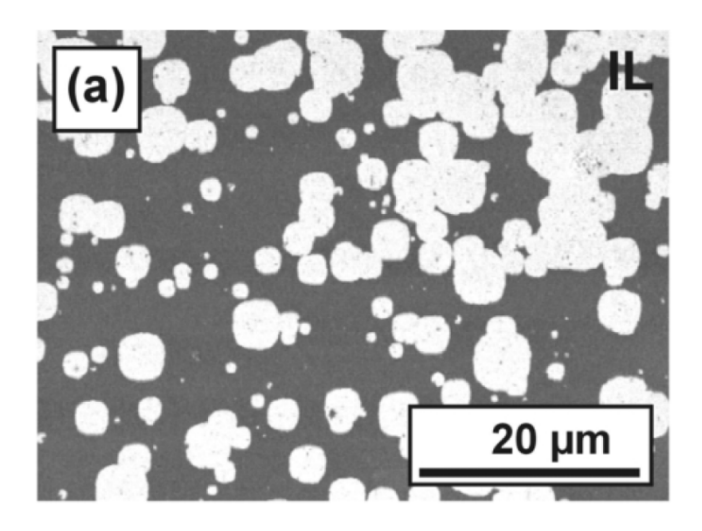


Figure 5.10 Low-resolution SEM image of BEN-treated Ir surface showing the bright areas referred to as domains. ¹²⁸

The Auger spectrum of the bright layer is similar to amorphous carbon. ¹²⁹ According to x-ray photoelectron spectroscopy (XPS) measurements, this layer contains partially disordered sp² carbon, C-H bonds formed in hydrogen-rich plasma and sp³ bonding in an amorphous tetrahedral carbon structure, like diamond. ^{130,131,132} The depths of Ir furrows were reported as 2-3 nm^{126,129} and dependent on bias conditions. Conflicting reports of domains heights were given: in one account, domains were 8.4 nm higher than its vicinity¹²⁹; others ¹³³ found that domains resided in 1 nm depressions.

Domains were confirmed to be the precursor region for diamond growth ^{128,129,132,134} as shown in Figure 5.11. Domain coverage increases with bias duration to a point: ^{128,129} however, 100% coverage by domains has not been achieved. The mechanism of domain expansion during bias has not been explained.

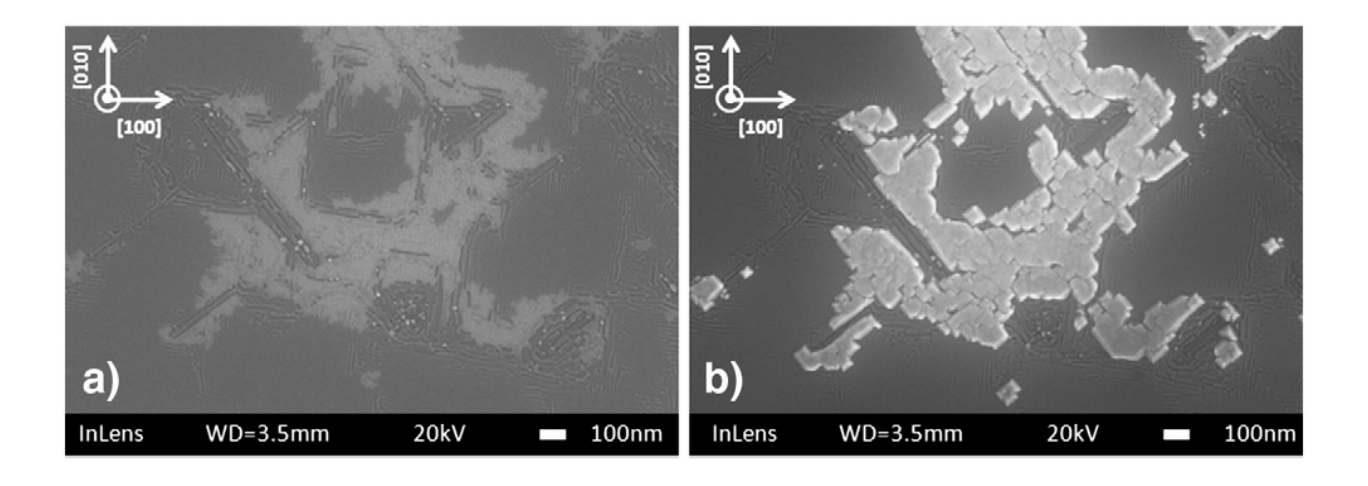


Figure 5.11 Plan-view SEM images of (a) domain formation on Ir after 30 min BEN and (b) 15 min diamond growth in the domain.¹²⁹

Qualitatively different Ir surface modification after BEN has been extensively studied. These studies^{8,9,31} used a low bias voltage, -150 V, and low methane concentration, 2%. For

short-term bias, 20 min, furrows along <110> and dots were observed. The biased Ir surface was also highly covered by the carbon layer, showing bright SEM regions covering 75% of the surface. Unlike the irregular domains, the carbon patches in Figure 5.12 are rectangular with edges along <110>.

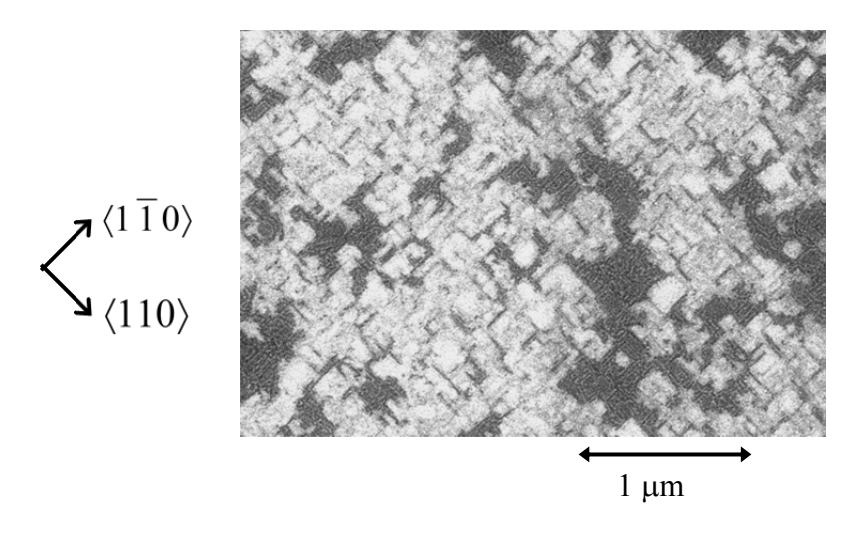


Figure 5.12 Plan-view SEM image of Ir surface after 20 min bias.⁹

After 60 min bias, Ir dots forming a nearly hexagonal array were observed with a density 10^{11} - 10^{12} cm⁻², Figure 15.13(a). The lateral size of an Ir dot is 5 nm with a mean dot to dot spacing of 15 nm. The coverage of the carbon layer was about 90%. The corresponding high-resolution transmission electron microscopy (HRTEM) cross-sectional image, Figure 5.13(b), shows faceted Ir pillars with a mean spacing 14.6 ± 0.5 nm covered by a bright amorphous carbon layer. In these images, the mean lateral size and height of Ir pillar is 8 and 4.5 nm, respectively.

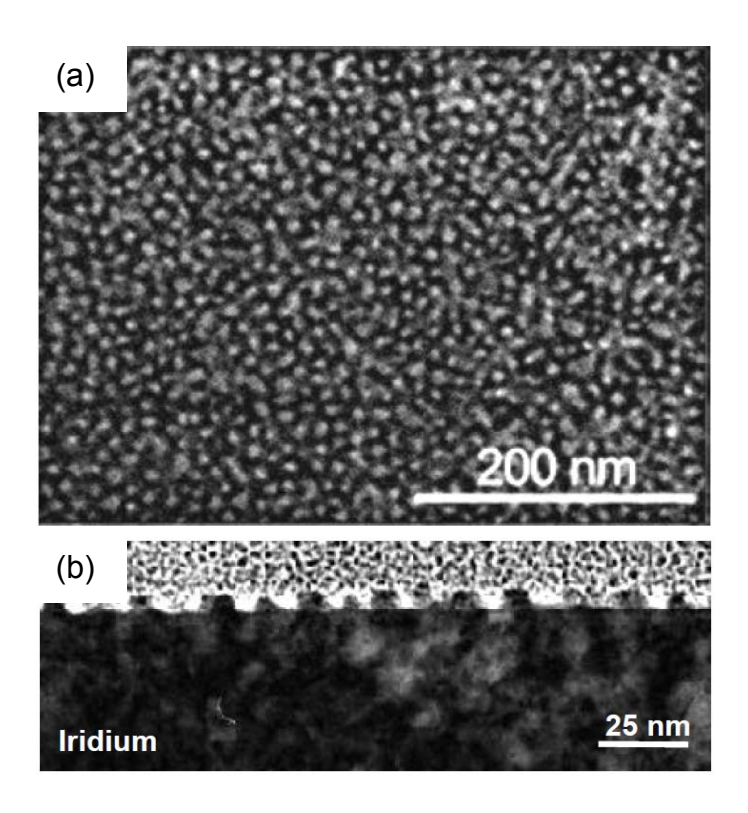


Figure 5.13 (a) Plan-view SEM image and (b) HRTEM cross-sectional image of BEN treated Ir surface after 60 min.³¹

Unlike diamond growth on Si, no Ir-C interfacial layer and no crystalline diamond crystallites on Ir immediately after bias were observed with HRTEM. 123,124,135 A diamond signature was, however, clearly seen by x-ray photoelectron diffraction analysis. 135,136 This suggests that the size of diamond nuclei must be very small, possibly sub-nanometer. Short interrupted growth experiments, following biasing, showed very early stage emergence of diamond. After 90s of growth, diamond was observable but crystal facets had not fully developed, Figure 5.14(a). The HRTEM image in Figure 5.14(b) clearly shows the diamond crystallites emerging from the Ir interface, indicating that the diamond nucleated on the sides of the Ir nanopillars.

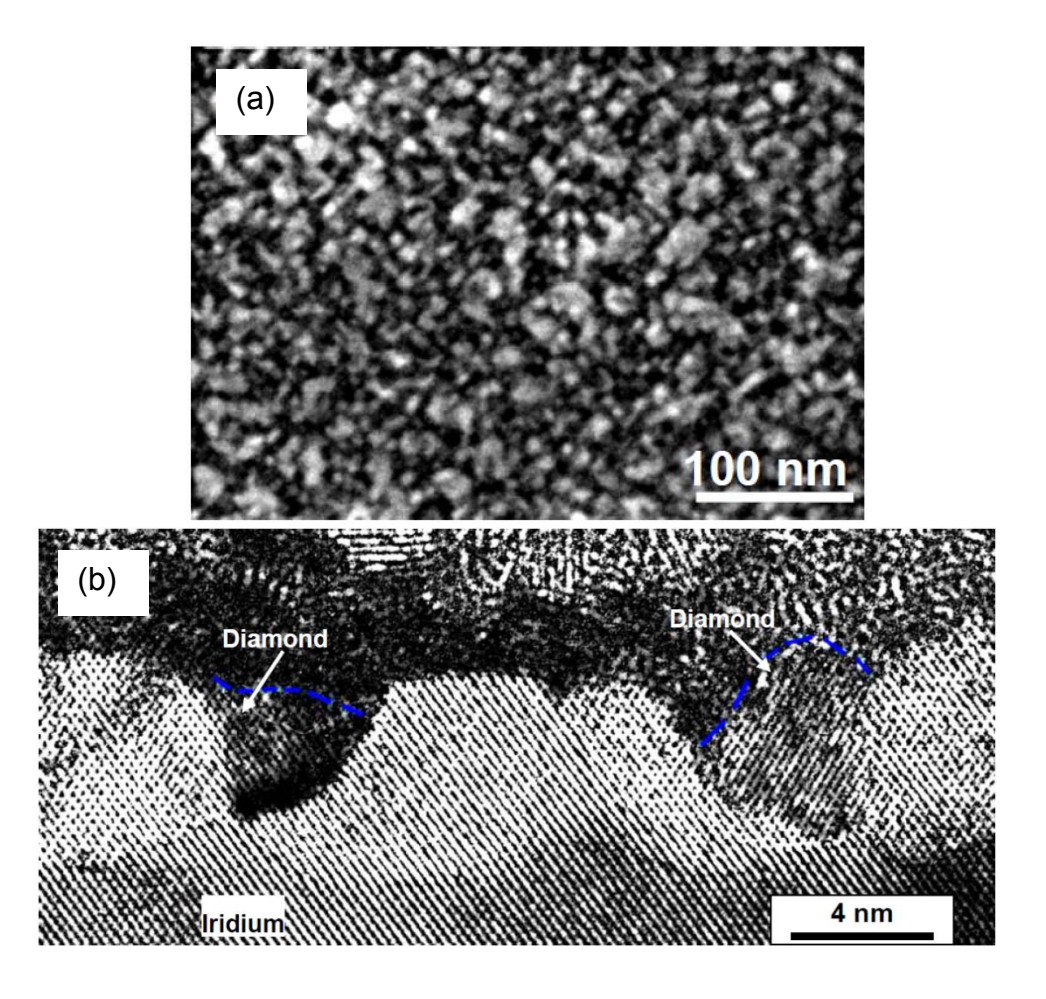


Figure 5.14 (a) Plan-view SEM image and (b) HRTEM cross-sectional image of 90s diamond growth on a 60-min biased Ir surface. In (b) each white line is the (111) plane of Ir (bottom) and diamond (surrounded by blue dashed line) crystals.³¹

As a result of high coverage of carbon following biasing, coalescence of individual grains began soon after growth commenced, leading to the formation of a partially connected film with a flat top surface, as shown in Figure 5.15 after 10 min growth. Figure 5.16 shows a comparison of diamond surfaces of two groups after short growth periods. In the present work, after 1h growth, diamond thin films were well-coalesced, forming a flat and continuous film, with few visible boundaries. Other groups, as shown in Figure 5.16(c, d), found cubic or rectangular

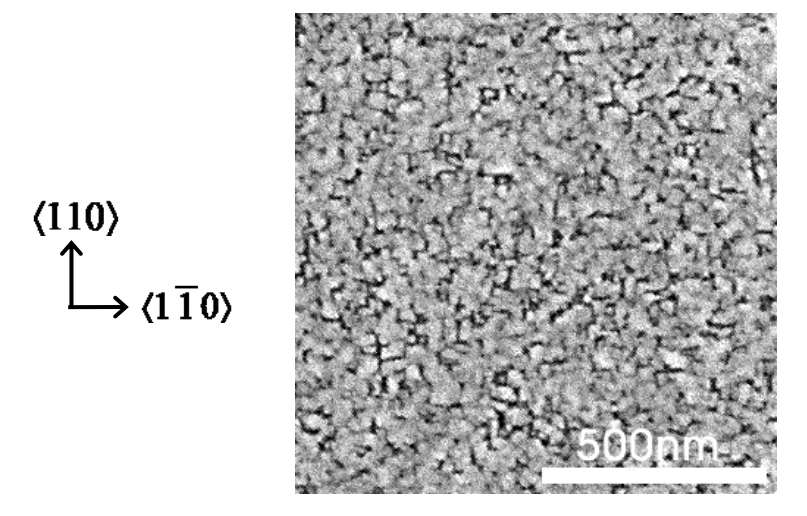


Figure 5.15 Plan-view SEM image of diamond surface after 10 min growth following 60 min biasing.

diamond crystallites with (001) top surfaces. Given similar growth conditions, listed in Table 5.2, the coalescence rate will mainly depend on carbon surface coverage and the resulting diamond nucleation density. Higher diamond nucleation density leads to an earlier continuous thin film. Table 5.3 lists the bias conditions used by different groups for comparison.

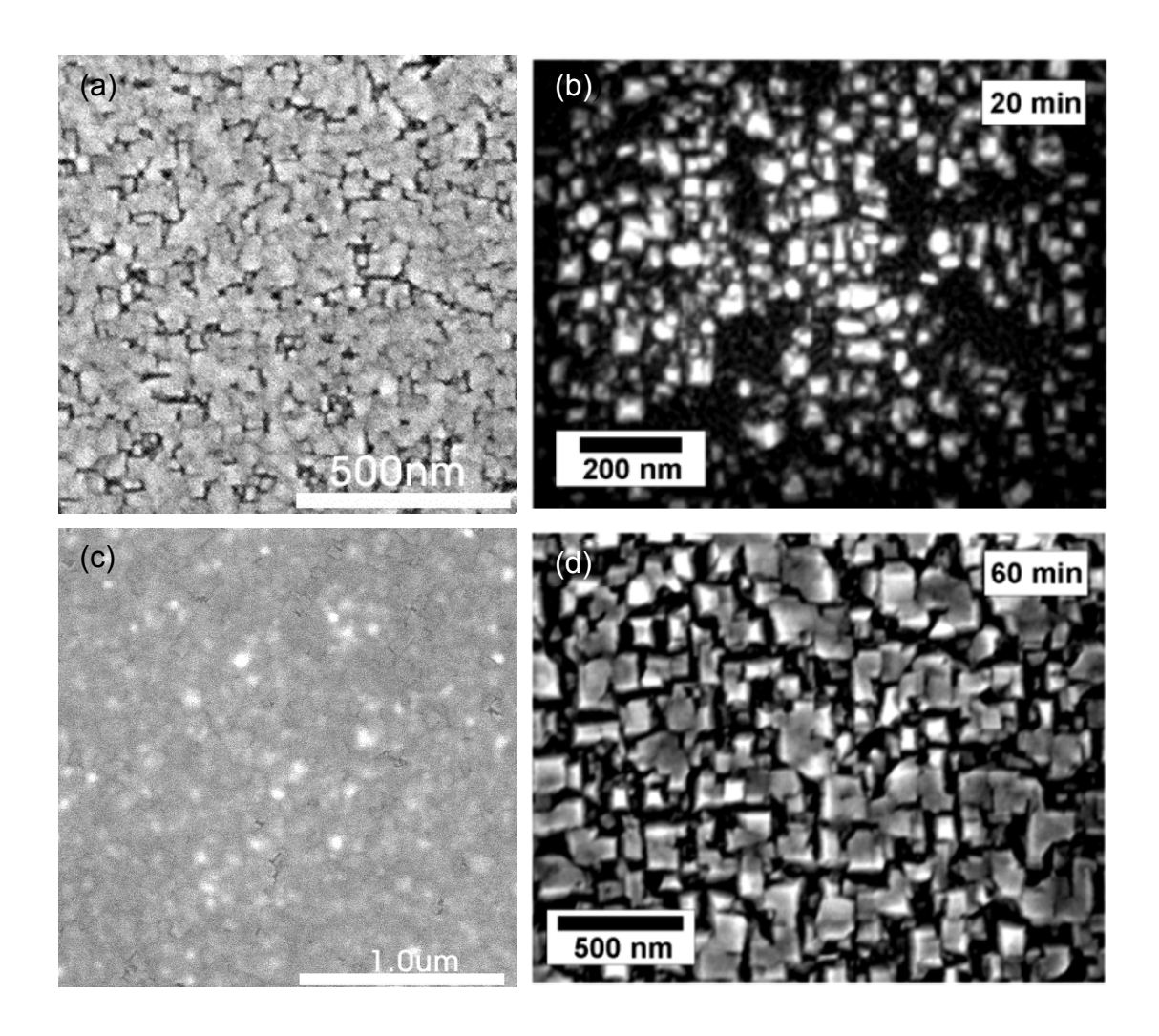


Figure 5.16 Heteroepitaxial diamond surface after 20 min growth $(a)^{47}$ and $(b)^{127}$. Diamond surface after 60 min growth $(c)^{47}$ and $(d)^{127}$.

Table 5.2 Comparison of growth conditions for samples shown in Figure 5.16.

	Pressure (Torr)	CH ₄ (%)	N ₂ (ppm)	Substrate temperature (°C)	Reactor type
Bauer et al. 127	22.5	1	30-50	650	MPCVD
Golding et al. 47	18	1		670	MPCVD

 Table 5.3 Bias conditions for groups studying diamond heteroepitaxy on Ir.

	Pressure (Torr)	CH ₄ (%)	Bias voltage (-V)	Substrate temperature (°C)	Duration (min)	Reactor type
Bauer et al. 127	22.5	0.5-10	250-320	700	45	MPCVD
Chavanne et al. 132	15	4	300	700±50	60	MPCVD
Washiyama <i>et al.</i> ¹³	115	2		940	90	DC CVD
Stehl et al. 137		3	300	850		MPCVD
Golding et al. 8,9,47,31,	18	2	150	710	60	MPCVD

6. Chapter 6 Epitaxial lateral overgrowth (ELO)

6.1 Dislocations

A real crystal contains imperfections due to impurities and other defects. The latter can be categorized into four groups according to their dimensionality: vacancies or self-interstitial atoms are point defects (0-D), dislocation lines are linear defects (1-D), grain boundaries and stacking faults are planar defects (2-D) and voids and precipitates are considered as volume defects (3-D). Dislocations are the most important issue in epitaxial growth. Crystalline quality is usually compromised by dislocation propagation into the growing layer from the interface. Especially for heteroepitaxy, the dislocation density typically is 10¹⁰ cm⁻², due to the lattice mismatch and the different chemical properties of the substrate and deposited material. Moreover, although some interfacial dislocations are generated to release stress, a high density of propagating dislocations usually leads to a high intrinsic stress state, which can cause film cracking.

Dislocations are classified into two types: edge and screw. They can be visualized as follows. Consider an extra half-plane of atoms (ABCD) inserted into a perfect crystal, Figure 6.1(b). The adjacent atoms then are displaced to each side by one lattice spacing. The line DC, thus, is a positive edge dislocation, noted as \bot . If the half plane is inserted into the lower part of crystal, the line DC is a negative edge dislocation, \top . If the ABCD half-plane is inserted in the same place but with neighboring atoms displaced to one side of the half plane relative to the other side, the AB direction, the line DC is a screw dislocation. The helicity of such a dislocation can be identified by drawing a circle around the dislocation line DC, looking along DC. If the helix

advances one plane, it is a right-handed screw dislocation, as shown in Figure 6.1(d). Most of the dislocations in crystals are of mixed type with the coexistence of edge and screw displacements.

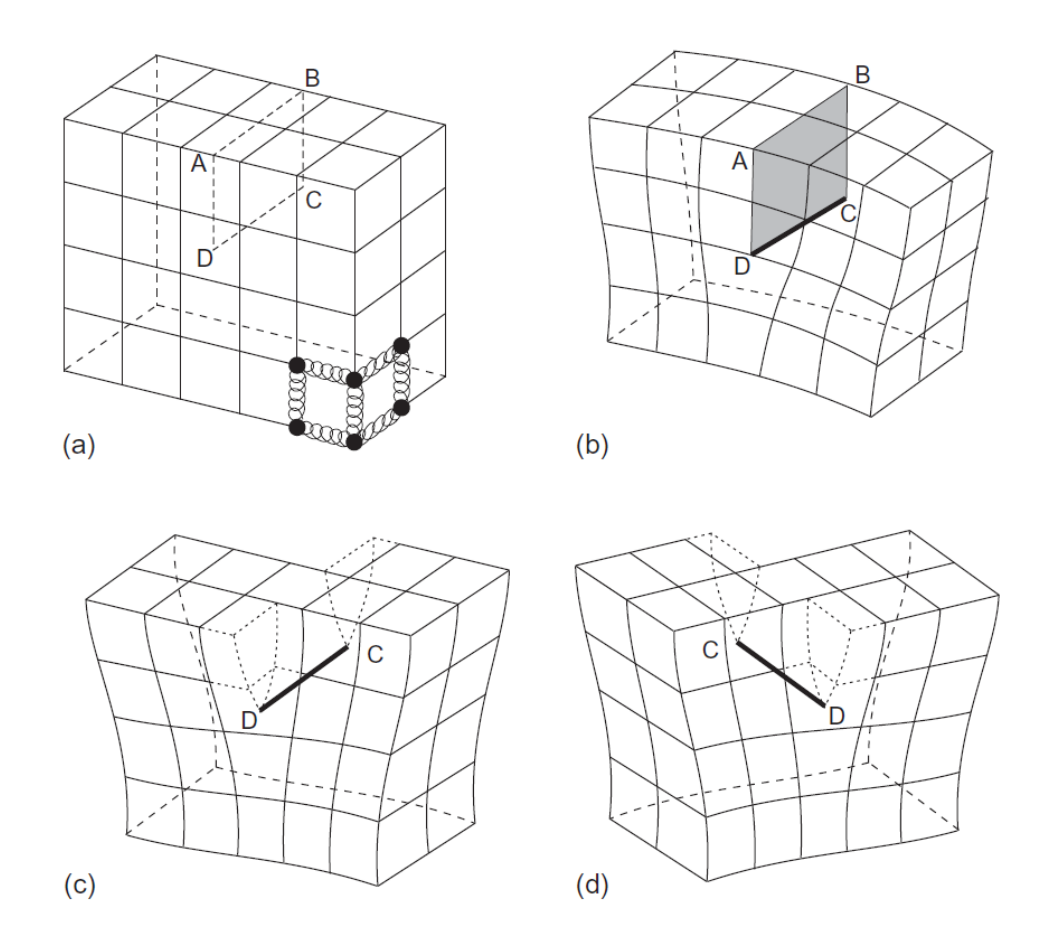


Figure 6.1 Illustration of dislocation geometry: (a) a perfect single cubic lattice as reference; distorted crystal lattices with a dislocation line DC which is a positive edge type in (b); a left-handed screw type in (c); and a right-handed screw type in (d). ¹³⁸

In a heteroepitaxial system, with lattice mismatch between growth material and substrate, coherent growth only survives in the first few layers of deposition due to the enormous stress in the film. As the thickness reaches a critical thickness, edge dislocations, called misfit dislocations, form at the interface to release the stress. The critical thickness depends on elastic strength and is typically 2-3 nm. Because of the rigid diamond lattice, misfit dislocations form

directly at the diamond-substrate interface, Figure 6.2. Because dislocations can move along glide planes, they may propagate upward into the epitaxial layer, forming threading dislocations. A positive dislocation can be annihilated only by interacting with its negative counterpart, or may terminate in a closed loop.

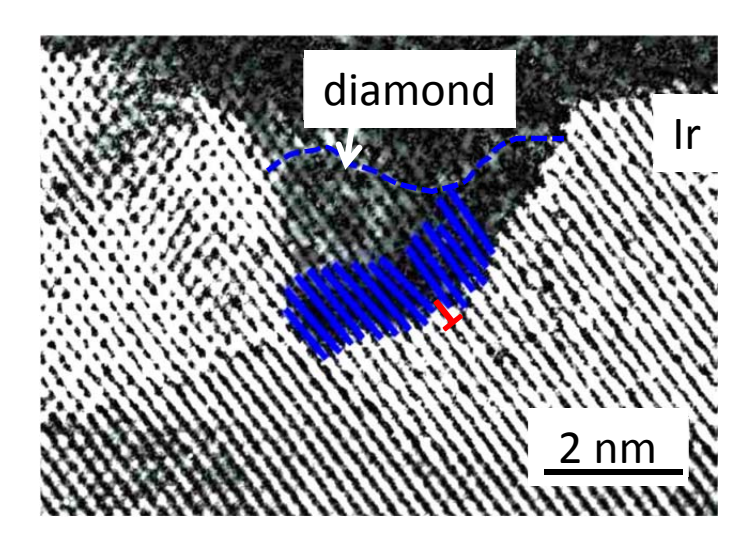


Figure 6.2 HRTEM image at the interface between diamond and Ir. The circled area by the blue dashed line is the diamond grain. The blue and white lines represent the diamond (111) and Ir (111) lattice planes, respectively. A misfit dislocation formed at the interface, indicated by \bot .³¹

6.2 ELO method

In the ELO process, a substrate patterned by a mask layer is used. The epitaxial layer, then, grows vertically from the seed area and laterally over the mask layer. This selective area growth was invented in the 1960's for GaAs homoepitaxy in small areas. ^{139,140,141} It was discovered in 1988 that dislocations were blocked in ELO in GaAs homoepitaxy. ¹⁴² This resulted in a nearly dislocation-free lateral overgrown GaAs layer. Since then, various ELO methods have been widely studied for III-V semiconductors, principally GaAs and GaN. In 1997, Usui *et al.* ¹⁴³ developed an ELO process for GaN heteroepitaxy and reduced the dislocation density by three orders of magnitude. Figure 6.3 shows the concept of ELO for blocking threading dislocations.

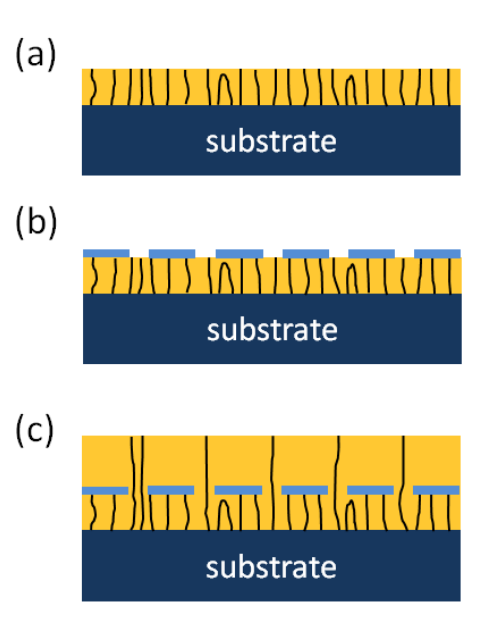


Figure 6.3 Illustration of an ELO process. (a) A thin epi layer serves as a substrate, where the solid lines generated from the substrate represent the threading dislocations. (b) A mask, e.g. SiO₂, is deposited and patterned by lithography. (c) Material overgrows the mask which blocks the threading dislocations during regrowth. The threading dislocation density is greatly reduced in the overgrown regions.

6.3 Types of ELO on GaN

6.3.1 Facet-initiated ELO (FIELO)

Usui *et al.*¹⁴³ developed the FIELO method for hydride vapor phase epitaxy method, shown in Figure 6.3. A thick GaN film, 26 μ m, was grown on a 2-in diameter sapphire substrate. The window stripes lie along <11 $\overline{2}$ 0> of the GaN layer with a period of 7 μ m and 1-4 μ m wide SiO₂ stripes serve as the mask. {1 $\overline{1}$ 01} facets formed on the side of the GaN stripes at the beginning of the growth, and the facets gradually coalesced above the SiO₂ mask. This method lowered the dislocation density by 3 orders of magnitude compared to the conventional GaN layer.

6.3.2 Different masking materials

 SiO_2 was first used as a mask for a GaN ELO process. However, the threading dislocations, especially around the mask, propagated laterally into the overgrown GaN, and merged at the center of the mask which was the coalescence region. In the center of the mask, the c-axis directions of 2 adjacent GaN lattice planes were found to tilt toward the boundary by 2° , but they tilted $\sim 1^{\circ}$ away from boundary at the edges of the mask. Kawaguchi *et al.* chose tungsten as the masking material. They studied the growth rates of different axes for $<11\overline{2}0>$ and $<1\overline{1}00>$ GaN stripes.

Sone *et al.*, later, discovered the ELO GaN layer did not contact the W layer. Instead, a triangular void formed above the mask.¹⁴⁷ Besides, the rocking curve widths of (0004) planes were ϕ -independent for ELO GaN with a W mask and were smaller than the corresponding widths of ELO GaN with a SiO₂ mask, where ϕ is the azimuthal angle between the stripe and rotation axis in an ω -scan. The c-axis tilting contributed to broadening when the stripes were

aligned parallel to the rotation axis with a SiO_2 mask. It was inferred that the large interfacial tension between the SiO_2 layer and GaN caused c-axis tilting. Transmission electron diffraction supported the argument that the void between the W mask and GaN prevented interfacial tension, suppressing c-axis tilting.¹⁴⁸

Tomiya *et al.* found that, with a SiO₂ mask, c-axis tilting could be suppressed in GaN ELO with plasma-enhanced CVD grown SiO₂ vs. e-beam evaporated SiO₂. In addition, they discovered less interfacial tension between ELO GaN using a SiN_x mask.¹⁴⁹

6.3.3 PENDEO epitaxy

Zheleva *et al.*¹⁵⁰ invented the method of PENDEO, a method without a contacting mask. As shown in Figure 6.4(b), the GaN/AlN/substrate was etched to form alternating columns and trenches along the $<1\overline{1}01>$ direction with widths of 3-5 μ m and 3-40 μ m, respectively. The free-standing laterally grown GaN layers coalesced above the trenches of the substrate with a large horizontal-to-vertical growth rate ratio, Figure 6.4(c). The resulting dislocation density was 4-5 orders of magnitude lower than in the GaN/AlN/substrate.

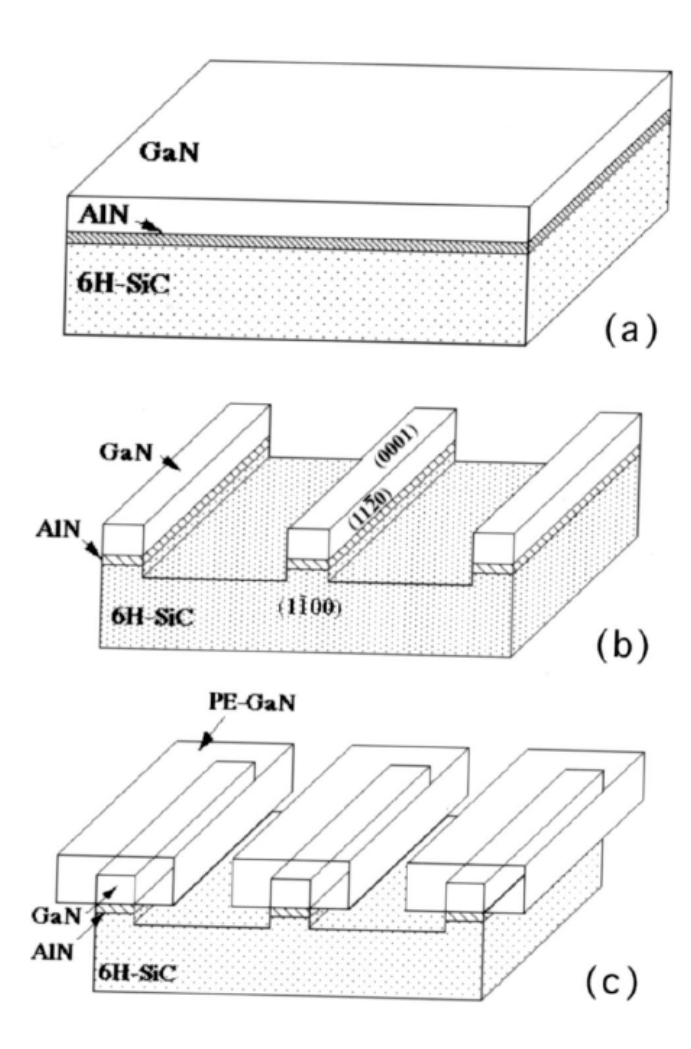


Figure 6.4 Illustration of PENDEO epitaxy. (a) A GaN epitaxial layer grown on a 6H-SiC substrate with AlN buffer layer serves as a substrate for the PENDEO process. (b) The GaN epilayer is plasma-etched to form alternating columns and trenches. (c) Regrowth of GaN columns has a large lateral-to-vertical growth rate ratio. 150

6.3.4 Air-bridged ELO

As shown in Figure 6.5, GaN was dry etched into a ridge-stripe pattern along $<1\overline{1}00>$. The bottoms of the trenches and the sidewalls of the GaN ridges were covered with a thin Si₃N₄ mask. In the initial stage, the GaN stripes grew vertically and then extended laterally over the mask from the newly formed $\{11\overline{2}0\}$ facets. A c-axis tilting was seen in a split XRD rocking curve, but the tilt angle was about an order of magnitude lower than that of ELO GaN with a SiO₂ mask.

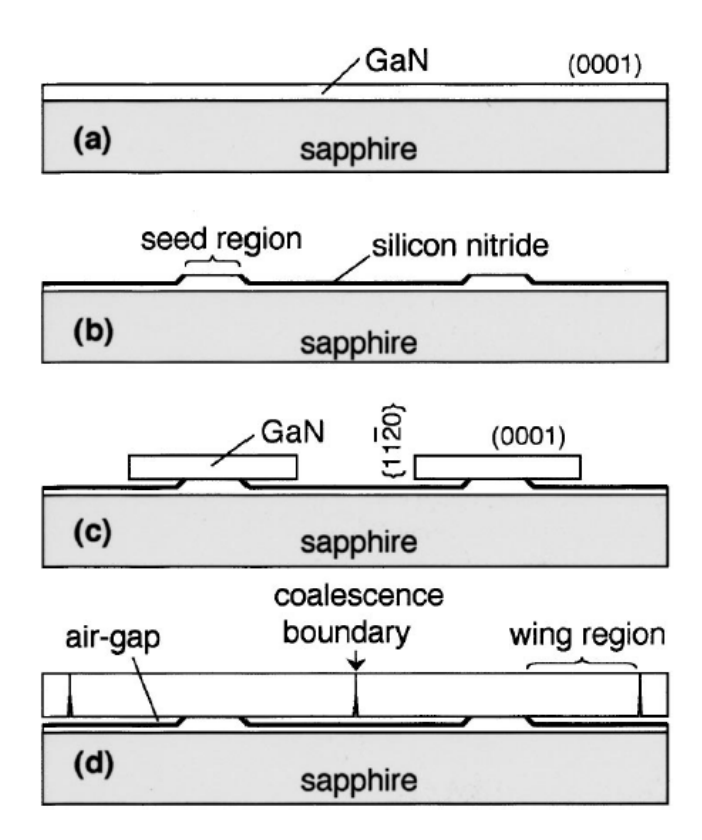


Figure 6.5 Illustration of air-bridged ELO: (a) a GaN/sapphire substrate; (b) GaN layer partly plasma etched to form ridges; (c) regrowth of GaN and (d) coalesced GaN overgrown layer in the center of masked region. In (b), except for the top surfaces of GaN ridges, other areas are covered by the Si_3N_4 mask.¹⁵¹

The reduced c-axis tilting was attributed to the air gap which removes the interfacial tension between the Si_3N_4 layer and ELO GaN.¹⁵¹

6.3.5 Cantilever epitaxy

To avoid impurity contamination from masking materials, i.e. SiO₂, and reduce the residual stress caused by thermal and lattice mismatch between GaN layer and substrate, Si (111), 6H-SiC (0001)_{Si}, and basal-plane sapphire substrates were fabricated via photolithography and reactive ion etching techniques to form a grooved structure prior to GaN growth ¹⁵², Figure 6.6(a). GaN was then deposited on the exposed substrate surfaces. Owing to the high lateral-to-vertical growth rate ratio, the GaN layers on two adjacent terraces shielded the trenches. Therefore, they coalesced laterally before the GaN overgrew the trenches. Flat GaN layers were achieved on the sapphire and 6H-SiC patterned substrates, but a very low lateral-to-vertical growth rate ratio was observed in GaN ELO on Si. The rocking curve linewidths of overgrown GaN on different substrates were comparable to those of GaN grown on the corresponding non-patterned substrates. The c-axis tilt was found to be in the direction perpendicular to the groove orientation. For sapphire and 6H-SiC substrates, dislocation densities in the GaN layer on the substrate terrace were three orders of magnitude lower than a typical GaN layer, and it was one order of magnitude further lower in the ELO GaN.

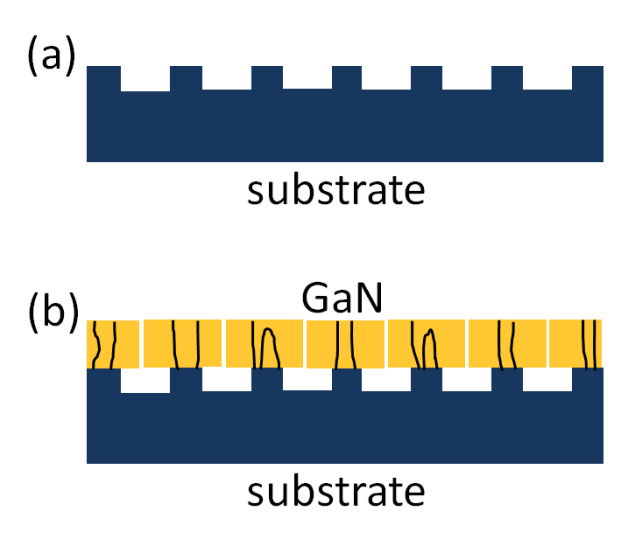


Figure 6.6 Illustration of cantilever epitaxy. (a) Substrates 6H-SiC, Si and Al₂O₃, are plasma etched to form trenches (etched area) and terrace (unetched). (b) GaN layers grow on substrate terraces.

6.3.6 Direct lateral epitaxy

A low nucleation density, 4×10^4 cm⁻², of GaN in the non-masked region was obtained by a low temperature buffer treatment on a patterned sapphire substrate with a SiO₂ mask.¹⁵³ With the high growth temperature and high pressure ratio of V/III content, the lateral-to-vertical growth rate ratio was increased to 2. The sparse GaN grains coalesced and formed a GaN stripe with a flat (0001) surface. The GaN layer further extended laterally over the mask region because of the high lateral growth rate. This method was called direct lateral epitaxy. In the overgrown region, the rms roughness of the GaN (0001) surface was as low as 0.3 nm indicating the absence of threading dislocations.

6.4 Types of ELO on diamond

Due to the aggressive chemical and thermal growth environment, ELO on heteroepitaxial diamond has not been widely explored. Ando *et al.* first demonstrated the ELO idea in heteroepitaxial diamond without a growth mask.¹² The (001)-oriented heteroepitaxial Ir was first deposited on a MgO substrate and treated by bias enhanced nucleation followed by e-beam lithography to pattern the surface. The patterned Ir surface was then ion beam etched by Ar to damage the non-masked region. Diamond (001) selectively grew from the prepared Ir layer, and overgrew the damaged Ir area. They established a minimum diamond nucleation density needed to grow specific areas.

Washiyama *et al.*¹³ further showed the results of coalesced diamond stripes along <100> and <110> directions. Owing to the facet-dependent growth rate, the spacing for <100> and <110> stripes were 20 and 10 µm, respectively. The Raman linewidth of overgrown diamond gradually decreased to a minimum at the coalescence boundary, indicating a lower defect density. Compared to the diamond nucleation region, with a Raman linewidth of 10-12 cm⁻¹, the linewidth of the overgrown diamond was reduced to 5 cm⁻¹. However, tensile strain was observed both in the overgrown and non-overgrown diamond.

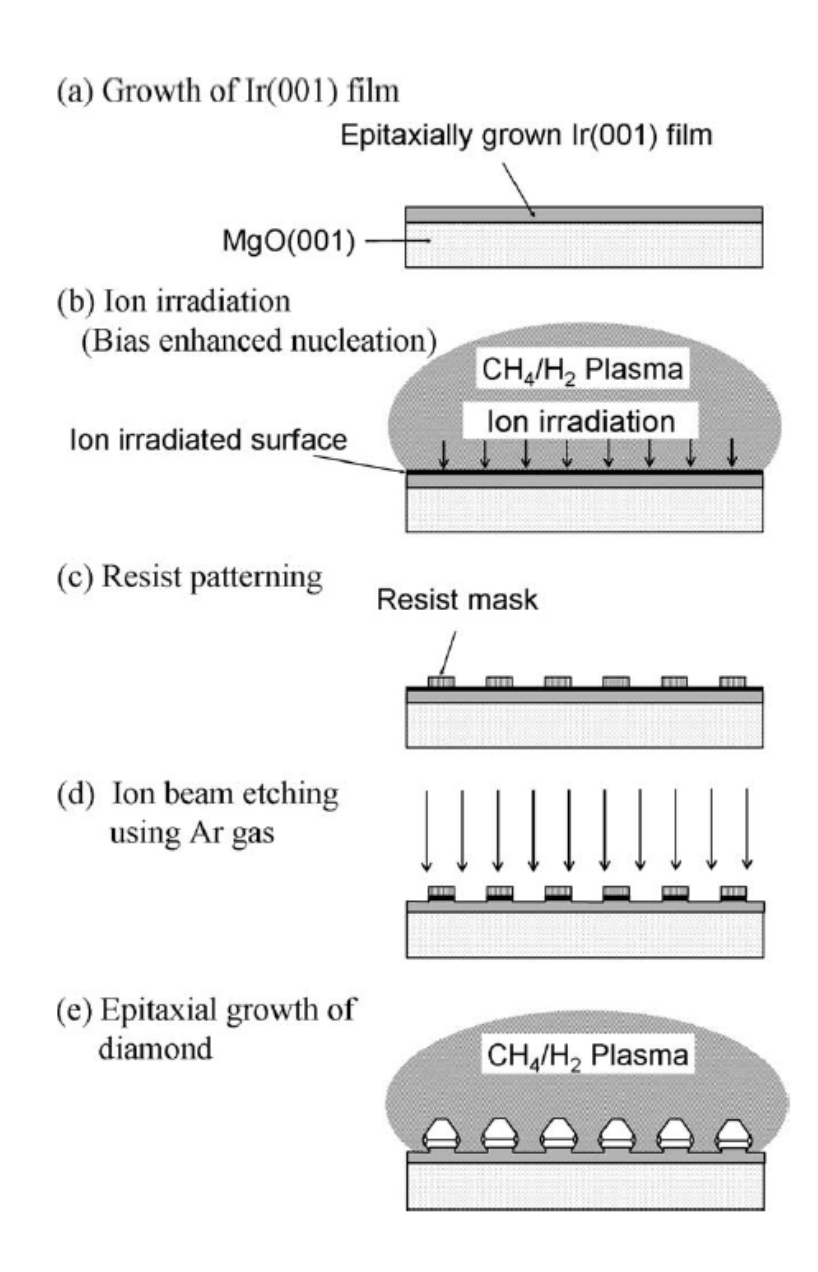


Figure 6.7 Steps of the diamond ELO process by Ando et al. and Washiyama et al. 12

Bauer *et al.*¹⁵⁴ deposited a very thin, 10-20 nm, Ir heteroepitaxial layer as a percolating mask layer on a (001)-oriented CVD diamond layer on a Si substrate and a (001)-oriented HPHT Ib diamond substrate. The porous Ir layer formed a mesh with 10-200 nm holes. For a 13 nm Ir layer, the coverage was about 70%. Diamond islands penetrated the Ir layer and coalesced into a (001) facet for the 2 types of substrates. However, overgrown diamond showed larger rocking

curve widths and Raman widths relative to those of non-overgrown diamond, indicating a high level of microstrain attributed to an increased dislocation density. Furthermore, a macroscopic tilt between the crystal lattice of Ib HPHT diamond substrate and overgrown CVD diamond layer in the off-axial direction was found.

7. Chapter 7 Epitaxial Ir growth on a-plane sapphire

This chapter describes the Ir DC sputtering process and the characterization of epitaxial Ir (001) growth on a-plane $(11\bar{2}0)$ sapphire (a-ALO). Owing to its cubic structure, its relatively small mismatch to diamond and its special chemical properties, the epitaxial Ir (001) buffer layer on various substrates serves as the best template for heteroepitaxial CVD diamond (001) growth, cf. Chapter 5.3.3.2. The crystallographic quality, as indicated by the mosaic spread of the Ir layer, is minimized by optimizing growth conditions. The primary characterization method is single-crystal x-ray diffraction (XRD), Chapter 3.3. The Ir surface topography is revealed by atomic force microscopy (AFM) scans, Chapter 3.2.

7.1 A-plane sapphire (a-ALO)

We focus mainly on iridium deposition on a-ALO substrates with different miscuts, i.e., surfaces at small angles to the a-plane. Commercial a-ALO 2 inch (5 cm diameter) wafers with high crystallographic quality are available at relatively low cost. Table 5.1 shows that the thermal expansion coefficients of sapphire are a reasonable match to diamond, better than MgO and STO, an advantage in decreasing the thermally-induced stress in the diamond film. In contrast to other materials with a cubic structure used for diamond substrates, sapphire has a hexagonal crystal structure with lattice constants: a=0.476 nm and c=1.299 nm, shown in Figure 7.1. Sapphire is thermally stable, with a high melting point at 2040 °C. No crystallographic phase transitions occur between room temperature and temperatures used for diamond growth, generally below 1200 °C.

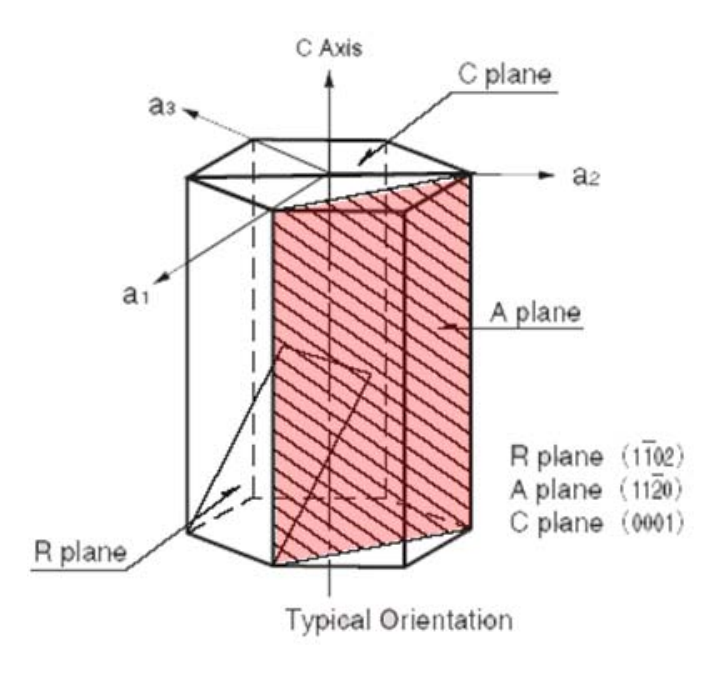


Figure 7.1 Hexagonal crystallographic unit cell of sapphire. The a-plane is shaded.

7.1.1 Epitaxial relation between Ir and a-ALO

For Ir heteroepitaxy on a-ALO, the lattice mismatch between Ir and sapphire is best understood by their atomic spacings, rather than by their lattice constants. Figure 7.2 is an applane projection of oxygen arrangements in a sapphire unit cell, showing the epitaxial relation of Ir atoms to an oxygen-terminated ALO surface. The spacing of O atoms in the $[1\bar{1}00]$ direction, or m-axis direction, is 0.275 nm which matches well the Ir spacing in its $[1\bar{1}0]$ direction, 0.272 nm. Along the [0001] direction, or c-axis of sapphire, the O spacing is 0.433 nm, giving rise to a atomic registration ratio of 3:2.

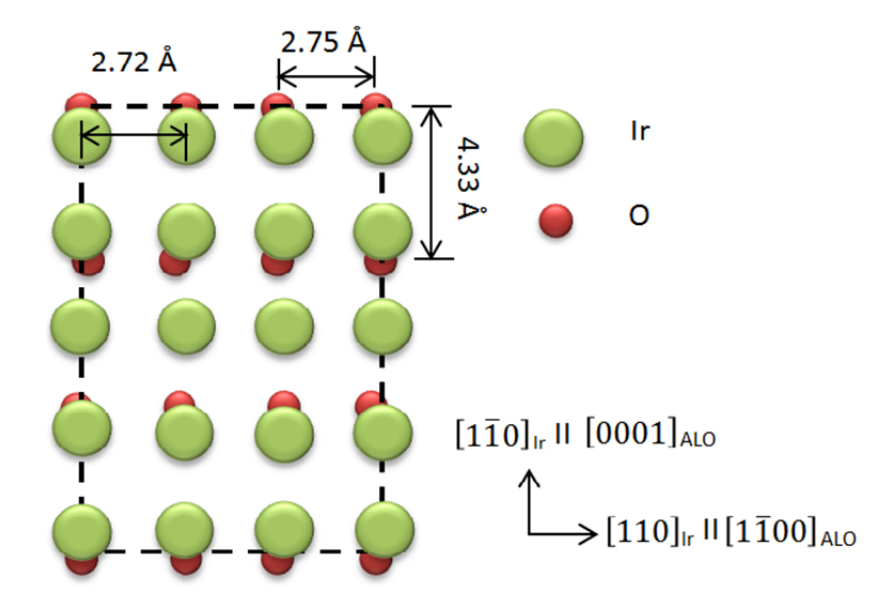


Figure 7.2 Illustration of proposed epitaxial relationship of Ir and a-ALO, where the small and large spheres represent the O and Ir atoms, respectively.

7.2 Ir sputtering procedure

a-ALO 2 inch diameter wafers with 4 different miscut angles were used as substrates: (1) nominally no miscut angle, denoted as 0-a-ALO (2) miscut angle of 1° rotated about c-axis (1C-a-ALO) (3) miscut angle of 1° rotated about m-axis (1M-a-ALO) and (4) miscut angle of 0.7° rotated about m-axis (0.7M-a-ALO). All wafers were specified to be one-side epi-polished and 0.5-mm thick. A flat on one side was oriented with its normal to the c-axis. Type (1) was obtained from Jiaozuo City Crystal; others were supplied by Substrates Technology. Type (1) substrates were found to have finite miscut angles, generally less than 0.3°, with random axis rotations.

7.2.1 Sapphire preparation

Prior to the Ir deposition, as-received wafers were processed in the KMF cleanroom. Macroscopic residues, such as dust particles, were removed by solvent cleaning in IPA with ultrasonic agitation, followed by blow-drying in N₂ to avoid any surface stains. This was followed by a high-temperature air anneal in an alumina tube furnace at 1300 °C for 24 hours for surface reconstruction. Temperatures were ramped up and down at 2.7 °C/min. The annealed wafers had strongly adhering particulates requiring another round of solvent cleaning. Figure 7.3 shows the surface topography, after annealing, of the four types of miscut a-ALO wafers studied.

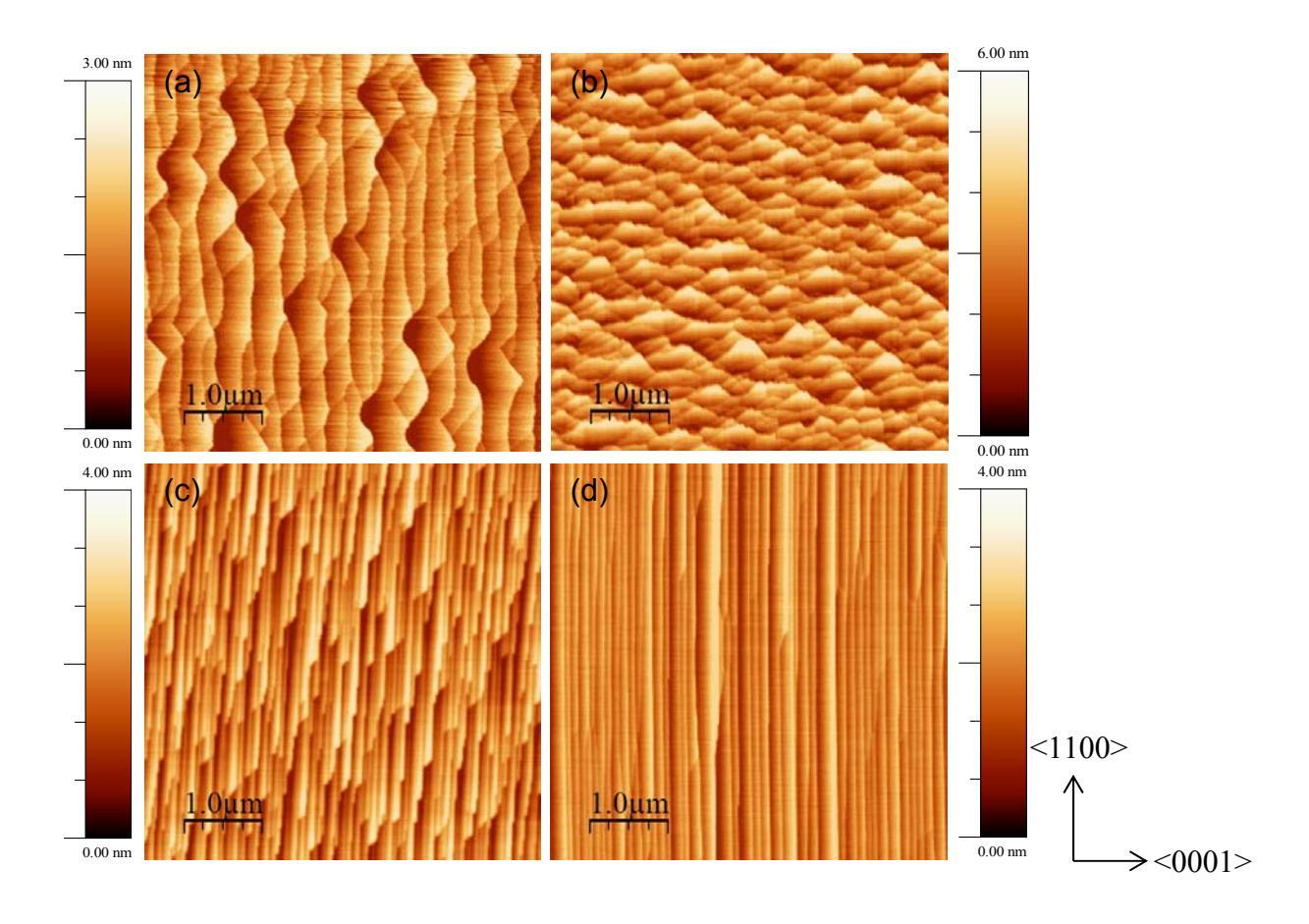


Figure 7.3 AFM images of annealed surfaces of (a) 0-a-ALO (b) 1C-a-ALO (b) 1M-a-ALO and (d) 0.7M-a-ALO wafers.

The surface reconstruction of a-ALO led to the development of surface terraces. They were generally irregular, with height differences of 4-6 unit cells in 1C-a-ALO wafers but with height differences of 2-3 unit cells for the others. The spacing and heights of terraces agreed with the miscut angle obtained by XRD orientation. Moreover, in Figure 7.3, the surface topography of annealed a-ALO is strongly dependent on the miscut angle and its rotation axis, as noted in previous studies. The 1C-a-ALO shows a tooth-like surface with a largest mean surface roughness, 0.87 nm. 1M-a-ALO and 0.7M-a-ALO show stripe-like features after annealing. The mean roughness increases with miscut angle: 0.41, 0.60, and 0.48 nm for a 0-a-ALO, 1M-a-ALO and 0.7M-a-ALO, respectively. The topography of a reconstructed surface also depends on annealing temperature and its duration. Figure 7.4, for example, compares the surface structures of 1C-a-ALO annealed at different temperatures. The tooth-like features are more distinct if the a-ALO surface is annealed at higher temperatures, in Figure 7.4(b).

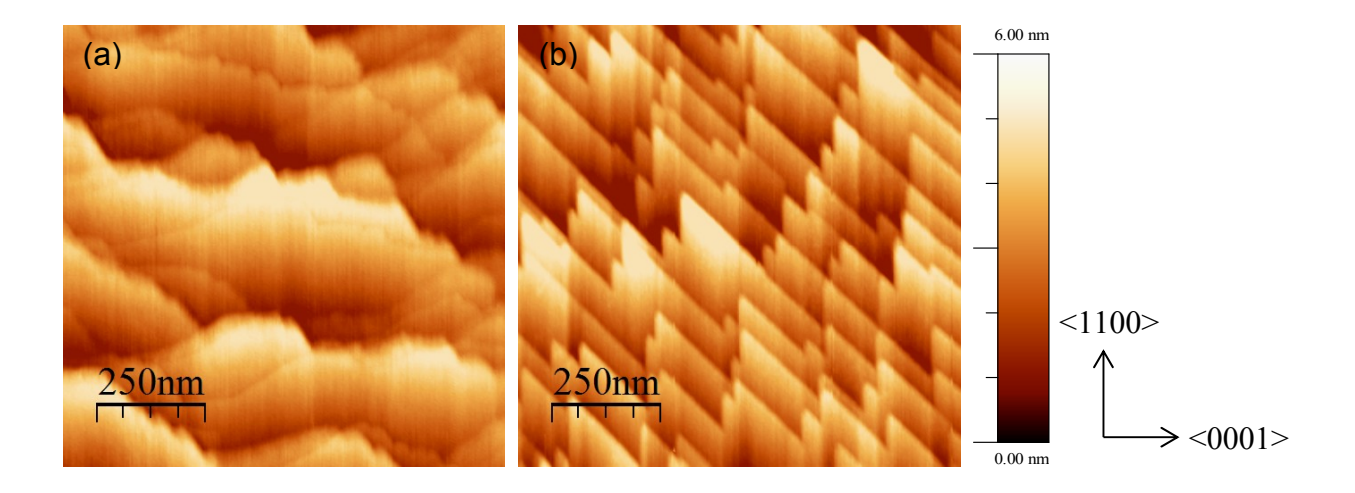


Figure 7.4 AFM images of 1C-a-ALO surface annealed at (a) 1300 °C and (b) 1500 °C for 24h.

7.2.2 Sample mounting and loading

Prior to Ir sputtering, a cleaned sapphire wafer was mounted in a sandwich structure composed of a 3.5 inch dia Inconel sample base plate or "puck" and a top 3.5 inch dia Mo capture ring. The capture ring had a 1.8 inch aperture and a 2-inch-dia recess that pressed the sapphire wafer against the puck. The structure was secured with stainless steel screws and lock washers. The substrate and mount were assembled in the cleanroom and transported to the AJA sputtering system with the protection of clean Al foil. The assembly was inserted into the load-lock of the sputtering system, pumped down to the mid-10⁻⁷ Torr range, and transferred to the main chamber whose minimum pressure was 2-3 10⁻⁸ Torr.

7.2.3 Ir DC sputtering

Before beginning sputtering, the Ar gas line was flushed for 15 min to reduce residual oxygen remaining in the gas lines. During this time, power supplies for the instrumentation were turned on and allowed to stabilize. The AJA system provides a computer interface for executing a sequence of operations and it allows the generation of a "stage" file. The stage file is created before each sputtering run; it can be saved as a record and reused for future runs. The steps for a typical Ir sputtering run are shown in Table 7.1. and were generated by the PHASEIIJ program which then executes the sequence.

Table 7.1 Typical steps for Ir sputtering. The pressure is set at 30 mTorr in the first step to ignite the RF plasma prior to substrate cleaning.

Step	Pressure (mT)	Power (W)	Ar flow rate (sccm)	Temperature (°C)	Deposition rate (nm/min)	Duration (min)
Ramping substrate temperature	30	0	15	25-850		6
RF bias cleaning on sapphire wafer	3	20	15	850		2.5
DC Ir sputtering (1)	3	20	15	850	1.2	10
DC Ir sputtering (2)	3	50	15	850	2.4	10
DC Ir sputtering (3)	3	75	15	850	3.6	10
DC Ir sputtering (4)	3	100	15	850	4.8	47.5

After the system was slowly cooled to room temperature, the sample puck was transferred to the load-lock. The load-lock was then vented with N_2 gas, the puck removed, and wrapped in aluminum foil for transfer to the cleanroom. The Ir surface must be protected as even a small scratch will generate lines of defects when diamond is overgrown. Finally, the wafer was characterized by XRD to confirm Ir structural quality.

An important attribute of the AJA system is its ability to rapidly heat a substrate, only 6 min to reach 850 °C from room temperature. This suppresses contamination from outgassing by allowing the walls of the main chamber to remain cool. During heating, the Ar pressure was kept

at 30 mTorr, rather than under vacuum, for rapid RF plasma ignition and to allow the puck to equilibrate with the surrounding gas.

7.2.3.1 Bias cleaning on a-ALO

Despite careful cleaning, sapphire substrates invariably have surface chemical residues, adsorbates, and very small particulates. The AJA system is equipped with a cleaning system that surrounds the electrically-isolated substrate with an RF plasma for an *in-situ* plasma cleaning just prior to sputtering. The plasma cleaning was found be essential for good Ir (001) heteroepitaxy on a-ALO. Without the plasma cleaning, sputtering under the same conditions led to Ir (111) growth. Figure 7.5 shows the dramatic difference between Ir grown on (a) high-temperature plasma-cleaned sapphire surface and (b) no cleaning. Note the complete absence of Ir (111) in (a). Figure 7.6 shows AFM images of the a-ALO surface before and after plasma cleaning. Sparse nanoparticles can be seen in (a) which cannot be removed by standard solvent cleaning whereas they are absent in (b).

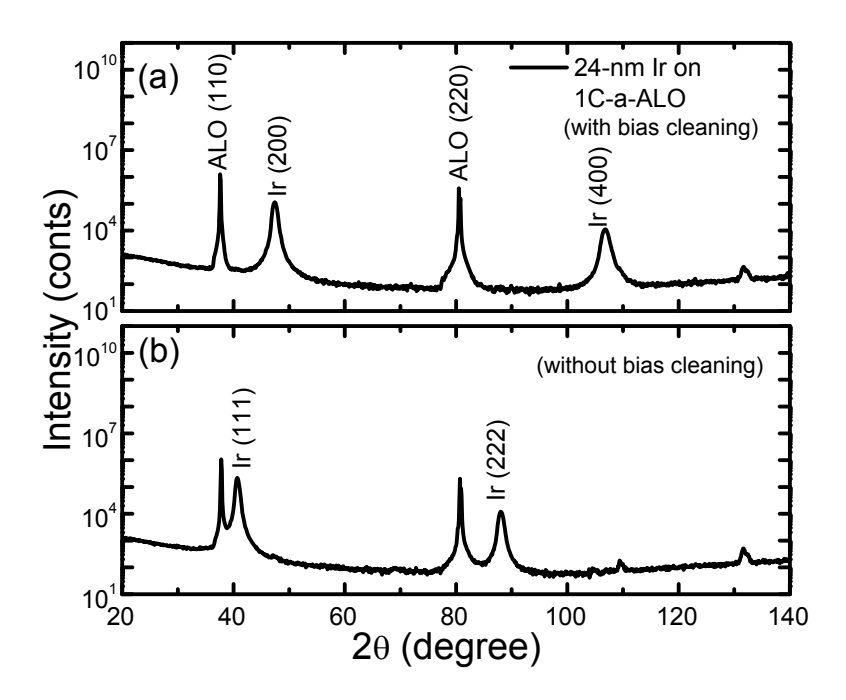


Figure 7.5 XRD diffraction patterns of 24-nm Ir on 1C-a-ALO substrates sputtered at 3 mTorr, 100W and 850 °C: (a) with plasma cleaning at 3 mTorr, 30W and 850 °C for 5 min and (b) without cleaning prior to the Ir sputtering.

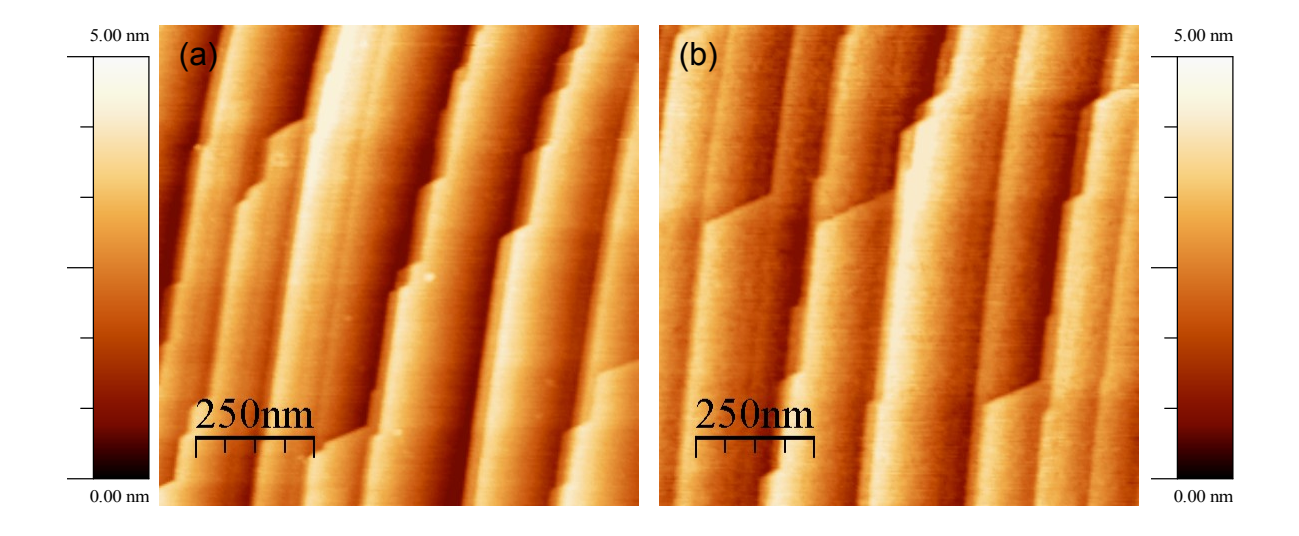


Figure 7.6 AFM images of a-ALO (a) before plasma cleaning and (b) after plasma cleaning at 3 mTorr, 30W and 850 °C for 5 min. The sparse bright spots in (a) are nanoparticles which cannot be removed by standard solvent cleaning.

Excessive plasma cleaning can damage the substrate surface and cause deterioration of the crystal quality of the Ir epitaxial layer. As shown in Figure 7.7, the (002)_{Ir} XRD rocking curve linewidth has a strong positive correlation with cleaning duration, but only slightly changes with bias power, having a minimum at 20W. Figure 7.8 shows the Ir surface topography after deposition on an excessively cleaned (10 min) substrate resulting in a discontinuous Ir film. As a consequence, only a short exposure to the plasma is sufficient. Therefore, the substrate surface was cleaned at 30W for 2.5 min in a standard process.

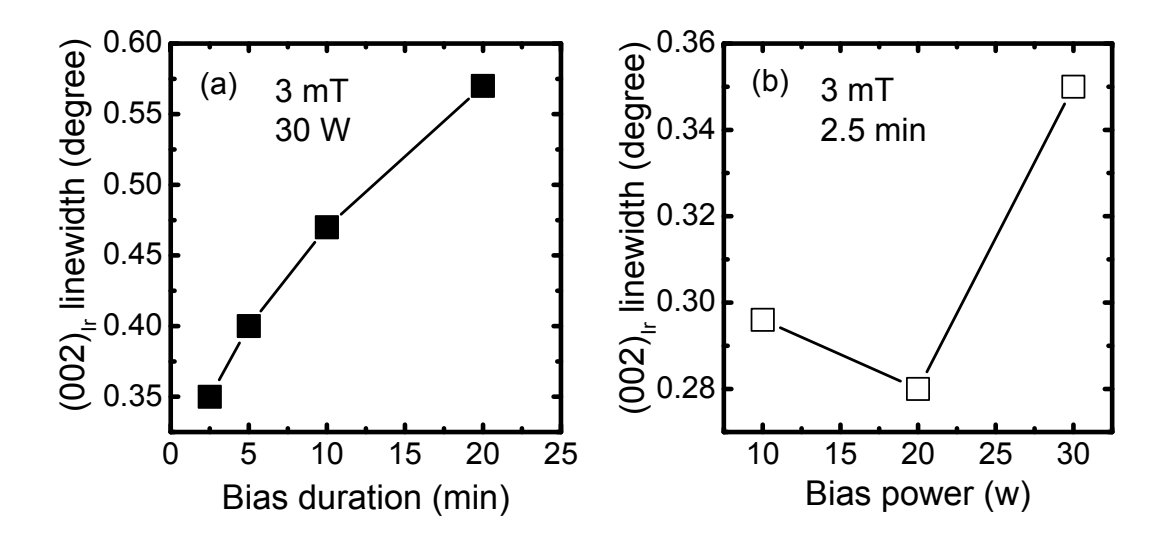


Figure 7.7 Linewidth of (002)_{Ir} XRD rocking curve vs. (a) bias duration and (b) bias power.

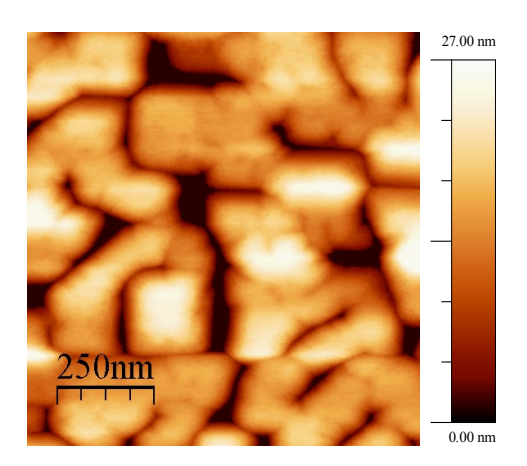


Figure 7.8 AFM image of 300-nm Ir on a-ALO plasma cleaned at 3 mTorr, 30W and 850 °C for 10 min.

7.2.3.2 Ir DC sputtering rate

The sputtering rate is generally a function of process pressure and power as shown in Figure 7.9 for Ir sputtering in the AJA system. The rate monotonically increases with power, but surprisingly, is independent of pressure at fairly low Ar pressures. At higher pressures, arcing due to the small gap between the sputtering gun's ground shield and Ir target occurred above 20 mTorr. There is a relatively short distance (about 10 cm) between the 2 inch diameter sputtering target and the 2 inch substrate, so the deposition is highly directional.

For the Ir sputtering process described in Table 7.1, the initial sputtering rate was relatively slow, 1.2 nm/min, to suppress the formation of non-epitaxial grains, and then it was ramped up gradually to 4.8 nm/min to shorten the processing time.

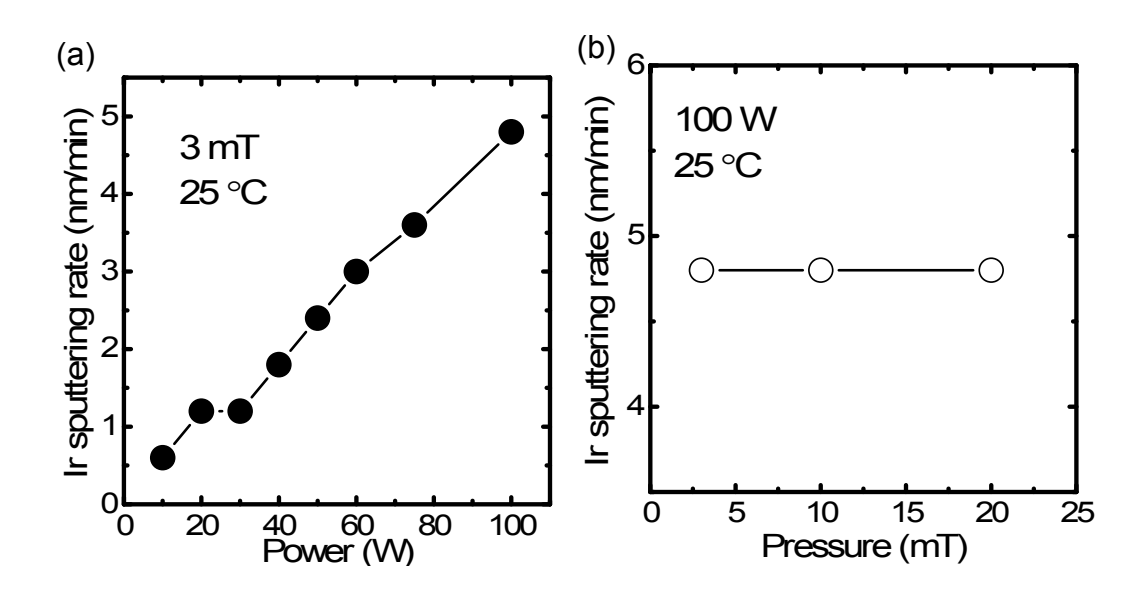


Figure 7.9 Ir sputtering rate vs. (a) sputtering gun power and (b) Ar pressure in the AJA system measured at room temperature.

7.3 Results for Ir (001) epilayers

7.3.1 Ir x-ray diffraction (XRD)

A typical XRD ω -2 θ scan is shown in Figure 7.10. Only diffraction peaks from Ir (200) and the underlying a-ALO (11 $\overline{2}0$) are visible. Traces such as these were independent of the sapphire miscut angle. Epitaxial alignment was confirmed by ϕ -scans of the (111) Ir reflections. It was found previously that small amounts of Ir (111) were present when electron-beam evaporated Ir or sputtered Ir without plasma cleaning was deposited. Sensitivity to miscut angle was also seen previously. Thus the reproducible Ir growth can be attributed to plasma cleaning and the rapid heating provided by the AJA system. A typical XRD rocking curve is shown in Figure 7.11. In over 20 Ir sputtering runs, the Ir (200) linewidth for films prepared under the conditions shown

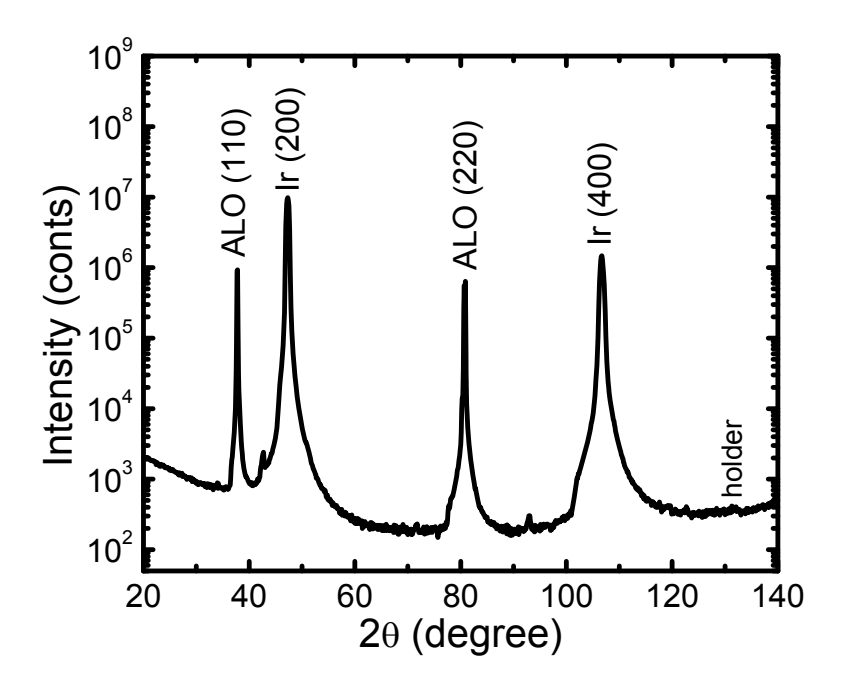


Figure 7.10 XRD diffraction pattern of 300-nm Ir on highly-oriented a-ALO. Small peaks originate from the small fraction of Cu K_{β} radiation in the incident x-ray beam.

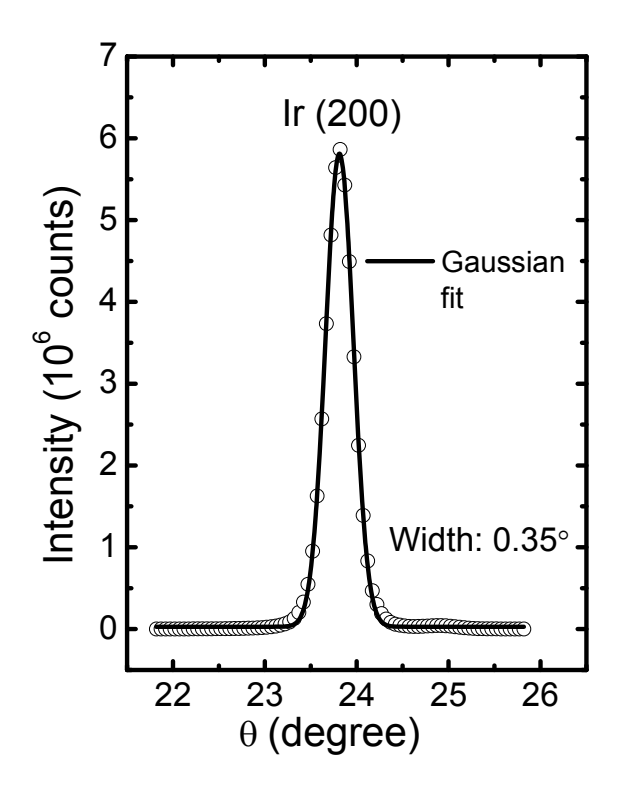


Figure 7.11 X-ray rocking curve of Ir (200) with Gaussian fit.

in Table 7.1 was $0.35\pm0.04^{\circ}$. This is somewhat larger than the best films prepared previously by electron-beam evaporation, which were as low as 0.21° . Figure 7.12 shows that the linewidth of the Ir (200) reflection for a 150 nm Ir film decreases with increasing growth temperature. Due to limitations of the AJA quartz heaters, the maximum substrate temperature was limited to 850 °C.

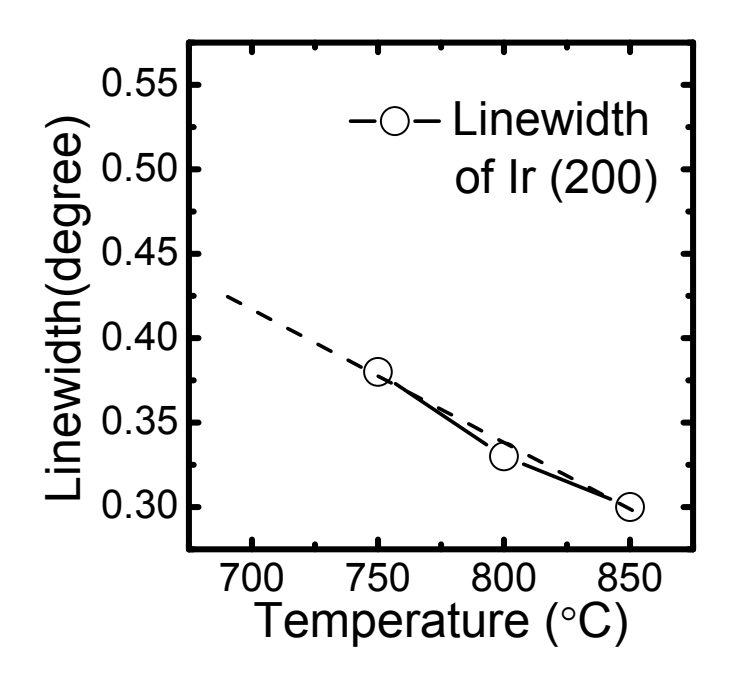


Figure 7.12 Ir (200) rocking-curve linewidth vs. substrate deposition temperature.

7.3.2 Ir surface topography on a-ALO

The surface topography of 300-nm Ir films sputtered at 850 °C substrate temperature depends on the sapphire miscut angle. The topography of the substrate is not necessarily transferred to the Ir at this thickness, as can be seen in Figure 7.13. This sensitivity differs from earlier studies with Ir sputtered in a different deposition system. Ir on highly-oriented a-ALO shows cross-like features, whereas Ir on substrates with larger vicinal angles has star-like aggregations. Note that the highest mean surface roughness, 1.1 nm, occurs on the 1C-a-ALO.

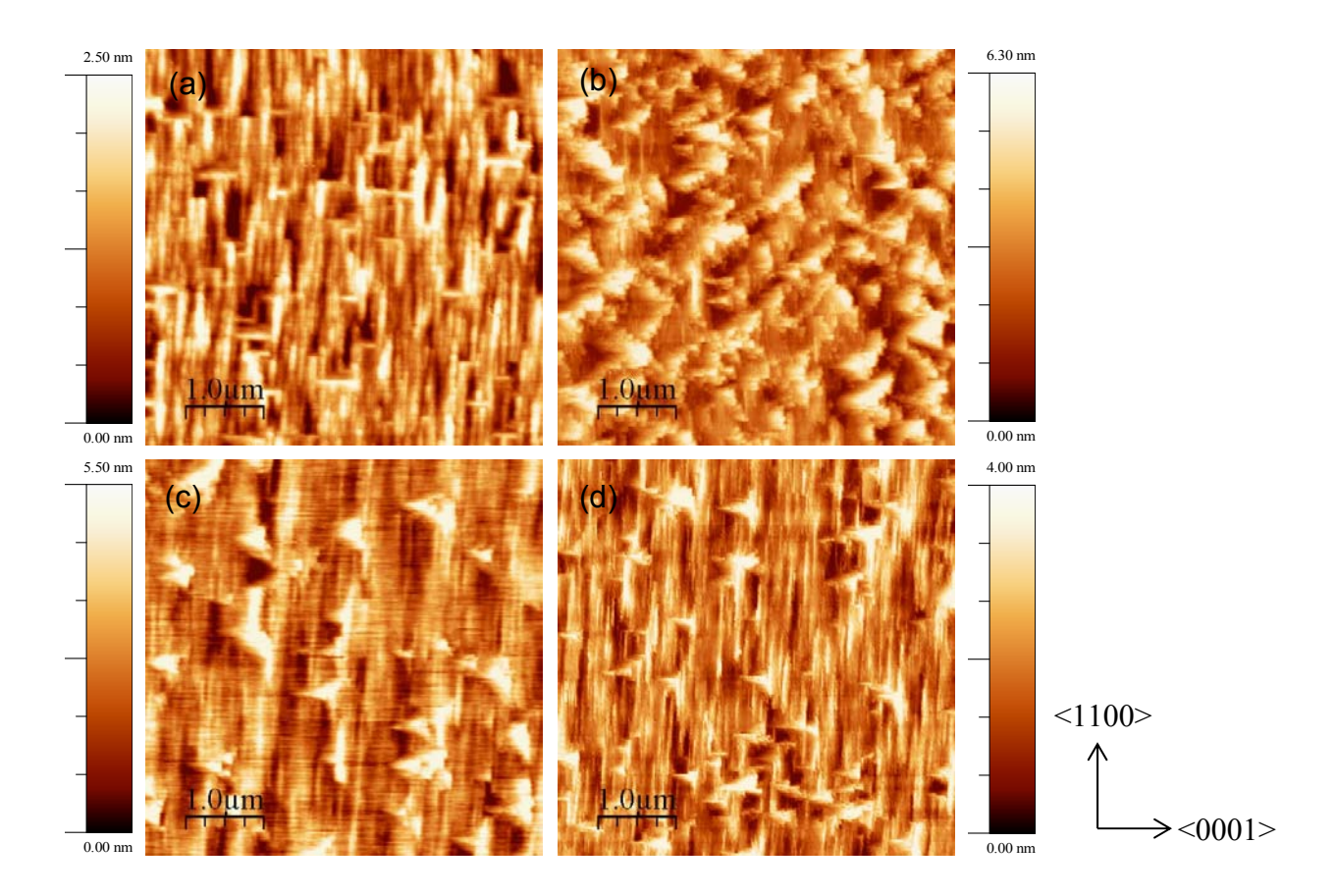


Figure 7.13 AFM images of 300-nm Ir sputtered by the process in Table 7.1 on a (a) 0-a-ALO (b) 1C-a-ALO (c) 1M-a-ALO and (d) 0.7M- a-ALO.

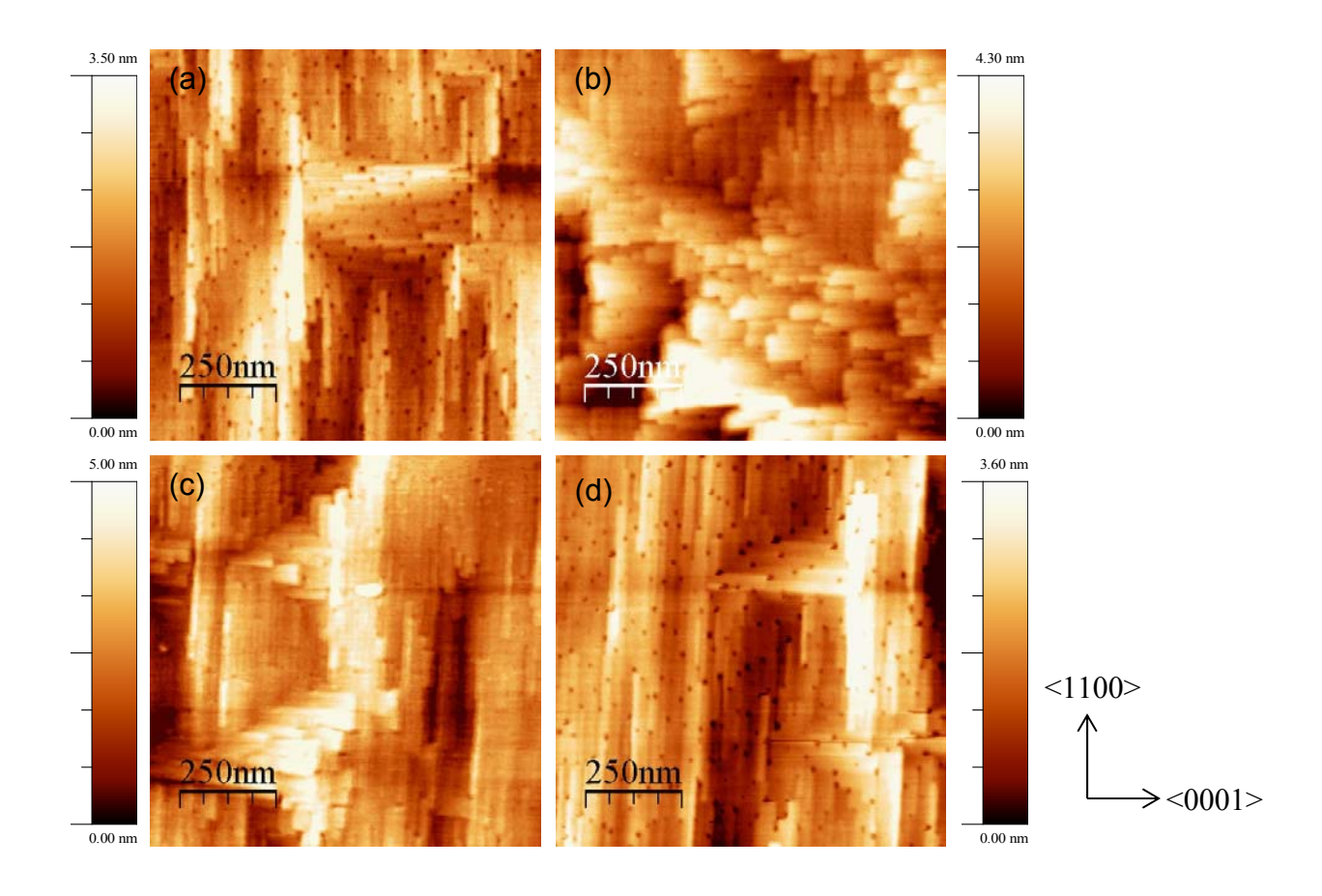


Figure 7.14 High-resolution AFM images of 300-nm Ir on a (a) 0-a-ALO (b) 1C-a-ALO (c) 1M-a-ALO and (d) 0.7M-a-ALO.

The mean surface roughness of Ir on a 0-a-ALO, 1C-a-ALO and 1M-a-ALO substrates is 0.49, 1.03, and 0.78 nm, respectively. Compared to the bare a-ALO surface, the Ir surface roughness increases by 0.3-0.4 nm on a-ALO substrates with the larger vicinal angles, but it does not change for Ir on a highly-aligned a-ALO substrate. The formation of star-like features enhances surface roughness. Figure 7.14 shows AFM images of Ir surfaces at higher resolution. It appears that there is a competition between c-axis and m-axis directional growth; when they exist in nearly equal amounts star-like features are more likely to be formed, as seen in Fig. 7.14 (b).

Experiments were also carried out on unannealed a-ALO substrates with Ir sputtered to a 24 nm thickness. As seen in Figure 7.15 (a), Ir developed textures parallel to the m- and c-axes of a-ALO with a small mean roughness of 0.2 nm on highly-oriented sapphire. The textures aligned with the c-axis in (b) the 1M miscut, and then coalesced laterally, with a roughness of 0.52 nm. The star-like features, meanwhile, started to develop on both substrates as high steps in AFM images.

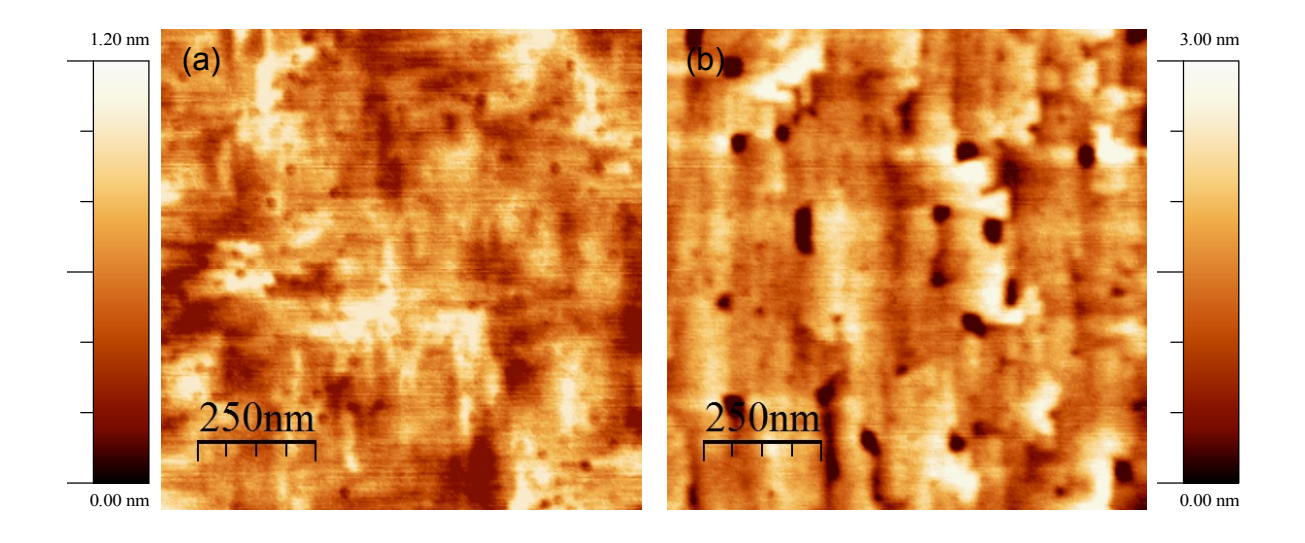


Figure 7.15 AFM images of 24-nm thick Ir on unannealed (a) 0-a-ALO and (b) 1M-a-ALO.

As a result of strong Ir-Ir bonding, the surface diffusion of Ir atoms is very low, leading to textured, rough surfaces. The diffusion rate of Ir changes with sputtering parameters such as pressure, power and substrate temperature, and is the origin of the different surface features. In Ir films prepared in the AJA system, the Ir surface topography is, somewhat surprisingly, independent of growth temperature in the range studied but more dependent on the sputtering pressure. At 10 mTorr Ar pressure, Ir prefers to aggregate on the a-ALO surface. The surface, as a result, was composed of spherical Ir nanograins with large mean surface roughness near 2 nm, Figure 7.16. Despite the granular appearance, the Ir grew epitaxially at this pressure, with a

rocking curve linewidth comparable to results for films grown below 3 mTorr. There is clearly a need for more careful investigation of the relationships between sputtering parameters, XRD linewidths, and Ir topography.

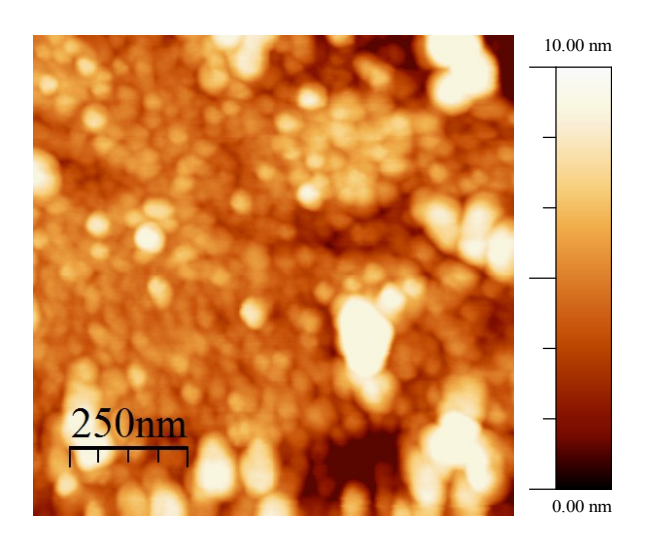


Figure 7.16 AFM image of 150-nm Ir sputtered at 10 mTorr, 100W and 850 °C.

7.4 Ir-ALO wafer processing

Following Ir deposition, the 2 inch wafer was inspected under a high-power optical microscope for growth defects and particulates. The entire wafer was coated with a layer of photoresist to protect the Ir surface and then exposed to UV light through a specially-designed low-resolution transparency film mask for reasons noted below. Prior to PR developing, the wafer was diced with a diamond cut-off wheel under low-light conditions. Dicing resulted in 9 nominally 10×10 mm² substrates per wafer. To identify ALO orientation, the chips had actual dimension 9.8×10.0 mm², with the long dimension along the c axis. Since the wafer was mounted on the vacuum chuck of the dicer, the sapphire was not completely cut through. It was subsequently easily broken into individual chips with slightly roughened edges. After developing

the PR, the chips were cleaned and ultrasonicated in a dilute Alconox detergent solution and rinsed in DI water.

Sapphire substrates are highly insulating even at temperatures where the BEN process is used. During BEN, a continuous current must flow from the top of the Ir surface to the Mo post below the substrate. Therefore, continuity between top and bottom substrate surfaces was produced by depositing a continuous Ir coating that connected the substrate's major surfaces by conducting edges. A thin 60 nm film of Ir was sputtered in the APX sputtering system with the substrates at room temperature. Three separate Ir depositions were needed, one that coated the back surfaces of the ALO chips, and two more that connected the front and back surfaces via two edges. For back coating, the substrates simply faced down on the sample holder followed by two rounds of side coating, where a special aluminum holder was used as shown in Figure 7.17. The reason for the special PR mask was to protect the epitaxial Ir on the front surface except for a small contact channel to one of the Ir-covered edges. Since the APX system was highly contaminated, it was necessary to increase the Ar flow rate to a few tens seem to avoid a highly resistive film. Tests with an ohmmeter gave a few ohms DC resistance across 1 cm. Finally, the protective PR layer was removed in solvent.

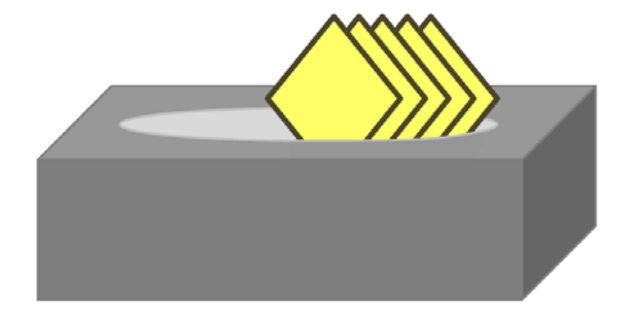


Figure 7.17 Illustration of sample holder for substrate side coating.

8. Chapter 8 Heteroepitaxial growth of diamond

In this chapter we describe a robust procedure for growing heteroepitaxial diamond films on Ir epilayers by CVD. A method for achieving highly efficient bias enhanced nucleation (BEN) on 1 cm² substrates is the most crucial step in the overall process. To achieve high nucleation density of diamond on Ir, a multitude of issues associated with BEN were addressed, many of which are influenced by small details of plasma and system geometry. Growth of thick diamond is discussed along with the physical characterization of the resulting diamond single crystal films. Topics include structural perfection, surface morphology, and stress state.

8.1 Fixtures for biasing

Figure 8.1 shows the bias set up including cooling stage, sample holder and the bias ring. Growth is carried out under the same geometry. The bias ring, which is supported by Mo posts, and the cooling stage are grounded. The bias lead is electrically isolated by a fused quartz tube. During bias, a negative voltage is applied by a DC power supply to the bias lead. The Mo sample post, the base plate, Ir/a-ALO substrate and cap are maintained at bias potential. The Mo base plate is isolated from the cooling stage by ceramic spacers. The shield plate is electrically isolated by ceramic spacers and is at a floating potential. With microwave plasma present, application of a bias voltage, typically between -150 and -250 V, forms a DC glow above the cap and substrate surface.

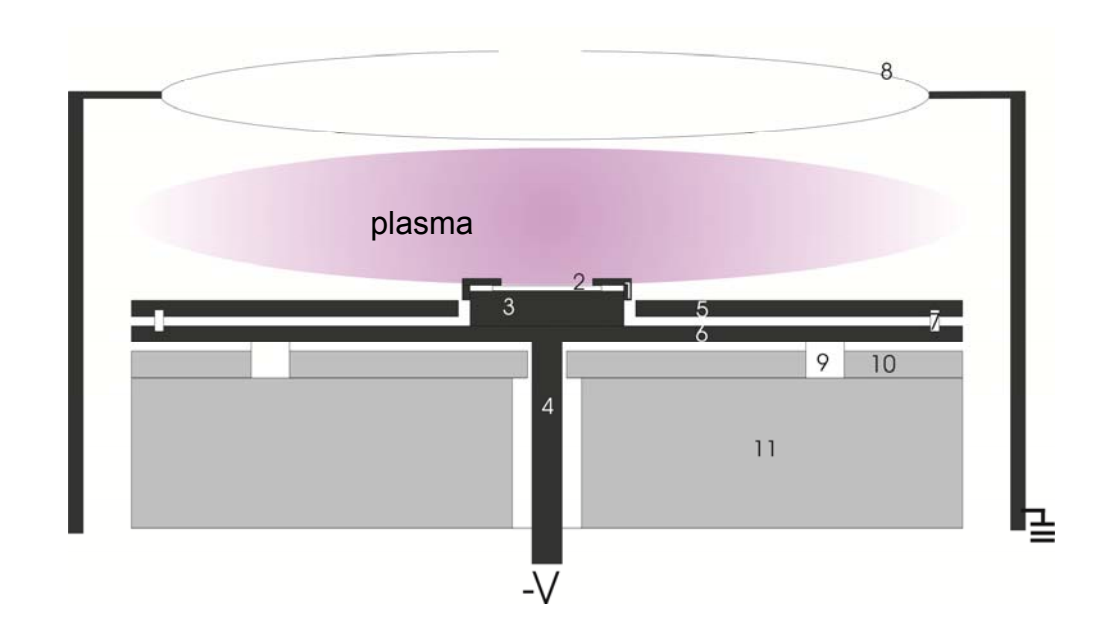


Figure 8.1 Fixturing for the CVD reactor: (1) Mo cap (2) Ir/a-ALO substrate (3) Mo post (4) bias lead (5) Mo shield plate (6) Mo base plate (7) ceramic spacer (8) tungsten bias ring (9) ceramic spacer (10) stainless steel plate (11) grounded cooling stage.

8.2 Procedure for diamond growth

In Figure 8.2, a typical procedure for CVD diamond growth is shown. It consists of a short hydrogen plasma cleaning, a carburization step where methane in introduced into the system, the BEN step, and the growth step. Table 8.1 gives the parameters used to produce 550 nm diamond substrates on an epitaxial Ir layer on sapphire. The reactor was modified from its previous configuration by the introduction of a water-cooled stage to allow higher microwave power during biasing and growth while maintaining a low substrate temperature. The detailed configuration of the CVD reactor was described in Chapter. 4.3.1.

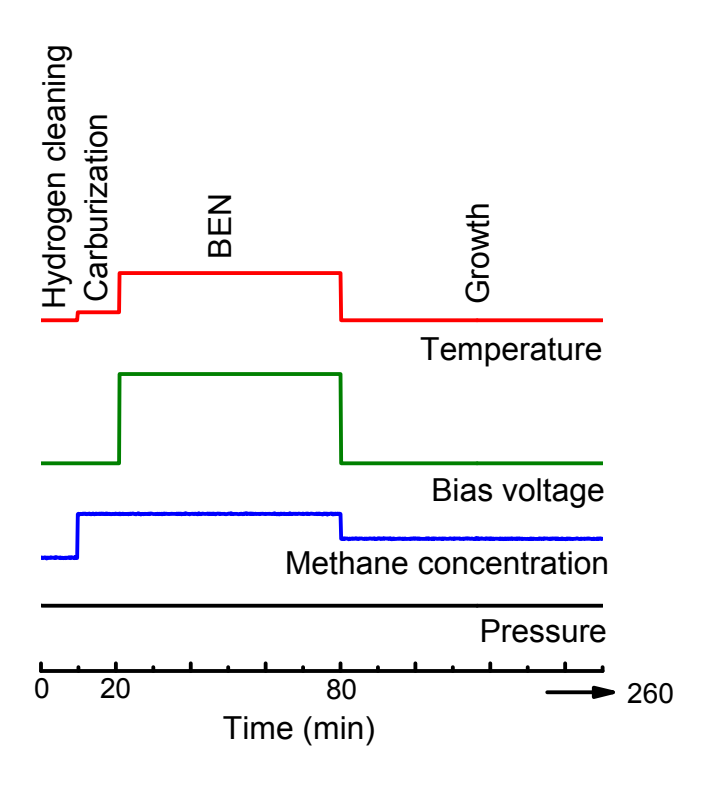


Figure 8.2 Time plot of the standard procedure of heteroepitaxial CVD diamond growth.

Table 8.1 Detailed conditions for CVD diamond thin film growth, with temperature measured on the Mo cap by a single-color pyrometer.

	H ₂ plasma cleaning	Carburization	Bias	Growth
Pressure (Torr)	18	18	18	18
H ₂ (sccm)	300	300	300	300
CH ₄ (sccm)	0	6	6	3
Temperature (°C)	670	680-670	710-730	670
Duration (min)	10	10	60	180

The diamond growth carried out previously in this reactor was restricted to 5 mm square SrTiO₃ (STO) substrates, with a growth region 3.5 mm diameter. Scaling the process to 10 mm square sapphire substrates had not been successful. A major problem was the inability to provide uniform nucleation with the larger substrates over a diamond growth area 8 mm in diameter. The larger area requires a higher bias current to maintain the same current density. Two ways to accomplish this are by (1) better confinement of current paths and (2) increased negative bias potential. Higher potentials lead to plasma instabilities, breakdown, and arcing. These issues were addressed by small changes in the fixture geometry and by additional shielding. The changes were subject to constraints such that the substrate temperature and plasma composition at the substrate be maintained at the conditions for optimal diamond growth.

Sapphire substrates are superior to STO in a number of ways. They are mechanically stronger, have better crystallographic quality, are available as very large wafers, and are generally less costly. STO has one advantage however: it develops a low electrical conductivity when processed at high temperatures due to oxygen loss. This is not the case for ALO which is not easily chemically reduced and maintains its insulating ability to temperatures well above diamond growth conditions. Whereas STO readily conducts a bias current from its Ir-covered top surface to its bottom surface, ALO does not. Using the fixturing illustrated in Figure. 8.1, it appears that a continuous path exists between the Ir surface, through the Mo top cap and post, to the bias lead. However, the cap only rests on the Ir substrate surface and may not make good electrical contact if it contains insulating deposits or if cap-post contact is poor. This was identified as a major source of variability in the bias processing. The best solution was to deposit Ir on the sides and bottom surface of the ALO substrate, as detailed in Chapter 7.4. With this,

and other adjustments, the reproducibility of growing diamond films was improved so that good quality films could be grown consecutively as illustrated in Figure 8.4.

8.3 Result of BEN on Ir

A high nucleation density of diamond on Ir/a-ALO (10×10 mm²) was obtained by optimizing the geometry and the growth parameters. Table 8.2 lists the bias parameters for the geometry described above. Figure 8.3 shows the surface morphology of a well-biased Ir surface. After of 60 min, the bias voltage was turned off with the microwave plasma on. To study the results just after bias, microwave power and bias voltage were simultaneously reduced to zero. A thin layer of amorphous carbon covered the biased Ir, showing bright contrast in an SEM image, Figure 8.3(a). The Ir has a surface covered with Ir nanopillars formed by the ion bombardment, Figure 8.3(b), where the mean lateral size of an Ir pillar is 11.3±2.3 nm. A similar Ir morphology is shown in Figure 5.13 where the size and height of an Ir pillar is 8±0.5 and 4.5±0.5 nm, respectively. As shown in Figure 5.14(b), diamond is most likely to nucleate between the Ir nanopillars. The density of Ir dots, thus, represents a lower bound on the nucleation density. In Figure 8.3(b), the density of Ir dots is 10¹² cm⁻².

Table 8.2 Standard bias conditions.

Pressure (Torr)	Power (W)	Bias voltage (-V)	Bias current (-mA)	Bias temperature (°C)	Duration (min)
18	1550	170-180	90-70	710-730	60

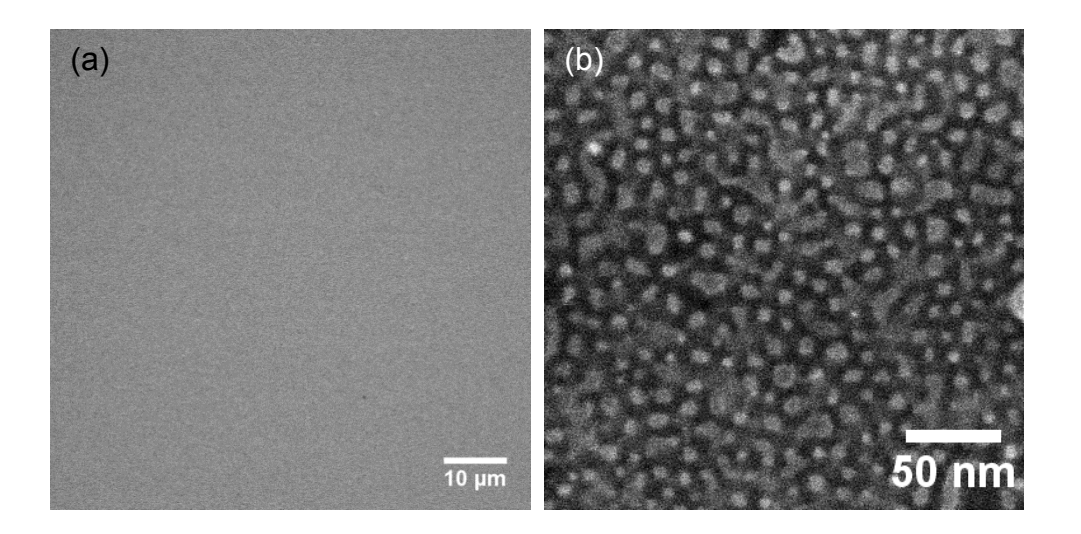


Figure 8.3 Plan-view SEM images of biased Ir surface: (a) the featureless amorphous carbon layer covering the Ir surface and (b) Ir nanopillars buried in the carbon layer.

8.4 Heteroepitaxial CVD diamond thin film growth

With the high nucleation density, a diamond thin film was able to coalesce in 30 min or less. The optical images of selected diamond thin films with good coalescence are shown in Figure 8.4 where four samples were grown in a sequence and the growth region is 8 mm in diameter, limited by the aperture of the Mo cap. Figure 8.5 shows a typical SEM image of a 3h-grown diamond thin film which is well-coalesced with a flat top surface. Boundaries between coalesced regions are not observed in good films. Since the growth was done at relatively low pressure, 18 Torr and 670 °C (measured on the Mo cap by a single color pyrometer), the growth rate was 160-180 nm/h. Thus, after a typical 3h growth, the thickness of the diamond film was about 550 nm. The film in Figure 8.4 is transparent and interference fringes are observed from light reflected between the diamond and Ir surfaces due to the radial thickness variation.

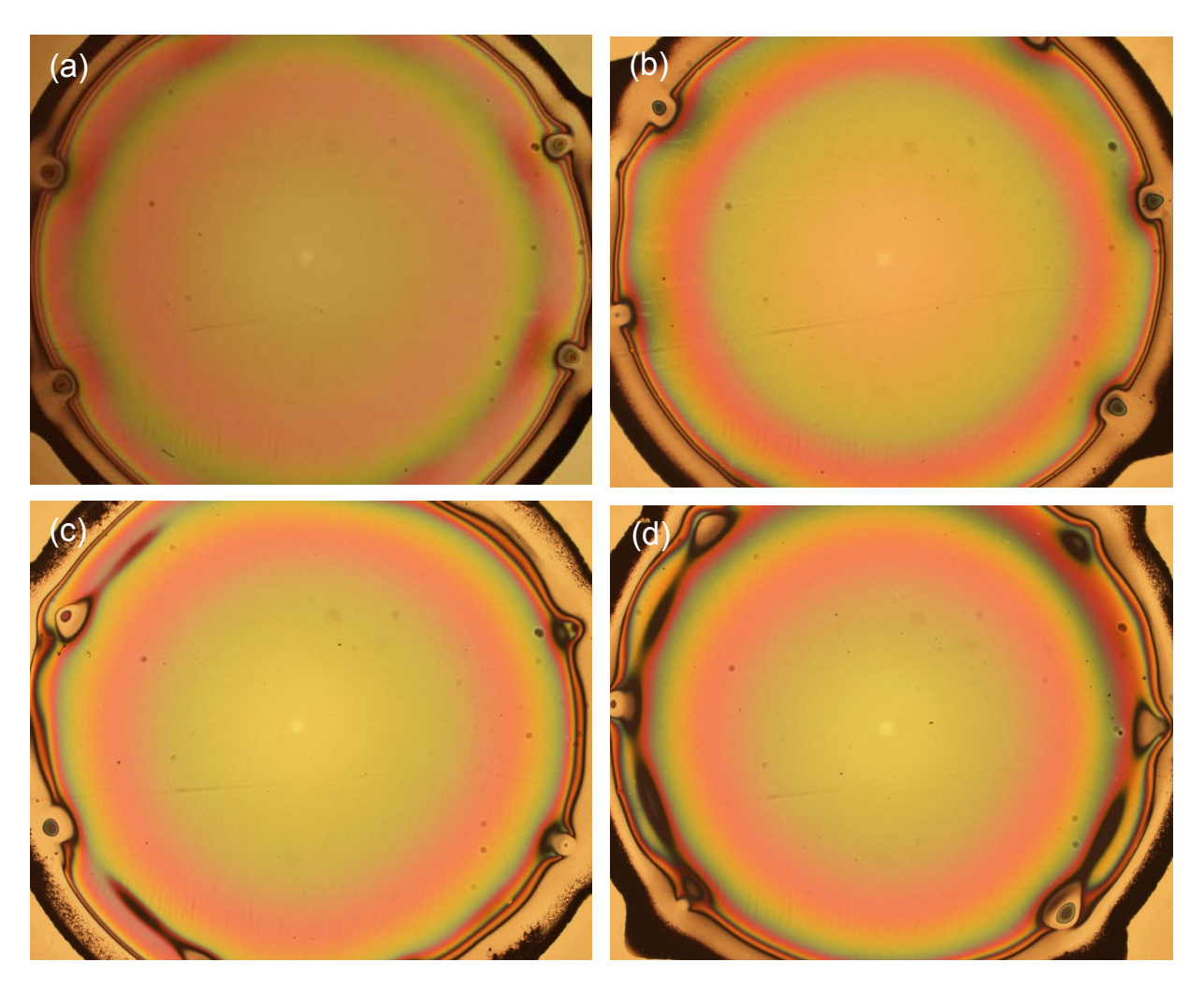


Figure 8.4 Four selected optical images of 550 nm diamond thin films, grown in a sequence. The burn marks on edges are caused by the Mo cap. (b) Film is about 100 nm thicker than other samples at its center.

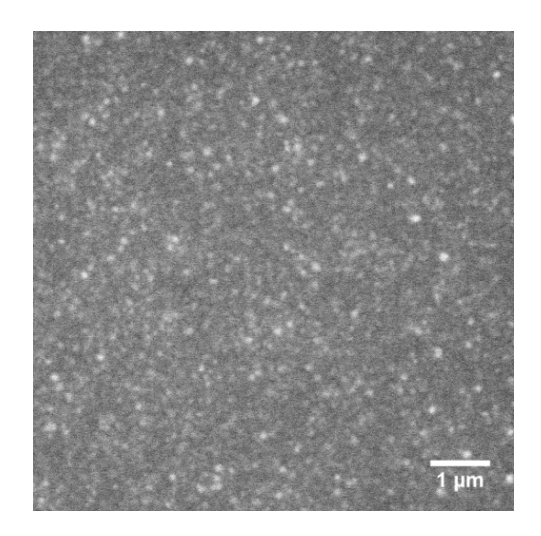


Figure 8.5 Plan-view SEM image of 3h-grown diamond thin film showing a well-coalesced diamond (001) surface. Bright dots are small height fluctuations on the diamond surface.

Figure 8.6 is a typical ω -20 XRD pattern of a 550 nm heteroepitaxial diamond thin film on a Ir (001)/a-ALO substrate. Diffraction peaks from a-ALO, Ir, and diamond are observed owing to the long x-ray absorption length in diamond and Ir, nearly 700 and 2.45 μ m respectively. Only the diamond (400) reflection is observed, consistent with {001} diamond planes. Since the pattern could arise from a polycrystalline film with (001) texture, it is necessary to carry out a ϕ -scan, Figure 8.7, to confirm the film is single crystal. Observation of the 4 (111) reflections during a 360° rotation about the (001) axis confirms this. A rocking-curve gives a 1° linewidth, indicating a significant mosaic spread at this thickness.

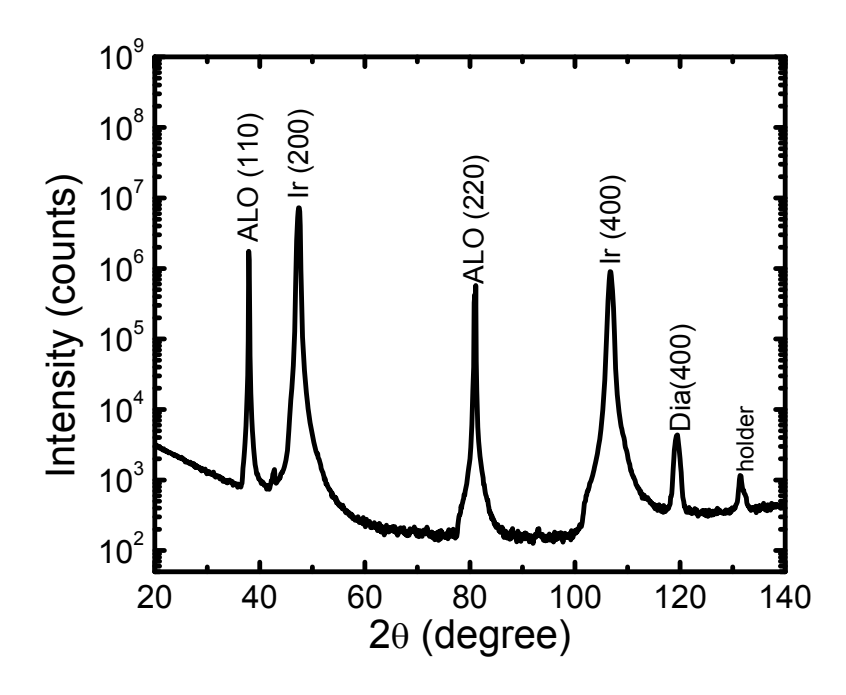


Figure 8.6 XRD diffraction pattern of 550-nm diamond on a Ir/a-ALO substrate. Small peaks originate from the small fraction of Cu K_{β} radiation in the incident x-ray beam.

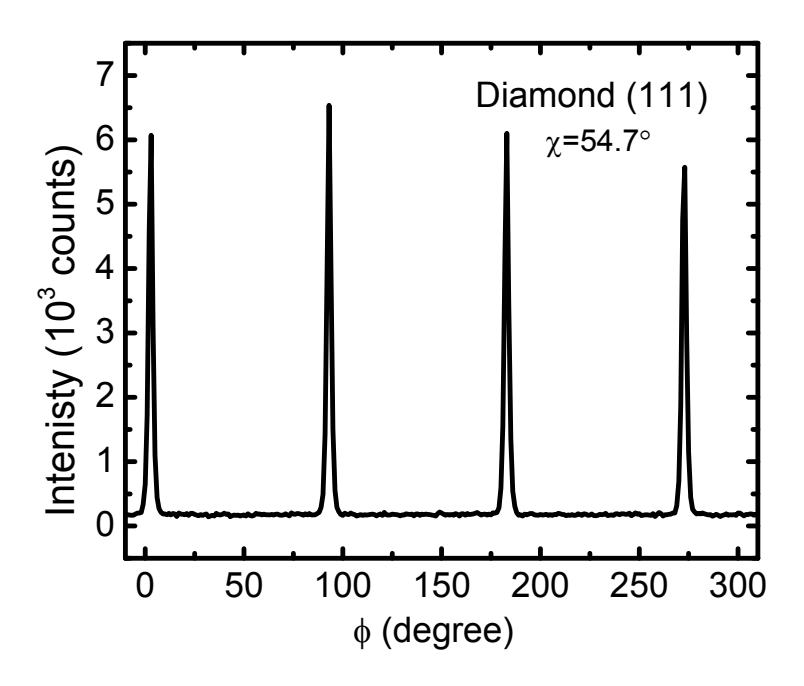


Figure 8.7 XRD φ-scan of 550-nm diamond on a Ir/a-ALO substrate.

8.5 Procedure of thick diamond growth in AsTex

Starting with 550 nm diamond substrates, growth of thicker films was carried out in the AsTex reactor. The fixturing around the sample was shown in Figure 4.9, generally similar to that in the CVD reactor. After pumping overnight with a turbo-molecular pump, the pressure in the main chamber reached 10⁻⁷ Torr. During growth, the hydrogen flow rate was set at 300 sccm. Other input parameters, such as pressure, microwave power, and the methane concentration, are variables. Hydrogen is introduced and a microwave plasma discharge is started. Power is adjusted until the appropriate substrate temperature, measured with a single-color pyrometer, is reached. After stabilization, methane is introduced into the chamber, initiating growth. After growth, system is cooled slowly to room temperature to avoid thermal shock.

8.6 Heteroepitaxial CVD diamond thick film growth

A diamond sample with a thickness greater than 20 µm is referred to a thick film. Three thick diamond films grown on diamond substrates are now described, labelled A, B, and C. The growth conditions for each sample are listed in Table 8.3. All were covered with a Mo cap during growth. The Mo cap, identical to the ones used in the CVD system, surrounded the substrate with an 8 mm diameter aperture. For the growth of sample C, a cylindrical rounded Mo dome surrounded the cap. All diamond films and their substrates exhibited cracking after cooldown to room temperature after the last growth step.

Table 8.3 Detailed growth parameters of thick heteroepitaxial diamond. Row lists the corresponding growth conditions. Multiple growth steps were used for samples A and B. The listed temperature is the reading from a single color pyrometer focused on diamond top surface.

Sample #	Pressure (Torr)	Power (W)	CH ₄ (%)	Temperature (°C)	Duration (h)	Thickness (µm)
A	30	650	1	660-670	0.75	
	30-60	650-700	1-4	830	4	
	60	700	4	830-840	85.25	85
В	60	600-700	5	800-810	4.3	
	60	700	5	810	23	
	60-90	700-750	5	880	1.7	
	90	750	5	930	46	70
С	90	1100	5	690-665	49	60

Due to the thermal stress resulting from the thermal mismatch between substrate and diamond, all of the thick diamond films peeled from the a-ALO substrate, denoted as "delaminated", during cooling. Moreover, in the diamond growth area, the BEN-treated Ir layer always adhered to the diamond whereas the untreated Ir surface stayed on the a-ALO substrate, implying the improvement of Ir adhesion to diamond by BEN. Figure 8.8 presents the diamond (111) cleavage plane of (001) single crystal diamond.

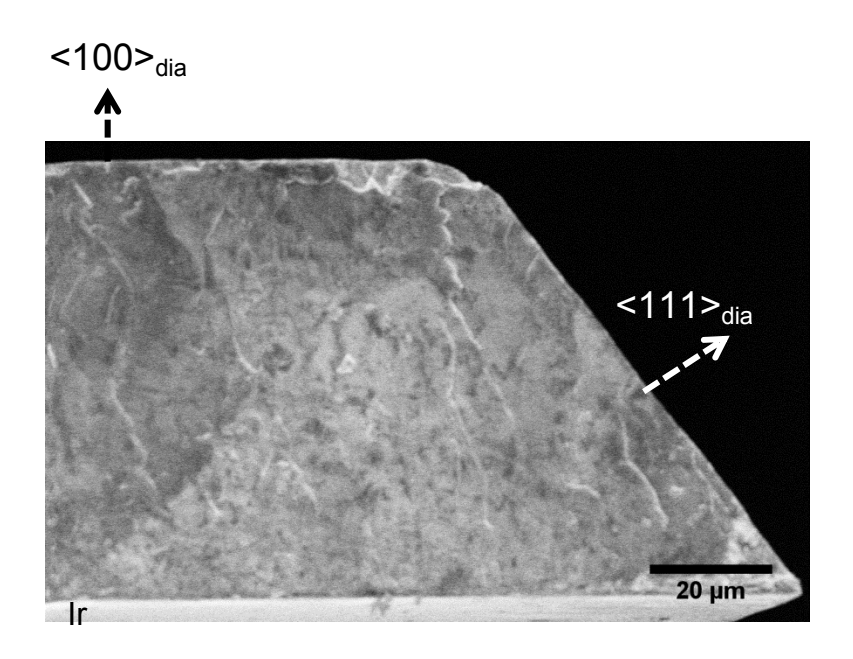


Figure 8.8 Cross-sectional tilted SEM image of a 70-μm delaminated diamond (001) piece showing a (111) cleavage. At bottom is the Ir layer.

In Figure 8.9, diffraction peaks from a delaminated diamond/Ir film are shown. Compared to Figure 8.6, the intensity of the diamond (004) peak has increased significantly, 30 times, relative to the initial diamond film intensity, a result of its greater thickness and the long

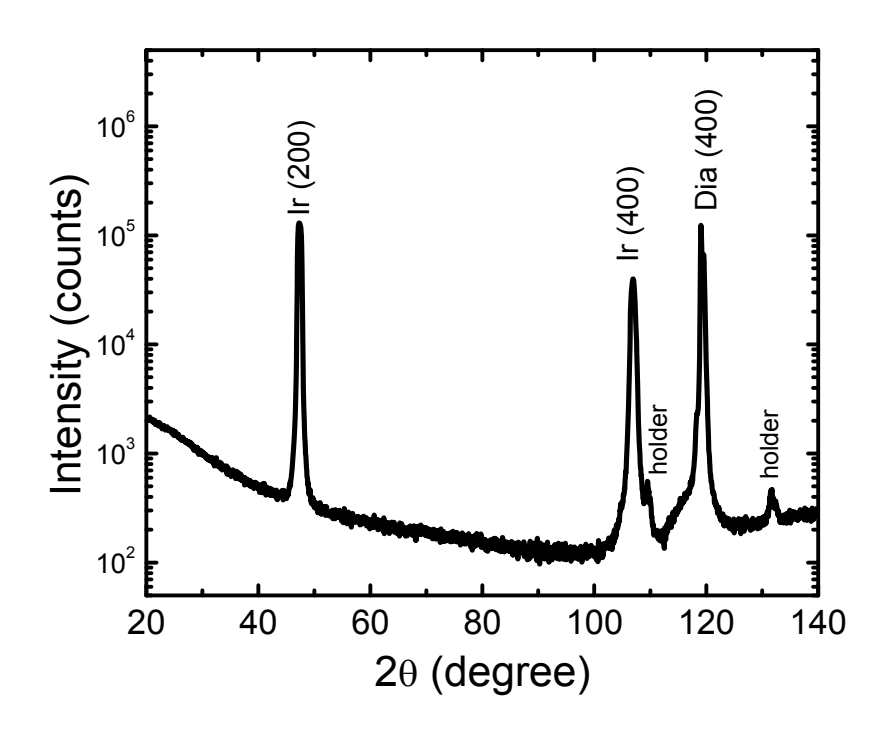


Figure 8.9 XRD diffraction pattern of a piece of 85-µm delaminated diamond.

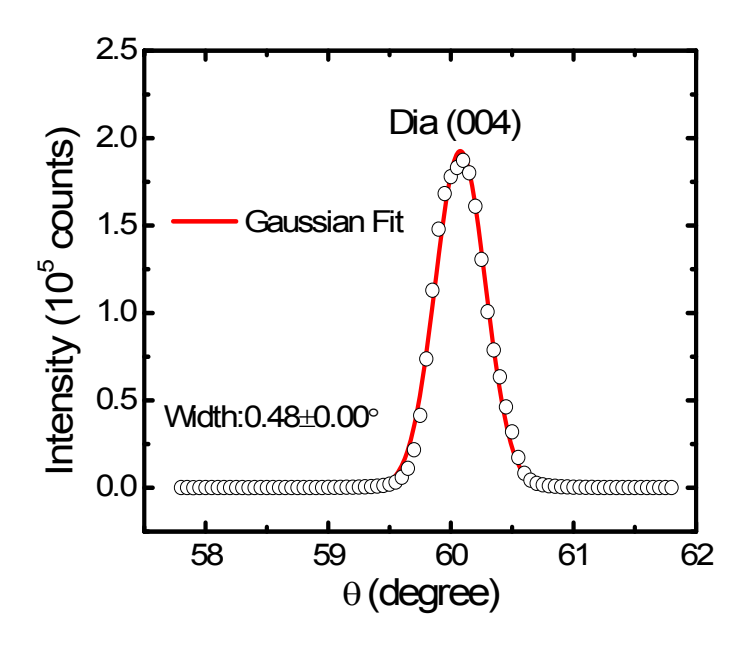


Figure 8.10 X-ray rocking curve of diamond (004) reflection with Gaussian fit.

x-ray absorption lengths in diamond, mentioned in Chapter 8.4. As diamond is grown even thicker, it is found that the XRD linewidth continues to decrease. For 85-µm thick diamond, the linewidth of XRD rocking curve FWHM is reduced to 0.48°, Figure 8.10.

Raman spectra of thick diamond samples were collected in a micro-Raman spectrometer operated in backscattering geometry as described in Chapter 3.4.2. Spectra taken from (001) and (110) faces obeyed selection rules, Chapter 3.4.1. With the high-resolution spectrometer grating, the instrumental resolution is 2 cm⁻¹. Therefore all spectra shown here should be deconvolved with the instrumental resolution function. Figure 8.11 compares the Raman spectra of all thick diamond samples with a Type IIa natural diamond. All of the Raman frequencies of delaminated thick samples appear near 1332.4 cm⁻¹, indicative of a relatively small internal stress in each thick diamond sample. Assuming a biaxial stress in (001), it is estimated at 0.1-0.4 GPa.³⁵

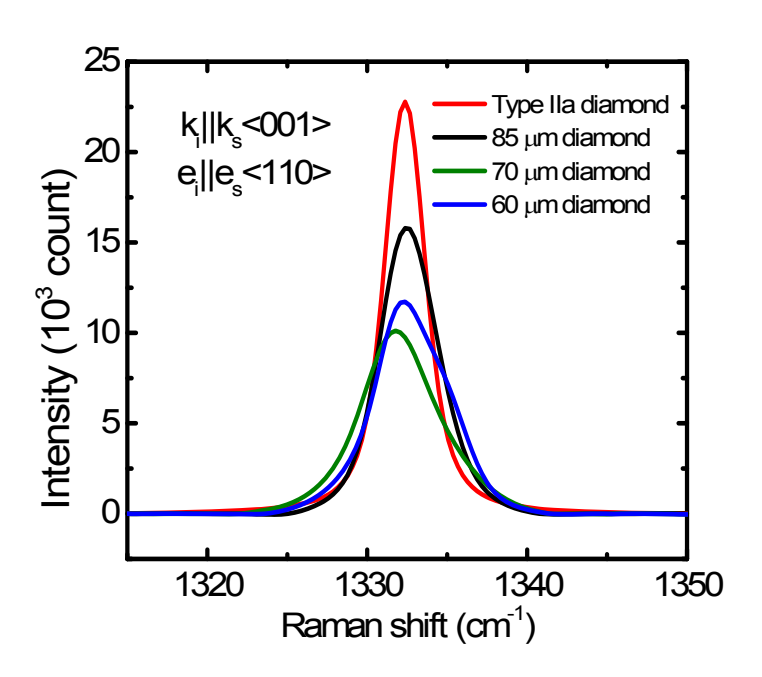


Figure 8.11 Raman spectra of IIa natural diamond and thick heteroepitaxial diamonds. The peak center and linewidth of natural diamond are at 1332 cm⁻¹ and 1.65 cm⁻¹, respectively.

Since the thermally-induced stress is removed when the diamond film delaminates from the substrate, the intrinsic stress in the thick diamond film should be negligible. The Raman linewidth of 85-μm diamond is only 1 cm⁻¹ larger than that of natural diamond, but for 70-μm and 60-μm diamond it is larger by 2-3 cm⁻¹.

Raman spectra were also collected from a diamond (110) surface of the 85-µm delaminated diamond with scans in the [001] direction. Figure 8.12 clearly shows that the stress starts to relax at a 20 µm thickness. Below 20 µm thickness, the intrinsic stress is compressive, approximately 0.6 GPa. The Raman linewidth of the initial layer was greater than 9 cm⁻¹, but decreases rapidly as the film thickens. Therefore, a diamond film thicker than 30 µm is essentially unstressed.

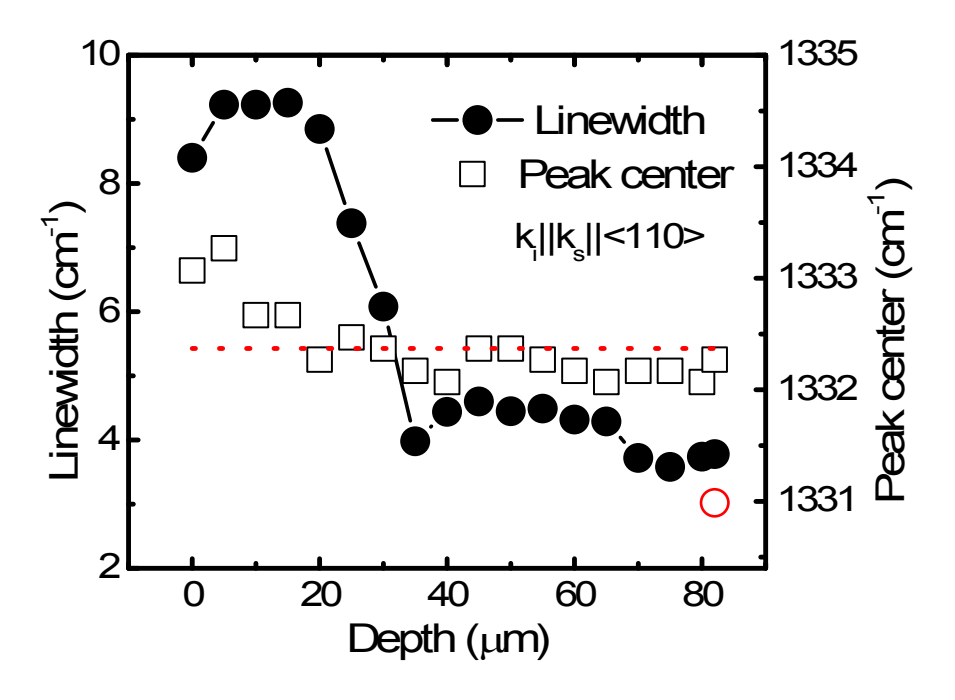


Figure 8.12 Raman linewidth and frequency vs. thickness of a 85-μm diamond sample. The linewidth decreases with thickness and the stress is largely relaxed after 30 μm.

9. Chapter 9 Diamond heteroepitaxial lateral overgrowth

Three different methods of diamond ELO were attempted with the goal of improving the structural quality of heteroepitaxial CVD diamond. The two methods described in Chapters 9.1 and 9.2 both start from a thin heteroepitaxially grown diamond film on an Ir substrate and use a Au masking layer. In the first process, the Au mask functions as a growth mask whereas in the second process it acts as an etch mask. In the third method, described in Chapter 9.3, the starting point is the epitaxial Ir (001) surface. A layer of SiO₂ is overlaid as a biasing and growth mask. Most of the present results were obtained with the first process, which has proven quite effective in producing high-quality single crystal films of (001) diamond up to 0.2 mm thickness and 8 mm in diameter. With further effort, the other two methods could also prove to be feasible routes to realize improved diamond.

9.1 Au-masked Diamond ELO

The basic ELO idea is shown in Figure 9.1 as applied to diamond. A coalesced heteroepitaxial diamond (001) thin film, as described in Chapter 8.5, serves as the starting point. Standard photolithography is used to pattern Au stripes on the diamond surface. Diamond then is grown through the stripe apertures, eventually overgrowing the masked areas laterally. Gold was chosen as the masking material for several reasons: (1) a relatively high melting temperature, 1064 °C, (2) compatibility with photolithographic processes, (3) ease of chemical etching, (4) deposition by thermal evaporation at room temperature, and (5) resistance to carbide formation.

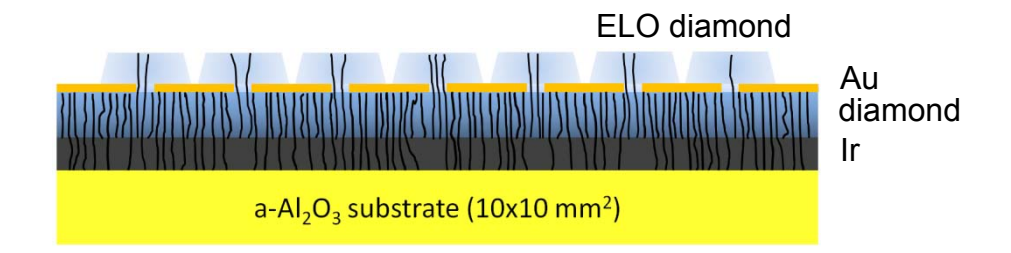


Figure 9.1 Illustration of Au-masked diamond ELO (not to scale). The vertical wavy lines depict threading dislocations which are partially restricted in the diamond overlayer.

9.1.1 Photolithography on diamond

The photolithographic process is illustrated in Figure 9.2. The substrate surface is a 550 nm thick heteroepitaxial diamond film, grown on a 10×10 mm² Ir (001)/a-ALO substrate. Growth conditions are described in Chapter 8.5. The heteroepitaxial diamond covers an 8 mm diameter circular region in the center of the substrate. Lithography proceeded as follows:

- (1) A 300-nm thick lift-off resist (Microchem LOR 5B) was spin-coated at 3000 rpm for 35 sec directly onto the diamond substrate, then baked at 185 °C on a hot plate for 15 min.
- (2) A 1.3 μm-thick positive photoresist (PR) layer (Microposit S1813) was spin-coated onto the LOR surface at 5000 rpm for 35 sec, then baked in an oven at 95 °C for 40 min.
- (3) The PR was exposed to the UV light in an AB-M mask aligner through a photomask for 9 sec.
- (4) The exposed PR was developed with Microposit MF-319 for 28 sec followed by rinsing in flowing DI water and N₂ gas drying. The profile of the diamond substrate at this stage is shown in Figure 9.2(a).

- (5) To remove any PR residues remaining in open channels, the substrate was lightly cleaned in an oxygen plasma etcher at 500 mTorr and 100W for 3 min.
- (6) A 85-nm thick Au layer, or Au (85 nm)/Ti (3 nm) bilayer, was thermally evaporated onto the PR patterned diamond substrate, Figure 9.2(b). It was found that the first Ti layer improved the adhesion of Au to diamond. During evaporation, a Cu foil mask with an aperture of 7 mm diameter covered the diamond substrate to confine Au to the central diamond region.
- (7) To lift off the Au (or Au/Ti) on the remaining PR bilayer, the substrate was bathed in PG remover (Microchem). The lift-off process was initiated in a beaker at 80 °C for 1-2h, then

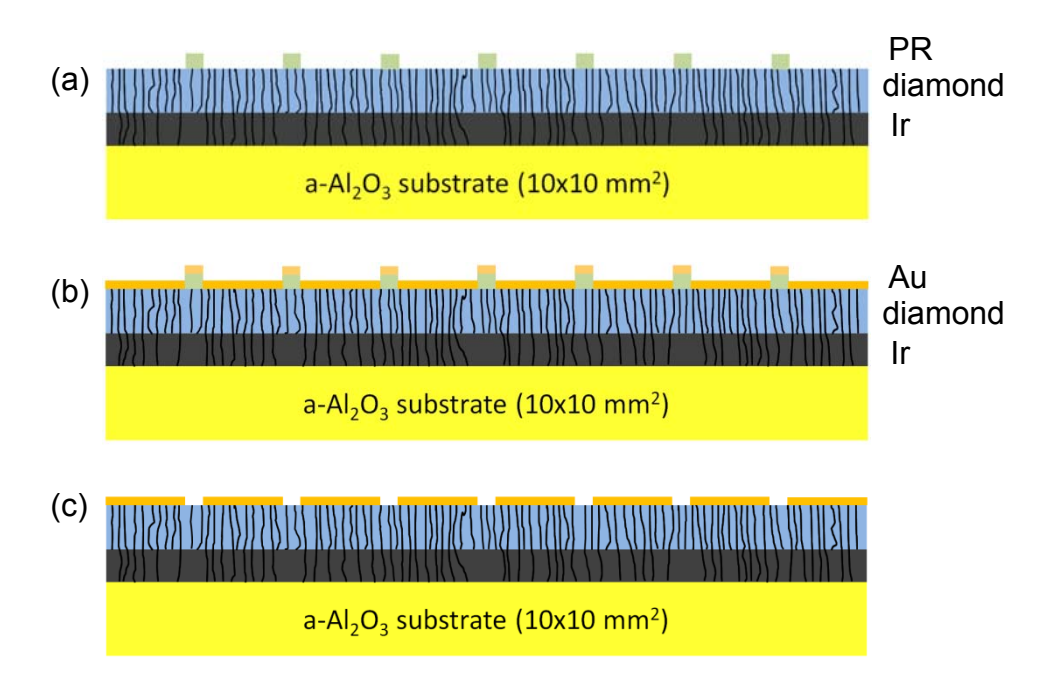


Figure 9.2 Schematic of sample preparation for Au-masked diamond ELO: (a) patterned diamond substrate after PR exposure and development; (b) substrate after Au evaporation; and (c) completed substrate after Au lift-off.

the beaker was left overnight at room temperature. The Au layer then easily floated off the diamond surface with a gentle shaking of the beaker the following morning. Figure 9.2(c) illustrates the diamond substrate after Au lift-off.

- (8) The sample was cleaned again to remove PR and Au residues. To remove LOR residues, the sample was heated at 80 °C again for 20 min in PG remover. To dissolve the PG remover on the surface, the sample was transferred to acetone and heated at 80 °C for another 20 min, followed by an IPA bath at the same temperature and duration. At the beginning of each step, the sample was gently ultrasonicated for 30 sec to improve the homogeneous dissolution. The sample was then rinsed in flowing DI water to remove any residual Au particles, then blown dry.
- (9) Finally, the Au-patterned diamond substrate was plasma-etched in oxygen at 500 mTorr and 300W for 9 min to prepare the diamond surface for regrowth.

Two types of photomasks were used in step (3): a 5-inch and a 4-inch diameter chrome mask. Both were supplied by Photo Sciences Inc. (PSI). The 5-inch mask consisted of a single stripe pattern with periodicity 20 μ m and 3.5 μ m apertures. The 4-inch mask had two separate sections of stripes: one section with periodicity 12 μ m and 8 μ m apertures and the other section with periodicity 16 μ m and 12 μ m apertures. The apertures are the transparent regions of the mask that exposes the PR; they ultimately become the Au stripes that mask the diamond.

Due to the radial thickness variation of the diamond film, the photomask did not uniformly contact the PR surface. The central high point resulted in a series of circular fringes on the PR surface when viewed in the mask aligner. The stripe direction of the photomask was aligned parallel to an edge of the a-ALO substrate, corresponding to a <110> diamond direction, or at 45° to an edge, corresponding to a <100> diamond direction. After developing, the PR stripe

edges were usually rounded due to the partial contact between photomask and PR. A rounded profile makes lift-off difficult because the Au layer covers the PR flats and edges. It is then difficult for the Au layer to break off evenly at the PR edges when the PR is dissolved during lift-off. For improved lift-off success, it is advantageous to form an undercut edge; this is the function of the LOR underlay. As a result the PG remover was able to easily dissolve LOR stripes from the bottom. Examples of diamond surfaces patterned by 4-μm or 8-μm wide Au stripes are shown in Figure 9.3.

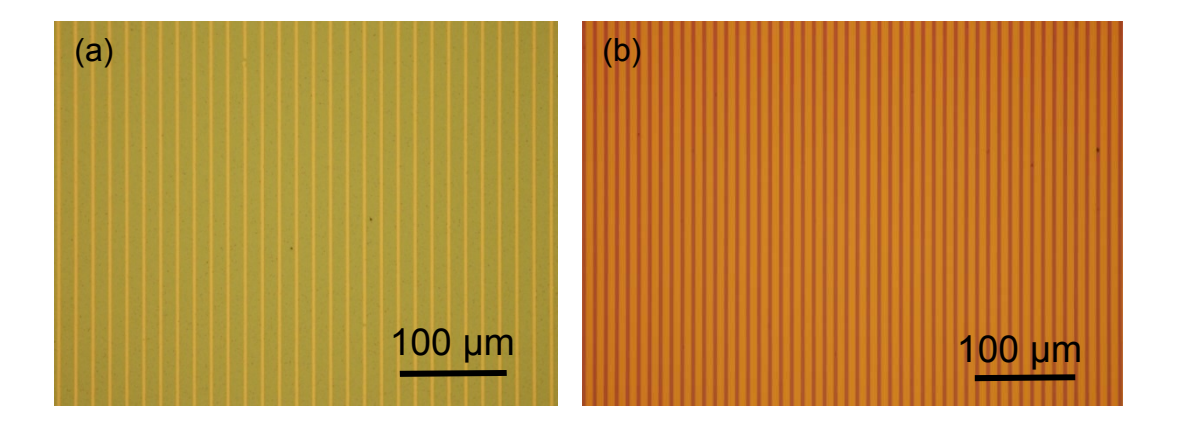


Figure 9.3 Optical images of patterned diamond substrates with (a) 4- μ m wide Au stripes with 16 μ m gaps and (b) 8- μ m wide Au stripes with 4 μ m gaps. In both cases, the stripes are parallel to the diamond <110> direction.

9.1.2 Diamond regrowth

The initial experiments on regrowth were performed in the CVD reactor. Those substrates were patterned with 4 µm wide Au stripes with 16 µm gaps using a mask designed for a different purpose. Since better dislocation masking is performed with small gaps, a photomask with 8 µm stripes separated by 4 µm apertures was designed later. Lateral overgrowth with the wider Au stripes was carried out in the AsTex reactor. During regrowth, the following issues are of concern: (1) whether the Au mask remains intact until overgrown by diamond; (2) whether diamond nucleates and grows on the Au surface; and (3) whether there is carbide formation on the Au. Regrowth conditions for a number of trials are listed in Table 9.1.

Table 9.1 Growth conditions of ELO diamond with different initial thicknesses. Growth with two steps is indicated by x/y.

Stripe width/ periodicity (µm)	Pressure (Torr)	Power (kW)	CH ₄ (%)	Growth temperature (°C)	Vertical growth rate (µm/h)	Stripe direction (diamond axes)	Final thickness (µm)
4/20	26	1.5	3	750^{\dagger}	0.4	<100>	2
8/12	58	0.51/0.53	2	740/750*	0.7/0.8	<110>	10
4/20	24	1.94	3	750^{\dagger}	0.4	<110>	30
4/20	45/60	0.7	4	710/800*	0.25/1	<110>	75
8/12	58/60	0.50/0.55	2/3	730/750*	1/1.5	<110>	190

[†]Growth in CVD reactor, temperature measured on the Mo cap. (cf. Chapter 4.3.1)

^{*}Growth in AsTex rector, temperature measured on the Ir surface. (cf. Chapter 4.3.2)

9.1.2.1 Early stage of coalescence

Diamond regrowth conditions with the Au mask did not differ significantly from non-masked diamond growth with one exception. Growth temperatures were generally 50 to 60 °C lower initially to inhibit Au delamination and sputtering in the microwave plasma. Excessive Au sputtering is believed to enhance twin formation on the growing diamond stripe sidewalls.

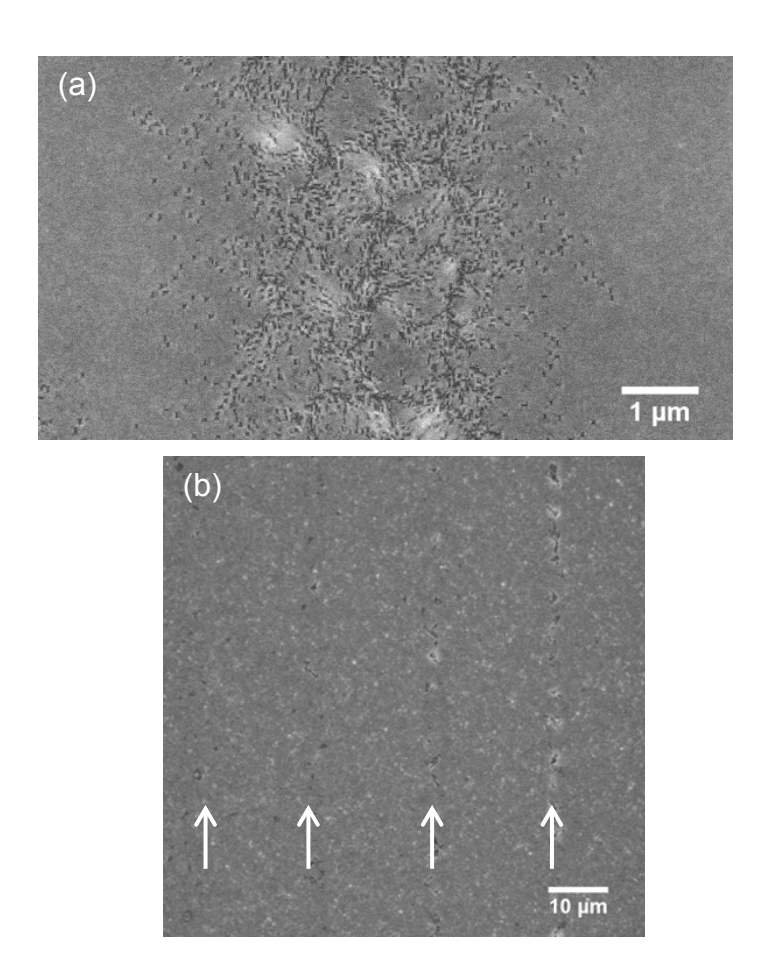


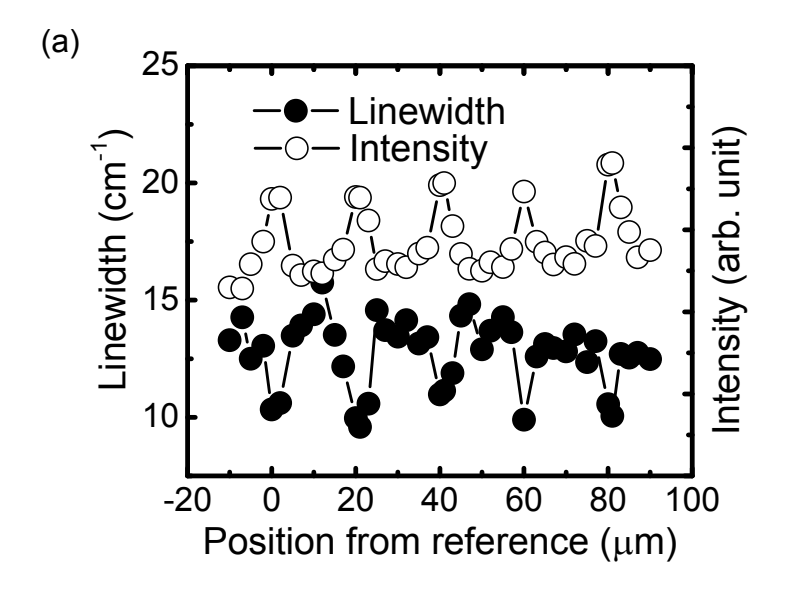
Figure 9.4 Plan-view SEM images of (a) 10-μm thick ELO diamond with 8-μm wide Au stripes centered on the non-overgrown region. The pits are the terminations of dislocations at the top surface. (b) 2-μm thick ELO diamond with 4-μm wide Au stripes, just prior to diamond coalescence. The white arrows indicate the position of the Au stripes.

During regrowth, the lateral diamond growth rate was only weakly dependent on growth direction. The time for coalescence to occur is proportional to the Au stripe width. Thus, the film thickness at coalescence will scale roughly with the stripe width. Substrates with 4 µm Au stripes were observed to coalesce at 2 µm thickness, but for 8 µm Au stripes they coalesced at about 10 µm thickness. The qualitative success of lateral overgrowth can easily be seen by inspection of Figure 9.4(a) which is an SEM image of a 10 µm thick film at coalescence. The central region is above the mask aperture where diamond grows unimpeded from the substrate. The dark region indicates surface roughness, brought about by the high density of dislocations that terminate at the top surface. The adjacent regions are much smoother and have few visible dislocation terminations. These are the Au-masked regions where lateral overgrowth has occurred.

In Figure 9.4(b) with 4 μ m Au stripes, coalescence has just occurred at a diamond regrowth thickness of 2 μ m. Here the thin film does not allow much SEM contrast between masked and non-masked regions. More quantitative methods to analyze diamond structural perfection must therefore be used. More specifically, the use of spatially-resolved micro-Raman scattering to probe the lateral variation of the regrown diamond is now described.

Figure 9.5 shows Raman linewidths and corresponding Raman intensities for the two aforementioned overgrown diamond samples. Oscillations of these quantities occur with the same periodicity as the Au stripes. The minimum Raman linewidths and maximum intensities occur just above the Au stripes in the laterally overgrown regions. The linewidth oscillated with amplitude of 30% for the 2- μ m thick ELO diamond with 4 μ m Au stripes. For the 10- μ m thick ELO diamond with 8- μ m wide Au stripes, the oscillation amplitude increased to 60%. More significantly, the value of the linewidth above the Au stripes was reduced by a factor of two for the thicker overgrown diamond. These results are consistent with dislocation confinement to the

non-overgrown regions. Here the dislocations produce random internal strains that broaden the distribution of the diamond vibrational frequencies detected by the Raman experiments.



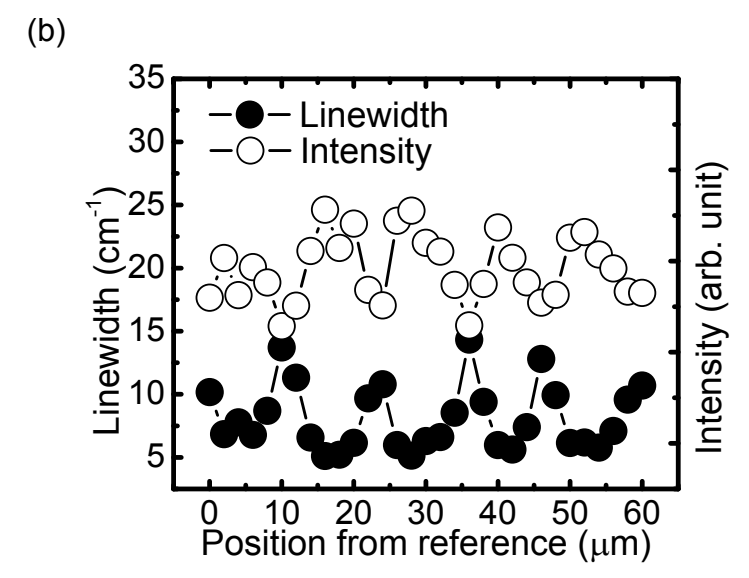


Figure 9.5 Spatial variations of the Raman linewidth and intensity for a (a) 2-μm thick ELO diamond with 4-μm wide Au stripes and (b) 10-μm thick ELO diamond with 8-μm wide Au stripes. In both cases the diamond has not detached from the substrate. The linewidth is minimized at the overgrown region above the Au stripe.

Useful information about the mean stress in the diamond film is contained in the Raman line center position. Since the Raman frequency is stress-sensitive, Appendix, it can be used to measure the static stress in the film. Two independent types of stress exist in the diamond film, designated as *internal* stress and *thermally-induced* stress. The film itself contains *internal* stress as a result of deviations from crystalline perfection, e.g., dislocations, vacancies, and impurities. *Thermally-induced* stress arises when the film and substrate have mismatched thermal expansivities and are cooled from growth temperature. It will be primarily a biaxial stress, with equal components in the plane of the film. Sapphire has a larger thermal expansivity than diamond (see Appendix) so that cooling from the growth temperature at 750 °C introduces a biaxial compressive stress in the diamond. Provided the film is much thinner than the substrate and that there is no slip at the interface, the theoretical thermal stress in diamond can be calculated from elasticity theory by

$$\sigma_d = \Delta \varepsilon E_d / (1 - \nu_d)$$
 9.1¹⁵⁶

where σ is the biaxial stress, $\Delta \varepsilon$ the thermal strain, E is Young's modulus and v is Poisson's ratio. The thermal strain is given by

$$\Delta \varepsilon = \int_{T_1}^{T_2} [\propto_d (T) - \propto_s (T)] dT$$
9.2

where α is the thermal expansivity of diamond (*d*) and substrate (*s*), T_2 is the growth temperature and T_1 is usually room temperature. Evaluation of Eq. 9.1 gives σ_d = -4.55 GPa for diamond on aplane sapphire.

This prediction can be tested by using the Raman data in Figure 9.6 for the 2-µm thick diamond film at coalescence. The film was grown at 750 °C and cooled to 25 °C at which time it

was found that the diamond film had cracked into large pieces that partially delaminated from the substrate. The thin Ir film always adhered to the diamond, not to the ALO. However, some parts of the film remained attached to the substrate, referred to as "non-delaminated". Figure 9.6 shows that the Raman center frequency is independent of lateral position but undergoes a large positive shift of +3 cm⁻¹ in the non-delaminated diamond. The delaminated film was essentially unchanged from the reference Raman peak position of unstressed Type IIa natural diamond at 1332.4 cm⁻¹, indicating the near-absence of thermal and internal stress. The shift for the adhering film corresponds to a biaxial compressive stress of -1.8 GPa. This is only 40% of the calculated value for the thermal stress. The low value leads us to infer that the interfaces are not rigidly connected, violating a validity condition for Eq. 9.1.

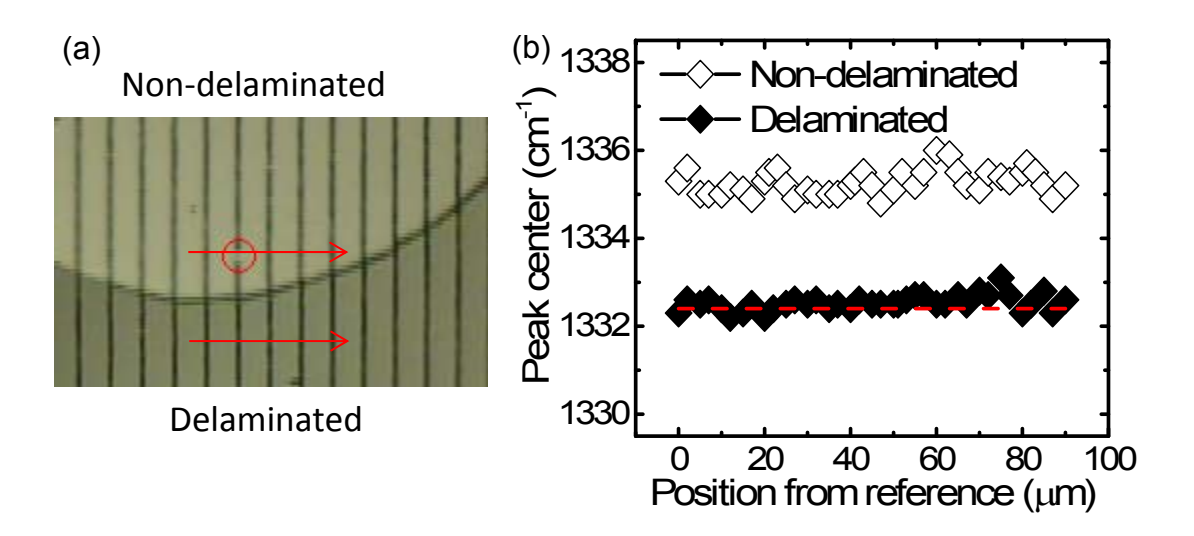


Figure 9.6 (a) Photograph of diamond (001) surface with both delaminated and non-delaminated regions and (b) comparison of the adherent and delaminated regions on 2-μm thick ELO diamond with 4-μm wide Au stripes. The delaminated film has the unstressed diamond Raman frequency whereas the strongly attached film shows large compressive stress. The red dashed line represents the unstressed diamond frequency at 1332.4 cm⁻¹. The polarizations of incident and scattered laser beams were parallel to <110>.

The low stress is most likely a consequence of the Au masking stripes, since Au is very ductile and easily deformed. It allows the overgrown diamond to slip with respect to its substrate. As we discuss below for a thicker diamond film, it appears that the Au does not adhere well to the diamond after growth and cool-down. Therefore, this Au ELO process not only improves diamond structural quality but acts to relieve thermal stress build-up.

9.1.2.2 Intermediate thickness diamond films

Figure 9.7 shows SEM images of a slab of 30 μm thick ELO diamond grown with 4 μm wide Au stripes. Figure 9.7(a) was taken at a tilt angle to demonstrate the flat and smooth (001) diamond top surface and two rough {110} fracture surfaces. Note that the Au stripe edges are visible at the lower edge of the crystal. Figure 9.7(b), at higher magnification, was taken without tilt near a Au stripe buried under the ELO diamond layer. The Au stripe appears to be intact following diamond growth but there is some evidence for deformation. Just above the center of the stripe is a triangular void. This is the coalescence region of the diamond film, i.e., the point at which diamond overgrew the mask from two sides and shadows the plasma from the substrate. The diamond does not wet or bond to the Au since there is a gap along most of the Au stripe edge. The void and gap may help to minimize interfacial tension in diamond. In ELO grown GaN, strong contact between coalescing regions has been shown to lead to growth-axis tilting ¹⁴⁸ so that weak contact is advantageous.

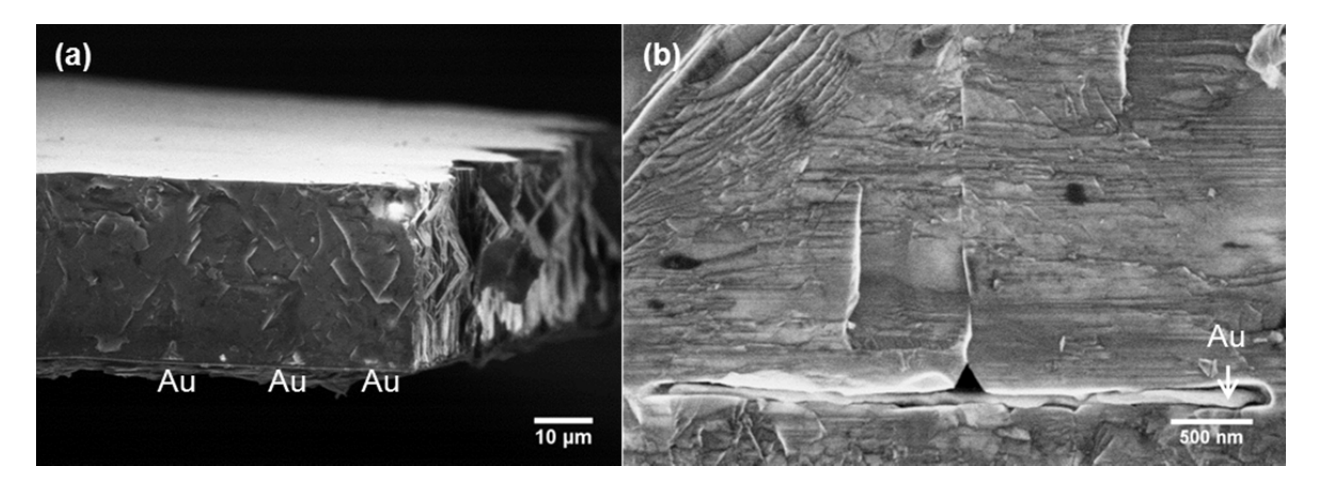


Figure 9.7 SEM images of a 30-μm thick ELO diamond grown with 4-μm wide Au stripes. (a) Tilted image, the top surface is the (001) face and the sides are {110} fracture surfaces. The Au stripes are visible in the lower part of the crystal. (b) Expanded {110} fracture surface at the region near the Au stripe. The diamond only weakly contacts the Au stripe during overgrowth and forms a void at the top surface of the gold.

9.1.2.3 Thick diamond growth

Diamond films were grown using Au-masked ELO to 75 and 190 µm thicknesses with 8-µm wide Au stripes and 4 µm apertures. Figure 9.8 shows an optical micrograph of the 190-µm thick diamond with the objective focused on the Au stripes through the diamond overlayer. The stripes are intact, continuous, and appear to be undamaged during growth. The image further demonstrates the feasibility of using 8-µm wide Au stripes as a mask for diamond under the present growth conditions.

Examination of films with SEM is restricted to the near surface owing to the relatively shallow penetration of keV electrons into diamond. In the 75-µm thick diamond film shown in Figure 9.9(a) there is some evidence for surface roughness arising from dislocation etch pits.

However, at both 75 μ m and 190 μ m thicknesses, Figure 9.9, there are no longer any periodic surface features that have resulted from ELO growth. It is also likely that the threading dislocations eventually bend laterally so that the spatial distribution of dislocations at the surface is fairly uniform. We note that Raman scattering shows no periodic spatial variation in films once they are thicker than 30 μ m.

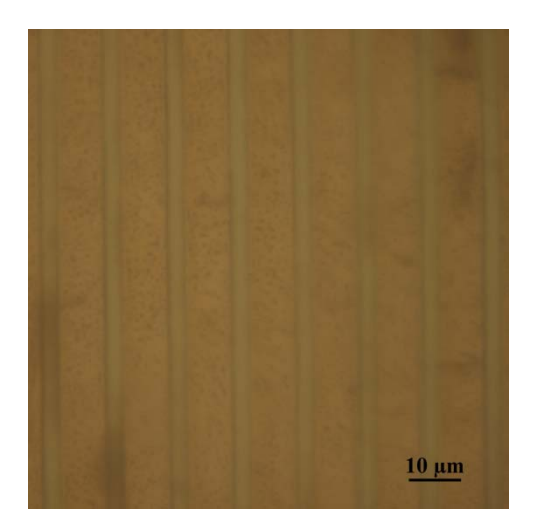


Figure 9.8 Optical image of Au stripes taken through a 190-μm thick ELO diamond overlayer. The 8-μm wide stripes are oriented parallel to the <110> diamond direction.

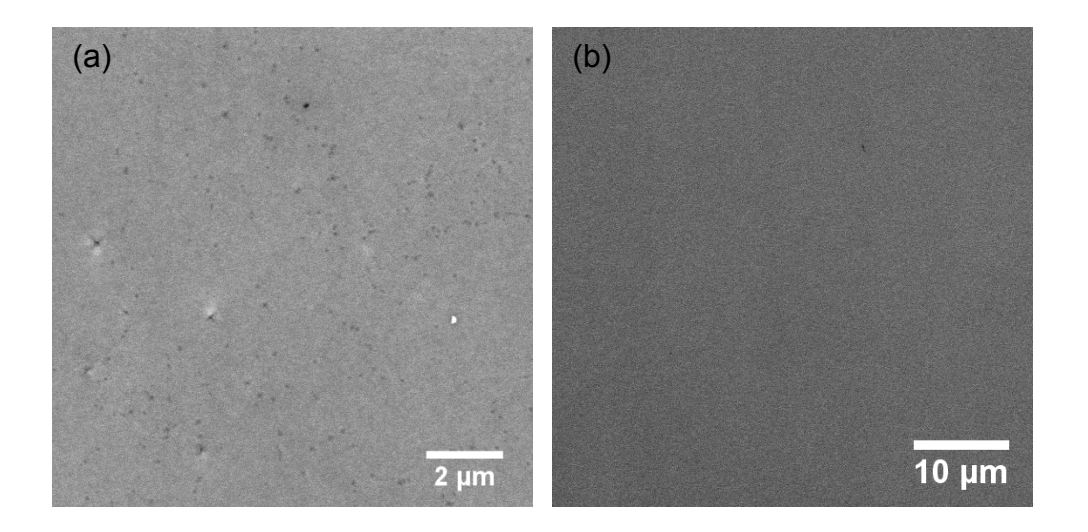


Figure 9.9 Plan-view SEM images of (a) 75-μm thick ELO diamond with 4-μm wide Au stripes and (b) 190-μm thick ELO diamond with 8-μm wide Au stripes.

The 190-μm thick ELO diamond film, noted above, did not catastrophically crack or delaminate from the a-ALO substrate after cooling to room temperature. We noted the appearance of small cleavage cracks near the ALO substrate which did not propagate to the surface. This suggests that the internal stress in this diamond sample is small. A lateral Raman scan, with the laser focused on the diamond surface, across the 8 mm diameter of the crystal is shown in Figure 9.10. The line center shows small fluctuations about 1332.4 cm⁻¹, corresponding to a total stress of 0.00±0.16 GPa. This indicates the maximum stress (the upper and lower uncertainties of the fit) is at least an order of magnitude lower than the thermal stress in a 2 μm diamond film, Chapter 9.1.2.1. It is not clear how much of the stress relaxation can be attributed to the ELO growth. In the future, a comparison should be made between ELO and non-ELO diamond grown under the same conditions to the same thickness.

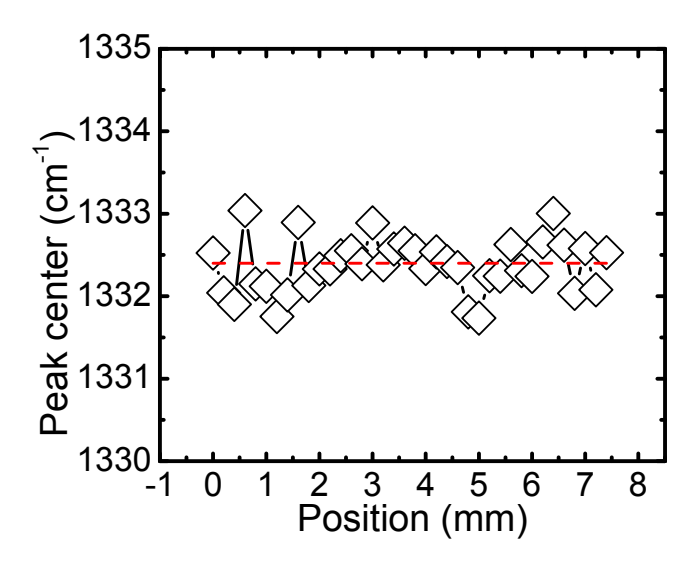


Figure 9.10 Raman center frequency of 190-μm thick ELO diamond with 8-μm wide Au stripes. The scan covers 8 mm, the diameter of the entire diamond crystal. Very low stress is apparent from the small Raman shift, 1332.4±0.26 cm⁻¹.

Even with the 100x Raman microscope objective focused at the diamond surface, Raman signals from well below the surface may contribute to the total intensity. This is because the spectrometer is not truly confocal; it lacks a pin-hole to collimate the scattered light. This is problematic for thick crystals, since the Raman signal will be averaged over 50 µm or more. To obtain reliable Raman data as a function of distance from the top surface, crystals were rotated by 90 degrees so that the beam was scanned parallel to the growth, or z-axis. Figure 9.11 shows results for a z-scan for the 75-µm thick ELO diamond with 4-µm wide Au stripes. In Figure 9.11(a), it can be seen that the Raman linewidth decreases more or less continuously as the film thickens. Figure 9.11(b) indicates that the crystal grows under tensile stress while it is largely relaxed at the surface. The oscillations may be correlated with small variations in the growth conditions. The linewidth at the surface is about 1 cm⁻¹ larger than the natural diamond linewidth

of 1.65 cm⁻¹. We expect that the linewidth will continue to decrease as crystals are grown to greater thicknesses.

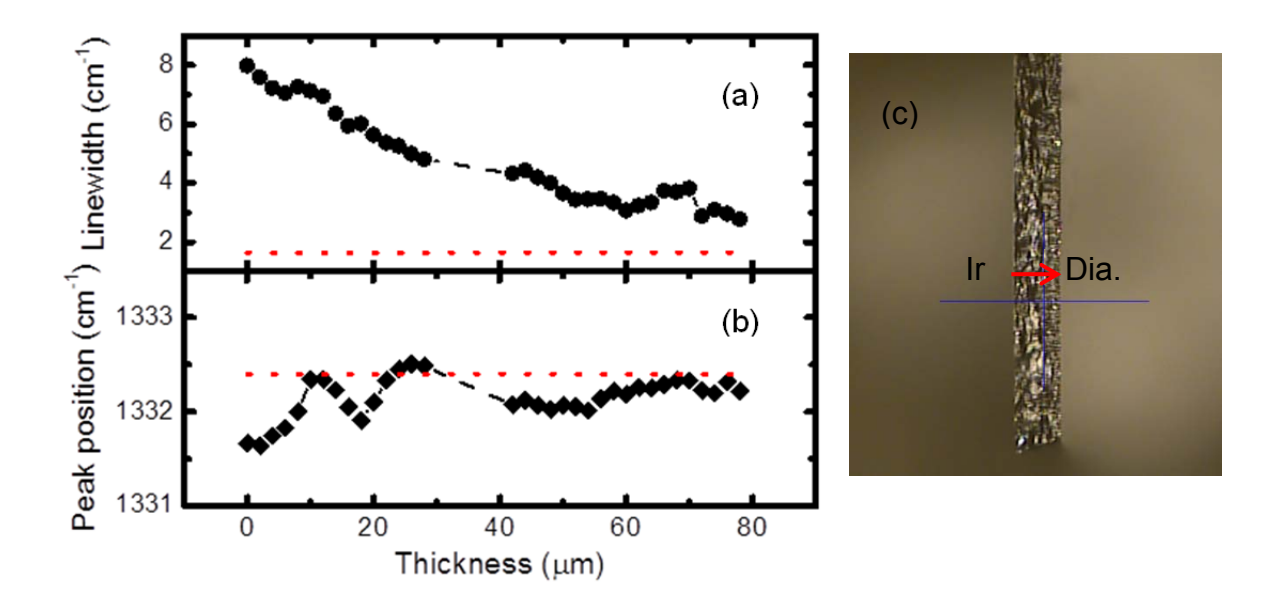


Figure 9.11 (a) Raman linewidth and (b) Raman frequency vs. thickness of a 75-μm thick ELO diamond with 4-μm wide Au stripes. The linewidth decreases with thickness and the stress is mostly relaxed on the top surface. (c) Photograph of diamond {110} surface. The arrow indicates the scan direction, along [001]_{dia}.

9.2 PENDEO for Diamond ELO

The idea of PENDEO lateral overgrowth, previously successful for GaN, see Chapter 6.3.3, was adapted to diamond. Although it also utilized a Au stripe mask, in this case the Au is used as an *etch* mask, unlike the previous method with Au used as a *growth* mask. The starting point is a 550-nm thick heteroepitaxial diamond film, grown under the conditions described in Chapter 8.5. The surface is masked with Au stripes, then plasma etched to form a parallel array of trenches, the Au removed and the diamond stripes then regrown until they coalesce. A part of process of diamond regrowth after etching is illustrated in Figure 9.12.

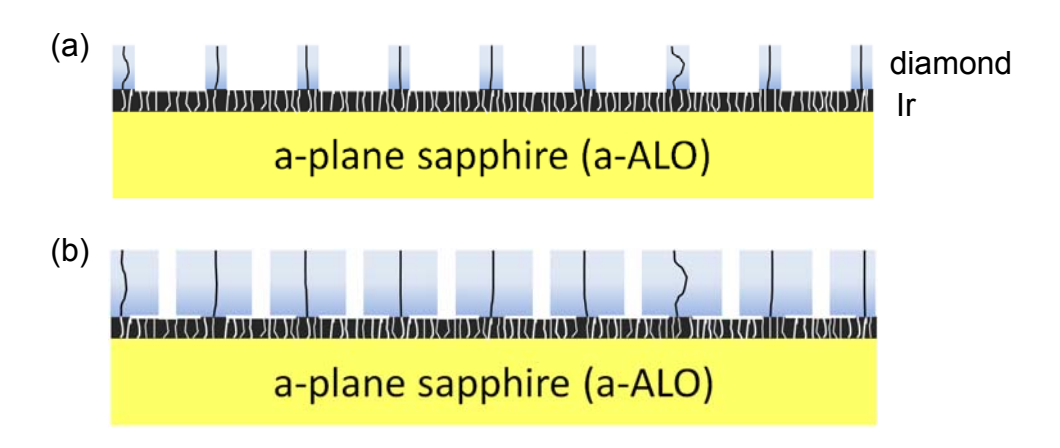


Figure 9.12 Schematic of PENDEO process during diamond growth.

Diamond is readily etched in oxygen or oxygen-containing gas mixtures by electron cyclotron resonance (ECR), inductively coupled plasma (ICP) or reactive-ion etching (RIE) systems. Masking materials previously studied are $Al_1^{157,158,159,160,161}$ $Au_1^{162,163,164,165}$ Ti_1^{165} $SiO_2^{165,166,167,168}$ and $Si_3N_4^{165}$ Since no commercial plasma etcher was available, we attempted to etch the diamond substrate in the CVD reactor at a relatively high temperature, at 500-600 °C, in

a hydrogen plasma. An evaporated Au layer was used as the etch mask. As we describe below, the idea is promising but only a proof-of-principle was demonstrated.

9.2.1 Substrate preparation

The photolithographic process for substrate preparation is illustrated in Figure 9.13. The diamond substrate was described in Chapter 9.1.1. Surface patterning proceeded as follows.

- (1) A 1.3 μm-thick positive PR (Microposit S1813) was spin coated onto the diamond surface at 5000 rpm for 35 sec diamond substrate covered with the PR layer, then baked in an oven at 95 °C for 40 min.
- (2) The baked PR surface was exposed by the UV light through a photomask for 9 sec.
- (3) The exposed sample was developed in Microposit 352 for 30 sec followed by rinsing in flowing DI water and N₂ drying. As this point, the diamond surface was patterned by the PR layer as shown in Figure 9.13(a).
- (4) To remove PR residues in open channels, the substrate was cleaned in the oxygen plasma etcher at 500 mTorr and 100W for 3 min.
- (5) As shown in Figure 9.13(b), a 100-nm thick Au layer was deposited by thermal evaporation onto the PR patterned substrate.
- (6) The Au-covered diamond substrate was immersed in acetone at room temperature for 20-30 min. Without a LOR layer, weak ultrasonication was needed to completely lift off the Au-covered PR. Due to the poor Au adhesion, even weak ultrasonication often causes the Au layer to delaminate from the diamond as well. The sample was then soaked in IPA for 10 min. Figure 9.13(c) illustrates the sample cross-section after Au lift-off. A final DI rinse followed.

(7) The Au-patterned diamond substrate was etched in an oxygen plasma etcher at 500 mTorr and 300W for 3 min to completely remove any remaining PR.

A 5 inch diameter PSI chrome stripe mask with a 3.5 μm stripe aperture and 20 μm repeat was used. After lift-off, the diamond (001) surface was covered with 4-μm wide Au stripes in the <110> diamond direction.

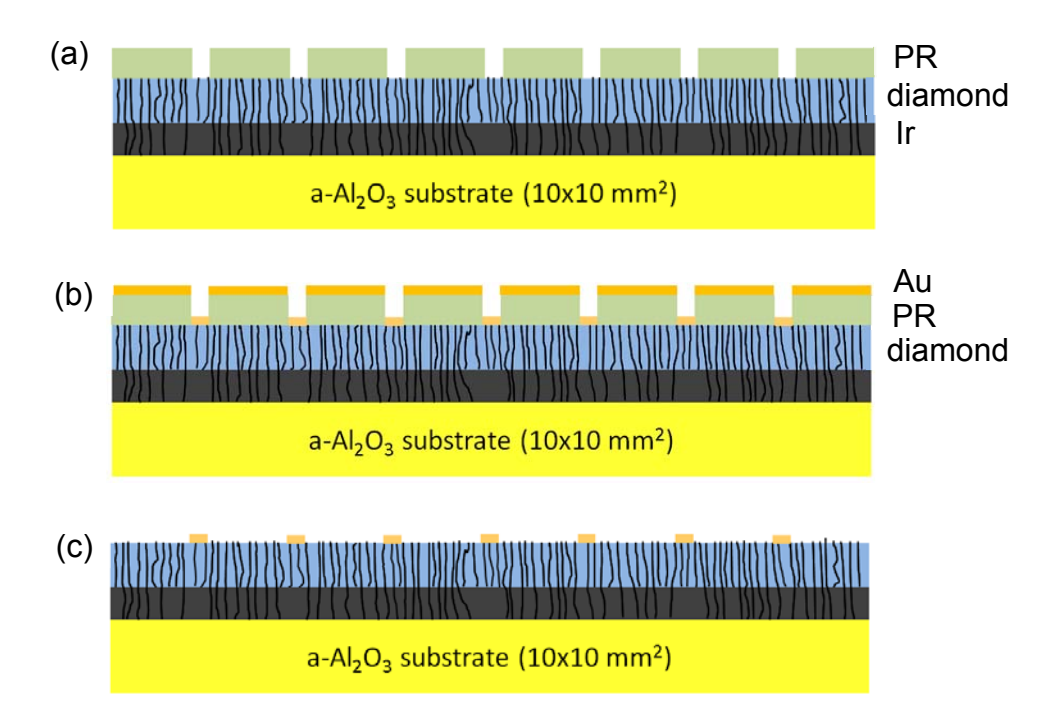


Figure 9.13 Illustration of sample preparation for PENDEO diamond ELO: (a) a 550-nm thick diamond substrate patterned with stripes of PR layer by standard photolithography; (b) Au (100 nm) mask layer thermally evaporated on a diamond substrate; and (c) diamond substrate covered by the Au stripes along the <110> direction. See Figure 9.12 for the two last steps of the process.

9.2.2 Diamond plasma etching

The Au-patterned diamond film was etched using a bias-assisted plasma process in the CVD reactor. Due to the low plasma density, the etching was carried out at moderate process pressure, 1-10 Torr, and temperatures between 500-600 °C. The sample holder geometry for diamond plasma etching is the same as that for BEN, Figure 8.1.

In the etching experiments, we addressed the following issues: (1) stability of the Au mask layer; (2) diamond etching rate in H_2 or dilute O_2/H_2 plasma; (3) selectivity, the thickness ratio of etched diamond to etched Au, in H_2 plasma; (4) Au mask removal following etching; (5) damage to the diamond underlayer; and (6) extent of Au redeposition.

Table 9.2 Conditions of diamond plasma etch in pure H₂.

Sample#	Pressure (Torr)	Power (kW)	Bias voltage (-V)	Bias current (mA)	Bias duration (min)	Note
13-3	18	1.11	133	46-38	5	Au
13-1	18	1.55	150	45-16	30	Au/Ti bilayer

In the first trial, a Au masked diamond substrate was etched in pure H₂ and biased at -133 V for 5 min. During biasing, a reddish glow appeared above the diamond surface, characteristic of the cathode glow of a hydrogen plasma. The bias current started at -46 mA again and decreased to -38 mA gradually. Figure 9.14 shows the steep sidewalls of protected diamond strip, indicative of the highly directional H₂ etching in diamond. In Figure 9.14(b), diamond was only partly etched forming cone-shape artifacts. Kobashi *et al.* found that the cone-shape feature was

etched diamond covered with a thin layer of graphite, ¹⁷⁰ which led to a decreased bias current. After biasing, the Au surface showed damage. This caused some unintentional etching of the masked region, Figure 9.14(b). After etching the Au was readily removed with a fresh aqua regia solution.

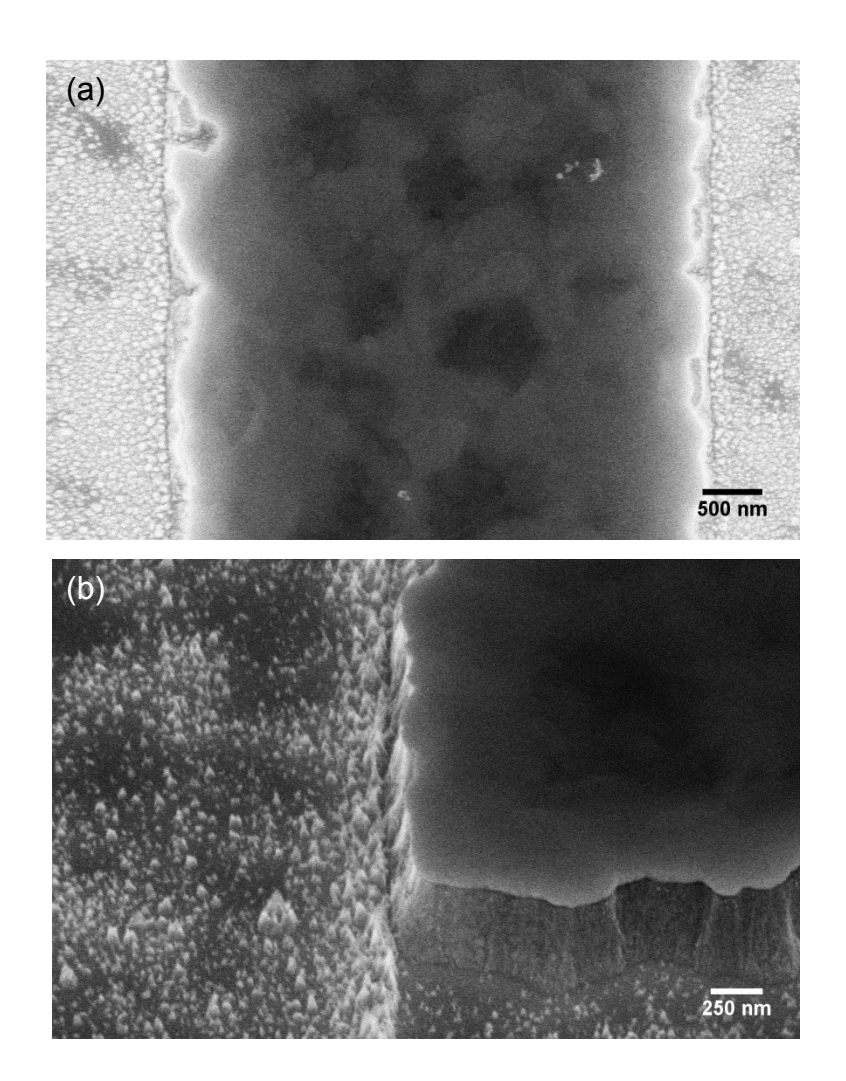


Figure 9.14 (a) Plan-view SEM image of a diamond stripe after etching with Au mask remaining (center). The Au mask shows damage, with holes visible. (b) 45° tilt SEM image at the boundary of a diamond stripe and the etched trench. The Au masked diamond stripe is on right side; the area on the left has been etched. Note the steep sidewalls of the diamond and the cone-like features in the etched area.

The 550 nm diamond substrate was etched by 370 nm, corresponding to an etch rate of 0.8-0.9 µm/h. During bias, the Au layer was also etched by 30-40 nm. Consequently, the selectivity was 11, comparable to the ECR technique. 165 Inadvertent peeling of Au during bias arises from poor Au-diamond adhesion. In the next trial, a 5-nm thick Ti layer was evaporated prior to Au evaporation to improve adhesion. The substrate was biased at -150 Vdc for 30 min. The bias duration and bias voltage were increased to etch more completely. The bias current started at -45 mA and decreased gradually to -16 mA. After biasing the masked regions were all intact and no peeling of the Au layer was observed. The diamond in the apertures was etched to the Ir surface, as shown in Figure 9.15, and no cone-like features on Ir were apparent. The height of the diamond stripe measured from the Ir was about 500 nm in agreement with the diamond thickness. Chemical etching in aqua regia solution left a thin residual layer on the diamond surface that Raman spectroscopy identified as TiC_x. ¹⁷¹ Apparently, the plasma etching temperature is sufficiently high that Ti reacts with carbon to form the carbide, which is relatively impervious to chemical or Ar/O₂ plasma etching. Consequently, the adhesion of Au still remains an issue for this ELO process.

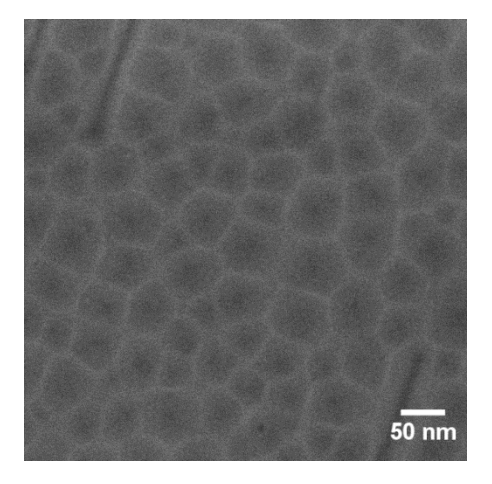


Figure 9.15 Plan-view SEM image of etched area showing the bare Ir surface. Small structures may be Ir coalescence boundaries. No trace of diamond residues is seen.

9.2.3 Regrowth of protected diamond stripes

Regrowth of the etched diamond stripes was carried out under conditions listed in Table 9.3. After 3.5h of growth, diamond stripes grew uniformly by 2 µm. Flat {111} facets formed on the sidewalls, Figure 9.16(a). The cone-like features in the etched region turned into (100) diamond faceted crystallites, Figure 9.16(b). No change in the height of the stripes relative to the aperture was measured, indicating that both regions had the same growth rate.

Table 9.3 Regrowth conditions of sample 13-3 after H₂ plasma etch.

Sample	Pressure (Torr)	Power (kW)	CH ₄ (%)	Growth temperature (°C)	Stripe direction (diamond axis)	Reactor
13-3	35	1.55	1	850	<100>	CVD

In Figure 9.16(a), the surfaces along the edge of diamond stripes, i.e., the overgrown regions are smoother than in the center of non-overgrown region. The different surface roughness is similar to the observation in Figure 9.4(a), suggesting that threading dislocations have a lower density in the overgrown area. Further studies aimed at improving Au adhesion and with better removal of diamond in the trenches are needed. A possible modification is the addition of oxygen to the plasma which should result in faster diamond etch rates with little effect on the Au adhesion. It would also be necessary to optimize the vertical and horizontal diamond growth rates so that overgrowth of the channels occurs before diamond nucleates in these regions. Nevertheless, this method appears to improve the diamond quality and should be investigated.

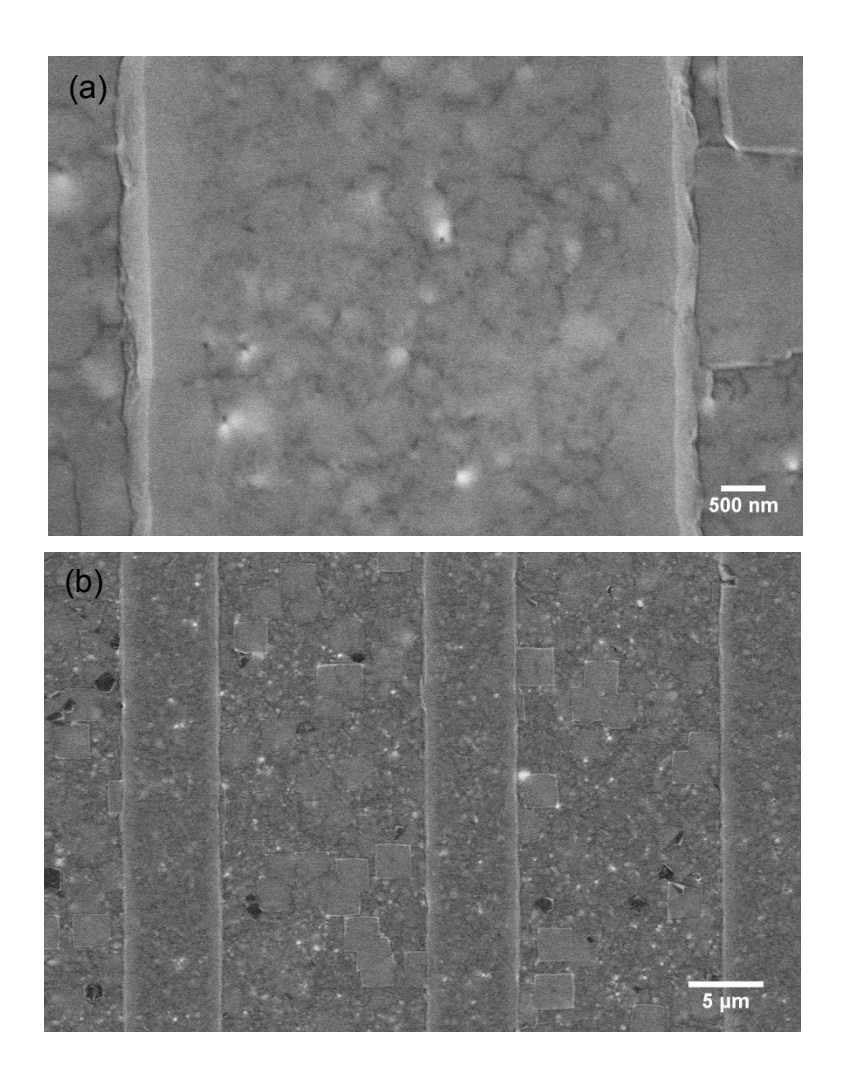


Figure 9.16 Plan-view SEM images of the plasma-etched diamond substrate after regrowth. (a) A diamond stripe, showing the formation of {111} facets on the side walls. (b) Diamond stripes and etched areas shown at lower magnification. The diamond grew in the etched areas and formed oriented crystallites after 3h.

9.3 Diamond ELO with SiO₂ mask

In this approach, SiO₂ was used as a growth mask. In contrast to the method that used Au to mask a previously grown thin diamond substrate, the SiO₂ masks a bare Ir epilayer. After exposure to the BEN process, it was anticipated that diamond would nucleate and grow from exposed Ir stripes, eventually overgrowing the SiO₂ mask, as visualized in Figure 9.17. Amorphous SiO₂ is a common masking material frequently used in III-V semiconductor ELO, see Chapter 6. SiO₂ has several advantages, particularly its high softening temperature and its etching properties. The issues to be addressed in this process are similar to those considered earlier. These are the relative etch rates of SiO₂ to diamond and whether diamond nucleates on SiO₂. We found that exposure of the SiO₂ to the intense BEN conditions is problematic. Although this method may prove viable, at the present time this method appears the least favorable approach.



Figure 9.17 Illustration of diamond ELO with SiO₂ mask.

9.3.1 Substrate preparation

Figure 9.18 illustrates the sample preparation procedure. This process starts from the deposition of a SiO₂ mask layer on a 2 inch diameter Ir (001)/a-ALO wafer by RF sputtering in the APX system, Figure 9.18(a). 500 nm SiO₂ was deposited at room temperature in 2 mTorr Ar pressure at 325W yielding a deposition rate of 3 nm/min. The result was a smooth, transparent, featureless film.

The SiO₂ surface was patterned by photolithography, Figure 9.18(b). The steps of the surface patterning on diamond are described as follows:

- (1) The SiO₂ surface was treated with HMDS adhesion promoter for 10 min to improve the adhesion of PR to SiO₂ prior to a 1.3-μm thick PR (S1813) spin-coating at 5000 rpm for 35 sec. Then, the coated sample was baked in an oven at 95 °C for 40 min.
- (2) The wafer covered with PR was exposed to UV light for 9 sec through the 5-inch diameter PSI mask, as described in Chapter 9.2.1. The stripes were aligned along the <110>_{Ir} direction.
- (3) Development of the PR in Microposit 352 developer for 30 sec was followed by rinsing in flowing DI water and N₂ blown dry.
- (4) To remove the exposed SiO₂, the sample was etched in a buffered oxide etch (BOE) with a ratio of 30:1 (NH₄F:HF). The etch rate was 25 nm/min. After the PR layer was stripped in acetone, the Ir surface was covered by SiO₂ stripes with a window/repeat distance of 4/20 μm, Figure 9.18(c).
- (5) The patterned SiO₂/Ir/a-ALO wafer was coated with PR to protect the Ir during dicing. Following dicing into 10×10 mm² chips, the chips were cleaned in solvent and blown dry.

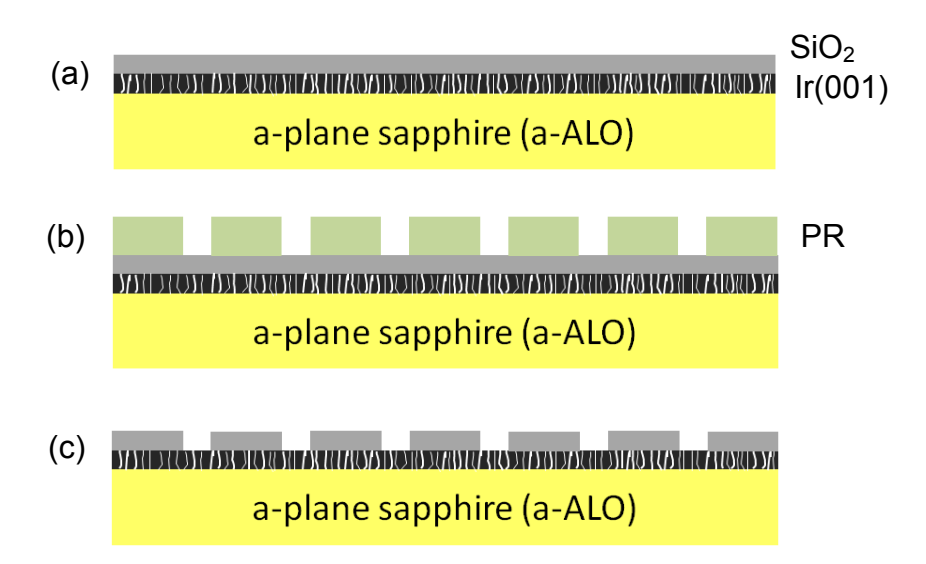


Figure 9.18 Steps followed in ELO with the SiO₂ mask process. (a) 500-nm thick SiO₂, the masking layer, was sputtered onto a Ir (001) surface, where the lines represent the dislocations lines in the Ir layer. (b) The SiO₂ surface was covered with a layer of PR, patterned by photolithography. (c) SiO₂ in the channels was etched by BOE, forming trenches.

9.3.2 BEN on patterned SiO₂/Ir (001)/a-ALO substrates

The SiO₂ patterned Ir (001)/a-ALO substrates were subjected to the BEN process, Chapter 8.4, to create diamond nucleation sites on the exposed Ir. Several attempts to carry out this procedure were unsuccessful. In particular, BEN conditions are appreciably more severe than those encountered in standard diamond growth. The high voltage applied to the substrate leads to arcing, SiO₂ sputtering, and its re-deposition as small particles on Ir, Figure 9.19. The re-deposition inhibits diamond nucleation and further growth. The arcing was observed to damage the SiO₂ and Ir surfaces as shown in Figure 9.20. Attempts to remedy the situation by decreasing the bias voltage to the threshold for DC glow ignition, and by changing the geometry of substrate

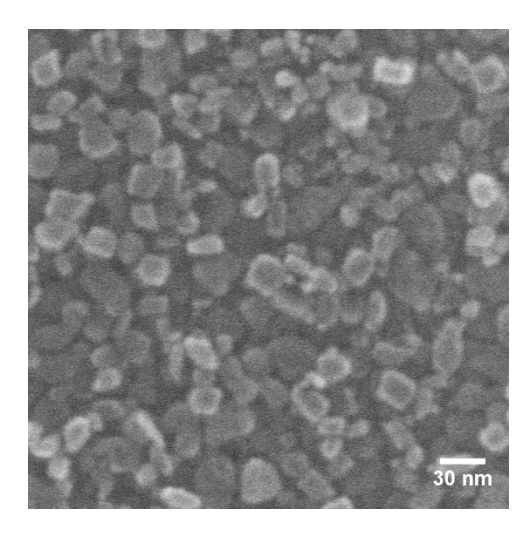


Figure 9.19 SEM image of exposed Ir surface after biased, showing nanoparticles randomly deposited on the surface.

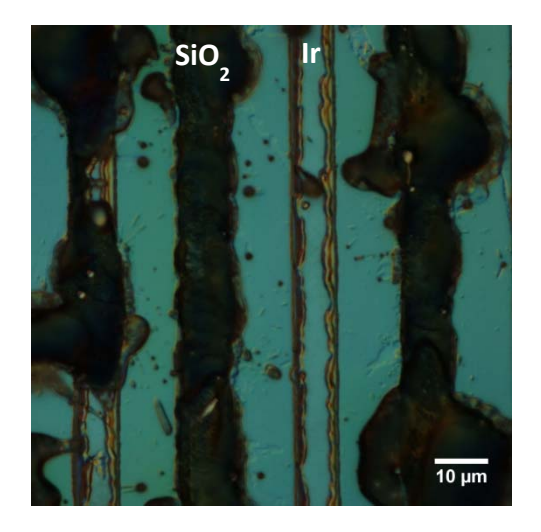


Figure 9.20 DIC optical image of damaged SiO_2 pattern on Ir (001)/a-ALO substrate. After 30 min of -200V bias, the SiO_2 and Ir surfaces were eroded by arcing.

cap were unsuccessful. Under bias, the highly insulating SiO₂ stripes become charged, leading to electrical breakdown. In some cases, the SiO₂ and Ir surfaces were burned off.

This problem could be addressed by insuring that the Ir film has a low resistance connection to the sample post. This should allow the charge to drain from the SiO₂, suppressing arcing. Since these experiments were conducted on substrates that had not been back-coated with Ir, it is likely that the circuit had a high resistance, leading to charge buildup on the SiO₂. Without charging, arcing should be eliminated and the particulate deposition should disappear.

We considered that the process might be more successful if the Ir underwent BEN exposure prior to depositing the SiO₂ layer. A substrate was prepared and biased, and then SiO₂ was stripped from half of the substrate, leaving an interface between the biased Ir and the SiO₂ mask. After diamond growth in the CVD reactor under standard conditions, results shown in Figure 9.21 were obtained. The diamond grew close to the boundary between Ir and SiO₂ which indicates that the SiO₂ does not sputter onto the Ir. Diamond clusters away from the boundary grew epitaxially. Figure 9.21(b) shows that oriented diamond grains grew close to the edges of the SiO₂. Furthermore, the biased Ir surface was not damaged by the BOE HF etch. The low diamond nucleation density observed is attributed to a non-ideal BEN process which was not optimized in this experiment. These results demonstrate that diamond grown by this method remains an option although further work is needed for its optimization.

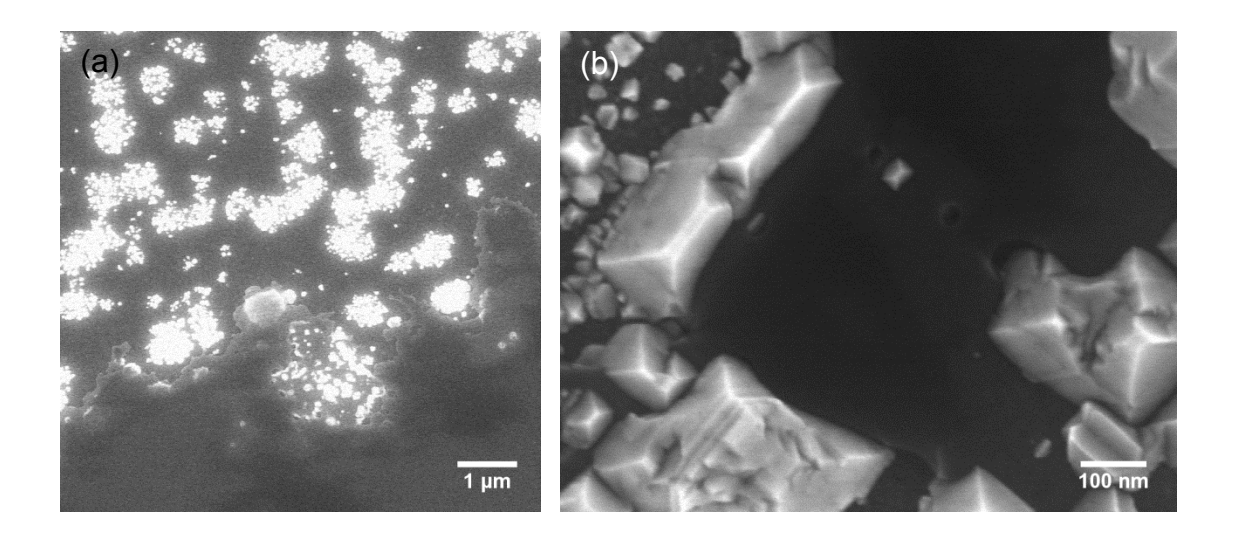


Figure 9.21 SEM images of diamond growth near a SiO_2 boundary. The SiO_2 layer is the dark region in the images. (a) Plan-view and (b) 5° tilt SEM image showing diamond growth adjacent to SiO_2 .

10. Chapter 10 Conclusions and outlook

This research has been motivated by the prospect of producing single crystal diamond wafers with the quality of present silicon and gallium arsenide substrates. There had been two major obstacles in reaching this goal. The first was the inability to grow diamond at the wafer scale. The second was the poor crystalline structural quality in such materials. To overcome the first obstacle, heteroepitaxial growth of diamond on sapphire has been investigated, as described in earlier chapters. A significant advance in nucleating diamond on a thin buffer layer of Ir has been reached at the 1 cm scale. A high-density nucleation procedure, which proved problematic in the past, has been placed on a solid foundation, with a highly reproducible process developed. The initial diamond layer that forms on a buffer layer is always highly defective, so methods to localize the defects in the vicinity of the substrate have been invented. Several epitaxial lateral overgrowth methods have been explored, with one method in particular that is simple to implement and has produced thick diamond films with greatly improved structural quality.

The major results of this work are summarized as follows.

- 1. **Epitaxial Ir growth on sapphire**. A robust sputtering process for growing (001) Ir epitaxial films on a-plane sapphire wafers was developed. By studying Ir on substrates with different miscut angles by x-ray diffraction, no trace of misoriented grains was found. In the past, sensitivity to miscut angles and existence of Ir (111) grains had been a concern.
- 2. **Bias-enhanced nucleation of diamond**. A significant advance in increasing the area of highly nucleated diamond on Ir was made. The reproducibility of the process, which

depends critically on control of the plasma in the vicinity of the substrate, was improved by careful examination of plasma instabilities. This is a key step for producing cm-sized thin diamond substrates, without which photolithography for lateral overgrowth would not be practicable.

- 3. Heteroepitaxial diamond growth of thick films on sapphire. Exposure of sapphire to the high temperature, highly reactive CVD hydrogen plasma was tested. It had been unclear whether degradation of the oxide substrate would occur, particularly with growth times of several days. Sapphire, whether protected by Ir or not, was found to be unaffected by the plasma chemistry or by thermal shock. As a consequence, non-ELO growth of CVD diamond on Ir was demonstrated using typical growth rates and temperatures for films up to 0.1 mm thickness.
- 4. **Diamond epitaxial lateral overgrowth**. A *photolithographic* ELO method using a simple metal mask was successfully demonstrated. The single prior example of ELO on diamond had used *electron-beam lithography* to produce a patterned substrate, a process which cannot be readily scaled to large substrates. The metal mask is a simple Au film which can be readily deposited at room temperature by thermal evaporation using standard equipment. Diamond successfully overgrew and coalesced above the masked regions. It was shown by a number of methods that dislocations, the source of internal stress in diamond, were largely excluded from the overgrown regions. By increasing the relative area of the overgrown region, it was shown that there was a commensurate improvement of diamond quality, as evidenced by a decreased Raman linewidth.
- 5. **Thermal stress reduction**. Thermally-induced stress, caused by the thermal expansivity mismatch between substrate and diamond, is problematic in heteroepitaxy and in all film

growth. The larger contraction of sapphire relative to diamond, when cooled from growth temperatures of 800 to 1100 °C, generally leads to fracture of film and substrate or delamination of diamond. A major advantage of Au-masked lateral overgrowth is the stress relief provided by the ductile Au film in the overgrown film. Whereas non-ELO diamond on sapphire was always found to fracture and delaminate on cooling. ELO-grown diamond, on the other hand, adhered to the substrate for a large range of thicknesses. For 2-µm thick ELO diamond, the thermal stress was reduced by a factor of about 3, even with a relatively small overgrown area. For a 0.2-mm thick ELO diamond plate, it was found that the growth surface was nearly stress-free, with a stress magnitude of 0.00±0.16 GPa.

Although dislocation confinement in diamond grown by ELO and the corresponding reduction of the Raman linewidth in overgrown regions were observed, additional quantitative evidence of dislocation density reduction is needed. The most direct test is by growth of diamond, under identical conditions, on ELO and non-ELO prepared substrates. Using interrupted growth and surface plasma etching, the etch pits that terminate dislocations can be readily counted and their evolution observed as diamond thickness increases. In a preliminary report, it was inferred that a dislocation density reduction by two orders of magnitude had occurred on ELO-grown material before the film thickness grew to 100 μm.¹⁷²

Because of the dislocation confinement resulting from Au-masked ELO, multiple ELO processes would be attractive. After a short growth step to the coalescence point, the substrate could be subjected to another lithography step, with the mask translated to block the previously unmasked region. Other alternatives are masking patterns with wider stripe to space ratios or a grid mask pattern for island growth.

The two other ELO methods briefly explored are also promising, especially the PENDEO process. Since the PENDEO process does not require a mask during growth, the temperature can be increased, leading to a higher growth rate from the onset. Improvements in this process would benefit from equipment that will allow for more efficient diamond etching.

Ultimately, the overall growth process should be tuned for higher chemical purity of the resulting diamond. This can be accomplished by slight modifications of growth conditions, along with greater purity and combinations of feedstock gases. Higher chemical and structural perfection is important for maximizing carrier lifetimes in particle detector applications. A program of carrier time-of-flight measurements with feedback to growth variables is needed. Such systematic research would allow the defects responsible for carrier scattering and trapping to be identified and eliminated.

APPENDIX

APPENDIX

Calculations of stress in diamond

The theoretical thermal stress in diamond grown on a substrate can be calculated from elasticity theory¹⁵⁶ by

$$\sigma_d = \Delta \varepsilon E_d / (1 - \nu_d)$$
 A.1

where σ is the biaxial stress, $\Delta \varepsilon$ the thermal strain, E is Young's modulus and v is Poisson's ratio. The thermal strain from a-ALO substrate to diamond is given by

$$\Delta \varepsilon = \int_{T_1}^{T_2} [\propto_d (T) - \propto_s (T)] dT$$
 A.2

where α is the thermal expansivity of diamond (*d*) and a-ALO (*s*), T_2 is the growth temperature and T_1 is usually room temperature, 25 °C. The thermal expansivities of diamond and sapphire at different temperatures are listed in Table A.1.

Table A.1 Temperature dependent thermal expansion coefficients of diamond and sapphire. ¹⁷³

Material _	$\alpha/(10^{-6} \text{ K}^{-1})$						
	100K	200K	293K	500K	800K	1100K	1500K
Diamond	0.05	0.4	1	2.3	3.7	4.7	5.6
Sapphire (c-axis)	3.6	4.1	4.8	7.9	8.9	9.8	10.9
Sapphire (m-axis)	3.3	2.2	6.6	7.4	8.3	9.1	10.0

By the integration of thermal expansion coefficients between 750 °C and room temperature from Table A.1, the thermal strains along c-axis and m-axis are -3.75×10^{-3} and -3.6×10^{-3} , respectively. Since the difference is negligible we use the average strain, -3.68×10^{-3} , to estimate the thermal stress. The Young's modulus of diamond is 1140 GPa and Poisson's ratio is 0.07. As a result, the thin film thermal stress in diamond is -4.55 GPa.

Relations between stress and Raman peak shift

Stress in diamond can be estimated from the shift of the Raman peak position. For unstressed Type IIa natural diamond, the Raman peak center is located at 1332.4 cm⁻¹. The relationships between stress and Raman peak shift³⁵ under various conditions are listed below. A compressive stress corresponds to a blue shift, and a tensile stress to a red shift.

(i) Hydrostatic stress:

$$\tau_{1,2,3} = -0.31 \, GPa/cm^{-1}$$
 (triplet)

(ii) Biaxial stress in (001) plane:

$$\tau_{1,2} = -0.42 \, GPa/cm^{-1} \, (doublet)$$
 A.4-1

$$\tau_3 = -0.61 \, GPa/cm^{-1} \, (\text{singlet})$$
 A.4-2

(iii) Biaxial stress in (110) plane:

$$au_1 = -1.09 \, GPa/cm^{-1}$$
 A.5-1
 $au_2 = -0.42 \, GPa/cm^{-1}$ A.5-2
 $au_3 = -0.32 \, GPa/cm^{-1}$ A.5-3

(iv) Biaxial stress in (111) plane:

$$au_1 = -1.49 \, GPa/cm^{-1} \, (\text{singlet})$$
 A.6-1
$$au_{2,3} = -0.35 \, GPa/cm^{-1} \, (\text{doublet})$$
 A.6-2

(v) Uniaxial stress in [001] direction:

$$au_{1,2} = -1.21 \, GPa/cm^{-1} \, (doublet)$$
 A.7-1
$$au_3 = -0.64 \, GPa/cm^{-1} \, (singlet)$$
 A.7-2

(vi) Uniaxial stress in [110] direction:

$$au_1 = -1.21 \, GPa/cm^{-1}$$
 A.8-1
 $au_2 = -10.78 \, GPa/cm^{-1}$ A.8-2
 $au_3 = -0.44 \, GPa/cm^{-1}$ A.8-3

(vii) Uniaxial stress in [111] direction:

$$au_1 = -0.40 \, GPa/cm^{-1} \, (\text{singlet})$$
 A.9-1
$$au_{2,3} = -2.97 \, GPa/cm^{-1} \, (\text{doublet})$$
 A.9-2

BIBLIOGRAPHY

BIBLIOGRAPHY

- ¹ W. Adam, B. Bellini, E. Berdermann, and P. Bergonzo, Nucl. Instruments Methods Phys. Res. Sect. A Accel. Spectrometers, Detect. Assoc. Equip. **511**, 124 (2003).
- ² C. Wild, P. Koidl, W. Müller-Sebert, H. Walcher, R. Kohl, N. Herres, R. Locher, R. Samlenski, and R. Brenn, Diam. Relat. Mater. **2**, 158 (1993).
- ³ X. Jiang and C.-P. Klages, Diam. Relat. Mater. **2**, 1112 (1993).
- ⁴ K. Ohtsuka, K. Suzuki, A. Sawabe, and T. Inuzuka, Jpn. J. Appl. Phys. **35**, L1072 (1996).
- ⁵ K. Ohtsuka, H. Fukuda, K. Suzuki, and A. Sawabe, Jpn. J. Appl. Phys. **36**, L1214 (1997).
- ⁶ M. Schreck, H. Roll, and B. Stritzker, Appl. Phys. Lett. **74**, 650 (1999).
- ⁷ F. Hörmann, H. Roll, M. Schreck, and B. Stritzker, Diam. Relat. Mater. **9**, 256 (2000).
- ⁸ C. Bednarski, Z. Dai, A.-P. Li, and B. Golding, Diam. Relat. Mater. **12**, 241 (2003).
- ⁹ B. Golding, C. Bednarski-Meinke, and Z. Dai, Diam. Relat. Mater. **13**, 545 (2004).
- ¹⁰ Z. Dai, C. Bednarski-Meinke, R. Loloee, and B. Golding, Appl. Phys. Lett. **82**, 3847 (2003).
- ¹¹ S. Gsell, T. Bauer, J. Goldfuß, M. Schreck, and B. Stritzker, Appl. Phys. Lett. 84, 4541 (2004).
- ¹² Y. Ando, J. Kuwabara, K. Suzuki, and A. Sawabe, Diam. Relat. Mater. 13, 1975 (2004).
- ¹³ S. Washiyama, S. Mita, K. Suzuki, and A. Sawabe, Appl. Phys. Express 4, 095502 (2011).
- ¹⁴ W. Massa, Crystal Structure Determination (Springer-Verlag, Berlin, 2000).
- ¹⁵ B.B. Pate, *Diamond: Electronic Properties and Applications* (Kluwer Academic publisher, 1995).
- ¹⁶ J. Isberg, J. Hammersberg, E. Johansson, T. Wikström, D.J. Twitchen, A.J. Whitehead, S.E. Coe, and G.A. Scarsbrook, Science **297**, 1670 (2002).
- ¹⁷ F. Himpsel, J. Knapp, J. VanVechten, and D. Eastman, Phys. Rev. B 20, 624 (1979).
- ¹⁸ M.W. Geis, N.N. Efremow, J.D. Woodhouse, M.D. McAleese, M. Marchywka, D.G. Socker, and J.F. Hochedez, IEEE Electron Device Lett. **12**, 456 (1991).
- ¹⁹ R. Mildren, *Optical Engieering of Diamond* (John Wiley & Sons, Somerset, 2013).
- ²⁰ J.L. Warren, J.L. Yarnell, G. Dolling, and R.A. Cowley, Phys. Rev. **158**, 805 (1967).
- ²¹ M. Liu, L. Bursill, S. Prawer, and R. Beserman, Phys. Rev. B **61**, 3391 (2000).

- ²² K. Ishioka, M. Hase, M. Kitajima, and H. Petek, Appl. Phys. Lett. **89**, 231916 (2006).
- ²³ K.C. Lee, B.J. Sussman, J. Nunn, V.O. Lorenz, K. Reim, D. Jaksch, I.A. Walmsley, P. Spizzirri, and S. Prawer, Diam. Relat. Mater. **19**, 1289 (2010).
- ²⁴ S. Solin and A. Ramdas, Phys. Rev. B **1**, (1970).
- ²⁵ F.P. Bundy, H.T. Hall, H.M. Strong, and R.H. Wentorf, Nature **176**, 51 (1955).
- ²⁶ F.P. Bundy, J. Chem. Phys. **38**, 631 (1963).
- ²⁷ R.S. Balmer, J.R. Brandon, S.L. Clewes, H.K. Dhillon, J.M. Dodson, I. Friel, P.N. Inglis, T.D. Madgwick, M.L. Markham, T.P. Mollart, N. Perkins, G.A. Scarsbrook, D.J. Twitchen, A.J. Whitehead, J.J. Wilman, and S.M. Woollard, J. Physics. Condens. Matter **21**, 364221 (2009).
- ²⁸ J. Wilks and E. Wilks, *Properties and Applications of Diamond*, 3rd ed. (Butterworth-Heinemann, 1994).
- ²⁹ A. Khursheed, *Scanning Electron Microscope Optics and Spectrometers* (World Scientific, Singapore, 2011).
- ³⁰ Y. Martin, C.C. Williams, and H.K. Wickramasinghe, J. Appl. Phys. **61**, 4723 (1987).
- ³¹ Murari Regmi, Ph.D. Dissertation, Michigan State University, 2008.
- ³² J.R. Ferraro, K. Nakamoto, and C.W. Brown, *Introductory Raman Spectroscopy*, second edition (Elsevier, 2003).
- ³³ J. Birman, Phys. Rev. **127**, 1093 (1962).
- ³⁴ R. Loudon, Adv. Phys. **13**, 423 (1964).
- ³⁵ Y. von Kaenel, J. Stiegler, J. Michler, and E. Blank, J. Appl. Phys. **81**, 1726 (1997).
- ³⁶ S. Ganesan, A. Maradudin, and J. Oitmaa, Ann. Phys. (N. Y). **56**, 556 (1970).
- ³⁷ E. Anastassakis, A. Pinczuk, and E. Burstein, Solid State Commun. **8**, 133 (1970).
- ³⁸ J.E. Field, *The Properties of Natural and Synthetic Diamond* (Academic, London, 1979).
- ³⁹ M.H. Grimsditch, E. Anastassakis, and M. Cardona, Phys. Rev. B **18**, 901 (1978).
- ⁴⁰ J. Ager and M. Drory, Phys. Rev. B **48**, 2601 (1993).
- ⁴¹ S. Porto, J. Giordmaine, and T. Damen, Phys. Rev. **147**, 608 (1966).
- ⁴² J.L. Vossen and W. Kern, editors, *Thin Film Processes* (Academic Press, INC., 1978).
- ⁴³ M.A. Lieberman and A.J. Lichtenberg, *Principles of Plasma Discharges and Materials Processing* (John Wiley & Sons, Inc., New York, 1994).
- ⁴⁴ H.V. Boening, *Plasma Science and Technology* (Cornell University Prss, London, 1982).

- ⁴⁵ R.E. Clausing, L.L. Horton, J.C. Angus, and P. Koidl, editors, *Diamond and Diamond-like Films and Coatings* (Plenum Press, New York, 1991).
- ⁴⁶ K. Kuo and J. Asmussen, Diam. Relat. Mater. **6**, 1097 (1997).
- ⁴⁷ C.R. Bednarski-Meinke, Ph.D. Dissertation, Michigan State University, 2002.
- ⁴⁸ J. Asmussen and D. Reinhard, *Diamond Films Handbook* (CRC press, 2002).
- ⁴⁹ J.C. Angus, J. Appl. Phys. **39**, 2915 (1968).
- ⁵⁰ D.J. Poferl, J. Appl. Phys. **44**, 1428 (1973).
- ⁵¹ J.C. Angus and C.C. Hayman, Science **241**, 913 (1988).
- ⁵² B.V. Spitsyn, L.L. Bouilov, and B.V. Derjaguin, J. Cryst. Growth **52**, 219 (1981).
- ⁵³ M. Kamo, Y. Sato, S. Matsumoto, and N. Setaka, J. Cryst. Growth **62**, 642 (1983).
- ⁵⁴ A. Sawabe and T. Inuzuka, Appl. Phys. Lett. **46**, 146 (1985).
- ⁵⁵ C.J. Chu, R.H. Hauge, J.L. Margrave, and M.P. D'Evelyn, Appl. Phys. Lett. **61**, 1393 (1992).
- ⁵⁶ H. Maeda, K. Ohtsubo, M. Irie, N. Ohya, K. Kusakabe, and S. Morooka, J. Mater. Res. **10**, 3115 (1995).
- ⁵⁷ I. Sakaguchi, M. Nishitani-Gamo, K.P. Loh, H. Haneda, and T. Ando, J. Appl. Phys. **86**, 1306 (1999).
- ⁵⁸ J. Achard, A. Tallaire, R. Sussmann, F. Silva, and A. Gicquel, J. Cryst. Growth **284**, 396 (2005).
- ⁵⁹ T. Teraji, Phys. Status Solidi **203**, 3324 (2006).
- ⁶⁰ C.-S. Yan and Y.K. Vohra, Diam. Relat. Mater. **8**, 2022 (1999).
- ⁶¹ J. Lu, Y. Gu, T.A. Grotjohn, T. Schuelke, and J. Asmussen, Diam. Relat. Mater. **37**, 17 (2013).
- ⁶² K. Kobashi, K. Nishimura, Y. Kawate, and T. Horiuchi, Phys. Rev. B 38, 4067 (1988).
- ⁶³ C. Wild, R. Kohl, N. Herres, and P. Koidl, Diam. Relat. Mater. **3**, 373 (1994).
- ⁶⁴ F. Silva, J. Achard, X. Bonnin, A. Michau, A. Tallaire, O. Brinza, and A. Gicquel, Phys. Status Solidi **203**, 3049 (2006).
- ⁶⁵ M. Volmer and A. Weber, A. Phys. Chemie **119**, 277 (1925).
- ⁶⁶ R. Becker and W. Doering, **24**, 719 (1935).
- ⁶⁷ J. Frenkel, J. Chem. Phy. **7**, 538 (1939).
- ⁶⁸ J.B. Zeldovich, Acta Physicochim. USSR **18**, 1 (1943).

- ⁶⁹ L. Zang, Lecture Note: Kinetics (2013).
- ⁷⁰ J.A. Venables, *Introduction to Surface and Thin Film Processes*, 2nd ed. (Cambridge University Press, 2003).
- ⁷¹ H. Yamada, A. Chayahara, H. Umezawa, N. Tsubouchi, Y. Mokuno, and S. Shikata, Diam. Relat. Mater. **24**, 29 (2012).
- ⁷² R.J. Jaccodine, Journal Electrochem. Soc. **110**, 524 (1963).
- ⁷³The CVD Diamond Booklet (Freiburg, 2008).
- ⁷⁴ P. Becker, P. Scyfried, and H. Siegert, Zeitschrift Für Phys. B Condens. Matter **48**, 17 (1982).
- ⁷⁵ J.W. Arblaster, Platin. Met. Rev. **54**, 93 (2010).
- ⁷⁶Strontinum Titanate-Properties and Applications (Macclesfield, 2013).
- ⁷⁷ O. Madelung, U. Rössler, and M. Schulz, editors, *II-VI and I-VII Compounds*; *Semimagnetic Compounds* (Springer-Verlag, Berlin/Heidelberg, 1999).
- ⁷⁸Single Crystal Sapphire (Vancouver, 2012).
- ⁷⁹ P.C. Yang, R. Schlesser, C.A. Wolden, W. Liu, R.F. Davis, Z. Sitar, and J.T. Prater, Appl. Phys. Lett. **70**, 2960 (1997).
- ⁸⁰ Z. Sitar, W. Liu, P.C. Yang, C.A. Wolden, R. Schlesser, and J.T. Prater, Diam. Relat. Mater. **7**, 276 (1998).
- ⁸¹ S.D. Wolter, B.R. Stoner, J.T. Glass, P.J. Ellis, D.S. Buhaenko, C.E. Jenkins, and P. Southworth, Appl. Phys. Lett. 62, 1215 (1993).
- ⁸² W. Zhu, X. Wang, B. Stoner, G. Ma, H. Kong, M. Braun, and J. Glass, Phys. Rev. B 47, 6529 (1993).
- ⁸³ X. Jiang, M. Fryda, and C.L. Jia, Diam. Relat. Mater. **9**, 1640 (2000).
- ⁸⁴ X. Jiang and C.L. Jia, Appl. Phys. Lett. **67**, 1197 (1995).
- ⁸⁵ C. Jia, K. Urban, and X. Jiang, Phys. Rev. B **52**, 5164 (1995).
- ⁸⁶ S. Koizumi, T. Murakami, T. Inuzuka, and K. Suzuki, Appl. Phys. Lett. **57**, 563 (1990).
- ⁸⁷ S. Koizumi, Isr. J. Chem. **38**, 33 (1998).
- ⁸⁸ W.A. Yarbrough and R. Messier, Science **247**, 688 (1990).
- ⁸⁹ R.H. Wentorf, Adv. Chem. Phys. **9**, 365 (1965).
- ⁹⁰ T. Tachibana, Y. Yokota, K. Nishimura, K. Miyata, K. Kobashi, and Y. Shintani, Diam. Relat. Mater. **5**, 197 (1996).

- ⁹¹ M. Hansen, *Constitution of Binary Alloys*, 2nd ed. (McGraw-Hill Book Co., New York, Toronto, London, 1958).
- ⁹² C.H. Lee, J. Qi, S.T. Lee, and L.S. Hung, Diam. Relat. Mater. **12**, 1335 (2003).
- ⁹³ Y. Wu, J. Qi, C.H. Lee, L.S. Hung, W.J. Zhang, I. Bello, Y. Lifshitz, and S.T. Lee, Diam. Relat. Mater. **12**, 1675 (2003).
- ⁹⁴ S. Iijima, Y. Aikawa, and K. Baba, J. Mater. Res. **6**, 1491 (1991).
- 95 S. Yugo, T. Kanai, T. Kimura, and T. Muto, Appl. Phys. Lett. **58**, 1036 (1991).
- ⁹⁶ K. Kobayashi, N. Mutsukura, and Y. Machi, Mater. Manuf. Process. 7, 395 (1992).
- ⁹⁷ J.E. Yehoda, R.I. Fuentes, J.C. Tsang, S.J. Whitehair, C.R. Guarnieri, and J.J. Cuomo, Appl. Phys. Lett. **60**, 2865 (1992).
- ⁹⁸ S.J. Lin, S.L. Lee, J. Hwang, C.S. Chang, and H.Y. Wen, Appl. Phys. Lett. **60**, 1559 (1992).
- ⁹⁹ J. Narayan, V.P. Godbole, G. Matera, and R.K. Singh, J. Appl. Phys. **71**, 966 (1992).
- ¹⁰⁰ D. Michau, B. Tanguy, G. Demazeau, M. Couzi, and R. Cavagnat, Diam. Relat. Mater. **2**, 19 (1993).
- ¹⁰¹ H. Liu and D.S. Dandy, Diam. Relat. Mater. **4**, 1173 (1995).
- ¹⁰² Sz. Katai, A. Kovats, I. Maros, and P. Deak, Diam. Relat. Mater. 9, 317 (2000).
- ¹⁰³ S. Yugo, T. Kimura, and T. Kanai, Diam. Relat. Mater. **2**, 328 (1992).
- ¹⁰⁴ S. Yugo, K. Semoto, K. Hoshina, T. Kimura, and H. Nakai, Diam. Relat. Mater. **4**, 903 (1995).
- ¹⁰⁵ X. Jiang, K. Schiffmann, and C.-P. Klages, Phys. Rev. B **50**, 8402 (1994).
- 106 X. Jiang, W. Zhang, and C.-P. Klages, Phys. Rev. B $\boldsymbol{58},$ 7064 (1998).
- ¹⁰⁷ K. Perng, K.-S. Liu, and I.-N. Lin, J. Appl. Phys. **91**, 3934 (2002).
- ¹⁰⁸ B.W. Sheldon, R. Csencsits, J. Rankin, R.E. Boekenhauer, and Y. Shigesato, J. Appl. Phys. **75**, 5001 (1994).
- ¹⁰⁹ S.P. McGinnis, M.A. Kelly, S.B. Hagström, and R.L. Alvis, J. Appl. Phys. **79**, 170 (1996).
- ¹¹⁰ J. Robertson, Diam. Relat. Mater. **2**, 984 (1993).
- ¹¹¹ J. Robertson, Diam. Relat. Mater. **3**, 361 (1994).
- ¹¹² J. Robertson, Appl. Phys. Lett. **66**, 3287 (1995).
- ¹¹³ Y. Lifshitz, S. Kasi, and J. Rabalais, Phys. Rev. Lett. **62**, 1290 (1989).
- ¹¹⁴ M.D. Whitfield, R.B. Jackman, D. Rodway, J.A. Savage, and J.S. Foord, J. Appl. Phys. **80**, 3710 (1996).

- ¹¹⁵ J.A. Mucha, D.L. Flamm, and D.E. Ibbotson, J. Appl. Phys. **65**, 3448 (1989).
- ¹¹⁶ M. Schreck, T. Bauer, and B. Stritzker, Diam. Relat. Mater. 4, 553 (1995).
- ¹¹⁷ R. Stöckel, K. Janischowsky, S. Rohmfeld, J. Ristein, M. Hundhausen, and L. Ley, Diam. Relat. Mater. **5**, 321 (1996).
- ¹¹⁸ R. Stöckel, M. Stammler, and K. Janischowsky, J. Appl. Phys. **83**, 531 (1998).
- ¹¹⁹ S. Barrat, S. Saada, I. Dieguez, and E. Bauer-Grosse, J. Appl. Phys. **84**, 1870 (1998).
- ¹²⁰ Y. Shigesato, R.E. Boekenhauer, and B.W. Sheldon, Appl. Phys. Lett. **63**, 314 (1993).
- ¹²¹ Y.-K. Kim and J.-Y. Lee, J. Appl. Phys. **81**, 3660 (1997).
- ¹²² G. Balestrino, M. Marinelli, E. Milani, A. Paoletti, I. Pinter, A. Tebano, and P. Paroli, Appl. Phys. Lett. **62**, 879 (1993).
- ¹²³ A. Sawabe, H. Fukuda, T. Suzuki, Y. Ikuhara, and T. Suzuki, Surf. Sci. **467**, 845 (2000).
- ¹²⁴ K. Ohtsuka, K. Suzuki, A. Sawabe, and T. Inuzuka, Jpn. J. Appl. Phys. **35**, L1072 (1996).
- ¹²⁵ M. Regmi, K. More, and G. Eres, Diam. Relat. Mater. **23**, 28 (2012).
- ¹²⁶ F. Hörmann, M. Schreck, and B. Stritzker, Diam. Relat. Mater. **10**, 1617 (2001).
- ¹²⁷ T. Bauer, S. Gsell, F. Hörmann, M. Schreck, and B. Stritzker, Diam. Relat. Mater. **13**, 335 (2004).
- ¹²⁸ M. Schreck, T. Bauer, S. Gsell, F. Hörmann, H. Bielefeldt, and B. Stritzker, Diam. Relat. Mater. **12**, 262 (2003).
- ¹²⁹ N. Vaissiere, S. Saada, M. Bouttemy, A. Etcheberry, P. Bergonzo, and J.C. Arnault, Diam. Relat. Mater. **36**, 16 (2013).
- ¹³⁰ A. Nikitin, L.-Å. Näslund, Z. Zhang, and A. Nilsson, Surf. Sci. **602**, 2575 (2008).
- ¹³¹ S. Rey, F. Antoni, B. Prevot, E. Fogarassy, J.C. Arnault, J. Hommet, F. Le Normand, and P. Boher, Appl. Phys. A Mater. Sci. Process. **71**, 433 (2000).
- ¹³² A. Chavanne, J. Barjon, B. Vilquin, J. Arabski, and J.C. Arnault, Diam. Relat. Mater. **22**, 52 (2012).
- ¹³³ S. Gsell, M. Schreck, G. Benstetter, E. Lodermeier, and B. Stritzker, Diam. Relat. Mater. **16**, 665 (2007).
- ¹³⁴ T. Bauer, M. Schreck, F. Hörmann, A. Bergmaier, G. Dollinger, and B. Stritzker, Diam. Relat. Mater. **11**, 493 (2002).
- ¹³⁵ S. Gsell, S. Berner, T. Brugger, M. Schreck, R. Brescia, M. Fischer, T. Greber, J. Osterwalder, and B. Stritzker, Diam. Relat. Mater. 17, 1029 (2008).

- ¹³⁶ A. Hoffman, S. Michaelson, R. Akhvlediani, N.K. Hangaly, S. Gsell, R. Brescia, M. Schreck, B. Stritzker, J.C. Arnault, and S. Saada, Phys. Status Solidi Appl. Mater. Sci. **206**, 1972 (2009).
- ¹³⁷ C. Stehl, M. Fischer, S. Gsell, E. Berdermann, M.S. Rahman, M. Traeger, O. Klein, and M. Schreck, Appl. Phys. Lett. **103**, 3 (2013).
- ¹³⁸ D. Hull and D.J. Bacon, *Introduction to Dislocations* (Elsevier, 2011).
- ¹³⁹ F.W. Tausch and A.G. Lapierre, J. Electrochem. Soc. **112**, 706 (1965).
- ¹⁴⁰ M. Michelitsch, J. Electrochem. Soc. **112**, 747 (1965).
- ¹⁴¹ D.W. Shaw, J. Electrochem. Soc. **113**, 904 (1966).
- ¹⁴² T. Nishinaga, T. Nakano, and S. Zhang, Jpn. J. Appl. Phys. **27**, L964 (1988).
- ¹⁴³ A. Usui, H. Sunakawa, A. Sakai, and A.A. Yamaguchi, Jpn. J. Appl. Phys. **36**, L899 (1997).
- ¹⁴⁴ A. Sakai, H. Sunakawa, and A. Usui, Appl. Phys. Lett. **71**, 2259 (1997).
- ¹⁴⁵ A. Sakai, H. Sunakawa, and A. Usui, Appl. Phys. Lett. **73**, 481 (1998).
- Y. Kawaguchi, S. Nambu, H. Sone, T. Shibata, H. Matsushima, M. Yamaguchi, T. Miyake, K. Hiramatsu, and N. Sawaki, Jpn. J. Appl. Phys. 37, L845 (1998).
- ¹⁴⁷ H. Sone, S. Nambu, Y. Kwawguchi, M. Yamaguchi, H. Miyake, K. Hiramatsu, Y. Iyechika, T. Maeda, and N. Sawaki, Jpn. J. Appl. Phys. **38**, L356 (1999).
- ¹⁴⁸ Y. Honda, Y. Iyechika, T. Maeda, H. Miyake, and K. Hiramatsu, Japanes J. Appl. Phys. **38**, L1299 (1999).
- ¹⁴⁹ S. Tomiya, K. Funato, T. Asatsuma, T. Hino, S. Kijima, T. Asano, and M. Ikeda, Appl. Phys. Lett. **77**, 636 (2000).
- ¹⁵⁰ T.S. Zheleva, S.A. Smith, D.B. Thomson, K.J. Linthicum, P. Rajagopal, and R.F. Davis, J. Electron. Mater. **28**, L5 (1999).
- ¹⁵¹ I. Kidoguchi, A. Ishibashi, G. Sugahara, and Y. Ban, Appl. Phys. Lett. 76, 3768 (2000).
- ¹⁵² T.D. Detchprohm, M. Yano, S. Sano, R. Nakamura, and S. Mochiduki, Jpn. J. Appl. Phys. **40**, L16 (2001).
- ¹⁵³ X. Zhang, R.R. Li, P.D. Dapkus, and D.H. Rich, Appl. Phys. Lett. 77, 2213 (2000).
- ¹⁵⁴ T. Bauer, M. Schreck, and B. Stritzker, Diam. Relat. Mater. **16**, 711 (2007).
- ¹⁵⁵ B. Wölfing, K. Theis-Bröhl, C. Sutter, and H. Zabel, J. Phys. Condens. Matter **11**, 2669 (1999).
- ¹⁵⁶ J. Michler, M. Mermoux, Y. Von Kaenel, A. Haouni, G. Lucazeau, and E. Blank, Thin Solid Films, **357**, 189 (1999).

- ¹⁵⁷ O. Dorsch, M. Werner, and E. Obermeier, Diam. Relat. Mater. **4**, 456 (1995).
- ¹⁵⁸ Y. Ando, Y. Nishibayashi, K. Kobashi, T. Hirao, and K. Oura, Diam. Relat. Mater. **11**, 824 (2002).
- ¹⁵⁹ D.S. Hwang, T. Saito, and N. Fujimori, Diam. Relat. Mater. **13**, 2207 (2004).
- ¹⁶⁰ J. Enlund, J. Isberg, M. Karlsson, F. Nikolajeff, J. Olsson, and D.J. Twitchen, Carbon **43**, 1839 (2005).
- ¹⁶¹ D.T. Tran, T.A. Grotjohn, D.K. Reinhard, and J. Asmussen, Diam. Relat. Mater. **17**, 717 (2008).
- ¹⁶² S.J. Pearton, A. Katz, F. Ren, and J.R. Lothian, Electron. Lett. **28**, 822 (1992).
- ¹⁶³ A.F. Isakovic, A. Stein, J.B. Warren, S. Narayanan, M. Sprung, A.R. Sandy, and K. Evans-Lutterodt, J. Synchrotron Radiat. **16**, 8 (2008).
- ¹⁶⁴ B.J.M. Hausmann, M. Khan, Y. Zhang, T.M. Babinec, K. Martinick, M. McCutcheon, P.R. Hemmer, and M. Lončar, Diam. Relat. Mater. **19**, 621 (2010).
- ¹⁶⁵ D.T. Tran, C. Fansler, T.A. Grotjohn, D.K. Reinhard, and J. Asmussen, Diam. Relat. Mater. **19**, 778 (2010).
- ¹⁶⁶ S.A. Grot, R.A. Ditizio, G.S. Gildenblat, A.R. Badzian, and S.J. Fonash, Appl. Phys. Lett. **61**, 2326 (1992).
- ¹⁶⁷ O. Dorsch, M. Werner, and E. Obermeier, Diam. Relat. Mater. 1, 277 (1992).
- ¹⁶⁸ T. Yamada, H. Yoshikawa, H. Uetsuka, S. Kumaragurubaran, N. Tokuda, and S.I. Shikata, Diam. Relat. Mater. **16**, 996 (2007).
- ¹⁶⁹ B.R. Stoner, G.J. Tessmer, and D.L. Dreifus, Appl. Phys. Lett. **62**, 1803 (1993).
- ¹⁷⁰ K. Kobashi, T. Tachibana, Y. Yokota, N. Kawakami, K. Hayashi, K. Yamamoto, Y. Koga, S. Fujiwara, Y. Gotoh, H. Nakahara, H. Tsuji, J. Ishikawa, F.A. Köck, and R.J. Nemanich, J. Mater. Res. **18**, 305 (2003).
- ¹⁷¹ R. Hsiao, D. Miller, S. Nguyen, and A. Kellock, Appl. Surf. Sci. **148**, 1 (1999).
- ¹⁷² Y.-H. Tang, B. Bi, and B. Golding, MRS Proc. **1734**, mrsf14-1734-r05-04 (2015).
- ¹⁷³ Y.S. Touloukian, R.K. Kirby, R.E. Taylor, and T.Y.R. Lee, *Thermophysical Properties of Matter* (IFI Plenum, New York, 1971).